The submillimetre and near-infrared properties of *Herschel*-ATLAS sources

Simone Fleuren

School of Physics and Astronomy

Queen Mary University of London

A thesis submitted for the degree of

PhilosophiæDoctor (PhD) in Astronomy

November 2012

Abstract

In this thesis I investigate a sample of galaxies that are detected with the *Herschel* Space Telescope in the sub-millimetre wavelength range and that also have near-infrared detections with the VISTA telescope in Chile as part of the VIKING survey.

The first necessity is to find the near-infrared galaxies that are most likely to be the counterparts to the *Herschel* galaxies. I accomplish this by using a likelihood ratio method which I modify to allow for an appropriate estimate of the probability of finding a genuine near-infrared counterpart above the magnitude limit to a SPIRE source. This probability is found to be $Q_0 \approx 0.73$. 51% of the SPIRE sources have a best VIKING counterpart with a reliability R = 0.8, and the false identification rate of these is estimated to be 4.2%. I expect to miss ∼5 per cent of true VIKING counterparts. There is evidence from Z - J and J - K_s colours that the reliable counterparts to SPIRE galaxies are marginally redder than the field population.

I obtain photometric redshifts for ∼ 68% of all (non-stellar) VIKING candidates with a median redshift of $\tilde{z} = 0.405$. I have spectroscopic redshifts for 3147 (∼ 28%) of the reliable counterparts from existing redshift surveys. Comparing to the results of the optical identifications supplied with the Phase I catalogue, I find that the use of medium-deep near-infrared data improves the identification rate of reliable counterparts from 36% to 51%.

I investigate the evolution of the sub-millimetre luminosity function (LF) using the sample of SPIRE sources with reliable counterparts in VIKING with $z \leq 1$. I find strong evolution of the 250 μm LF out to about redshift $z = 0.6$ and possibly out to $z = 0.8$ in broad agreement with previous studies. A double-power law seems to fit the local LF ($z \leq 0.2$) slightly better than a Schechter function and we find a flatter slope at lower luminosities as compared to recent studies.

Finally, I construct the star formation rates (SFR) from far-infrared (FIR) and ultra-violet (UV) luminosities of the SPIRE sample with reliable VIKING counterparts ($\mathrm{SFR_{FIR}}$ and $\mathrm{SFR_{UV}}$ respectively) and show that the contribution of the $\mathrm{SFR_{FIR}}$ increases with increasing luminosity. UV observations are hence crucial for all but the brightest SPIRE galaxies in calculating a total SFR. Calculating the slope β of the UV continuum and comparing with the ratio $L_{\mathrm{FIR}}/L_{\mathrm{UV}}$ leads to dust attenuation corrected $\mathrm{SFR_{UV}}$ that represent the total SFR well in the low to medium L_{FIR} range.

Acknowledegments

I am grateful to Will Sutherland for the support and guidance he showed me during the four years of research and the writing of this thesis. I would also like to thank Jim Emerson and Richard Nelson for encouraging me during some difficult periods.

Special thanks go to my colleges Joe Findlay and Chris Watkins which whom I could share, discuss and laugh about some of the more mundane aspects of university life.

A warm thanks goes to my husband Peter for his moral support and for gently edging me on. Special thanks also to my children Marc and Julian who made sure that I never lose contact with reality. I am grateful to my friend Bettina for her emotional support over skype when study isolation syndrome hit and to my friend Cathy dragging me out for coffee.

I would also like to thank my parents who, also they are far away, still managed to encourage me in my work.

I am also grateful to the STFC for the grant I received which enabled me to pursue my PhD.

List of publications

I Kim, S. et al. (2012), SPITZER IRAC identification of HERSCHEL-ATLAS SPIRE sources, ApJ, 756, 28

II Fleuren, S. et al. (2012), *Herschel*-ATLAS: VISTA VIKING K_s selected counterparts in the Phase I GAMA 9h data, MNRAS, 423, 2407

III McAlpine, K., Smith, D. J. B., Jarvis, M. J., Bonfield, D. G., Fleuren, S. (2012) The likelihood ratio as a tool for radio continuum surveys with Square Kilometre Array precursor telescopes, MNRAS, 423, 132

IV Bond, N. et al. (2012), The Mid- and Far-infrared properties of sources matched in the WISE All-Sky and Herschel ATLAS surveys, ApJ, 750, 18

V González-Nuevo, J. et al. (2012), Herschel-ATLAS: towards the detection of $\sim$ 1000 strongly-lensed galaxies, ApJ, 749, 65

VI Smith, D.J.B. et al. (2011), Herschel-ATLAS: counterparts from the UVNIR in the science demonstration phase catalogue, MNRAS, 416, 857

VII Negrello, M. et al. (2010), The discovery of a population of submillimeter-bright gravitational lenses by the Herschel Space Observatory, Sci, 330, 800

Author's contribution to the publications

I Sam Kim, the lead author, applied my new method as outlined in my paper II. I also helped with comments and suggestions on his task of matching SPITZER and SPIRE sources.

II I was solely responsible for the writing of the paper; all figures were created by me; all calculations were performed by me. In this paper I propose a new method of dealing with the estimation of a crucial factor (Q_0) in the matching of two galaxy catalogues at different wavelengths. The paper went through an initial reviewing process within the *Herschel*-ATLAS group; some useful comments and suggestions have been incorporated and their authors have been included in the author list. Will Sutherland has written two paragraphs, has helped with suggestions and has proof-read the paper. Special support was also received from Loretta Dunne in the form of suggestions and advise. Chapters 3 and 4 of this thesis are based on this paper.

III The lead author, Kim McAlpine has invited me to comment on her paper ahead of publication, as she uses the new method as outlined in my paper II. We mainly discussed the high completeness of her data matching.

IV The lead author Nick Bond and I discussed the use of the new method for matching SPIRE sources which he then applied to his WISE data.

V I provided VIKING counterparts plus their photometric redshifts from my matching results to candidates for gravitational lenses selected based on the LF of high redshift SPIRE sources.

VI The lead author, Dan Smith, and I discussed the likelihood ratio method on several occasions. I have contributed with detailed comments and suggestions to his paper in several draft stages.

VII I provided VIKING counterparts plus my derived photometric redshifts from my initial matching results to candidates for gravitational lenses selected based on their number counts.

Contents

List of Figures

List of Tables

Chapter 1

Introduction

Over 200 years ago, in 1800, William Herschel discovered what he called "calorific rays". Measuring the temperatures of the different colours in the visible spectrum from sunlight, he found that the temperature increases with increasing wavelength. This kindled his curiosity and he decided to measure the temperature beyond red, invisible to the eye; he found that it was the highest and he named this invisible radiation "calorific rays" from the latin word "calor" for "heat". We now call those rays "infrared" radiation from the latin word "infra" for "below". The visible (to the human eye) or optical wavelength range extends from 380 to about 760nm; the infrared range is itself divided into near-infrared (NIR, 0.760-5.0 μm), the mid-infrared (MIR, 5-30 μm) and the far-infrared (FIR, 30-500 μm). Longer wavelengths are divided roughly into sub-millimetre (sub-mm), millimetre, microwave and radio bands. The divisions vary widely though and the FIR is often assumed in the range 8-1000 μm and the sub-mm can include wavelengths down to 300 μm. The Sun's emission peaks at a wavelength of 883nm, well within the NIR band, causing Herschel's thermometer to register a peak in temperature beyond the red.

Since Herschel's days, infrared detectors have been developed for a broad range of technologies, from the military (night vision goggles) through medicine (thermography) to weather forecasting (infrared satellites determining temperatures). For the research undertaken for this thesis, applications in the field of astronomy are of course the most important. Before we cover some important infrared telescopes and surveys and some of the breakthrough discoveries made with their help so far in section 1.2, we will outline

the scientific possibilities of infrared astronomy in the next section.

Section 1.3 will supply a short introduction into the cosmology providing the framework for galaxy evolution which is outlined in section 1.4. Section 1.5 talks in more detail about the sub-mm population of galaxies. More detailed introductions to specific topics will be given at the beginning of each chapter.

1.1 Science in the infrared

What is the scientific motivation behind observing the universe in the infrared? The main advantages are related to dust properties and the observation that our universe is expanding.

Edwin Hubble found the first clues to an expanding universe in 1929 when calculating distances to what was then called nebulae and we now call galaxies. He discovered that galaxies are moving away from us with a speed that increases with increasing distance to us, the so-called Hubble law. The light from a moving object gets shifted relative to an observer, with a shift towards the shorter wavelength part of the spectrum if the object moves towards the observer, and the longer wavelength part if the object moves away from the observer. Hence, for galaxies moving away from us, we see a so-called (cosmological) redshift in their spectra. This redshift increases with increasing distance from us and can therefore be used as a good proxy for the distance; see section 5.1.1 for more detailed information on the link between redshift and distance. From about redshift 0.5, at a lookback time[1] of 5 billion years, the visible part of the spectrum gets redshifted into the near-infrared. Infrared observation are hence essential for studying galaxies at higher redshifts. Since light travels at a finite speed, distance is also a proxy for time elapsed and this effectively allows us to observe the past; this is useful indeed when investigating galaxy evolution (see section 1.4).

When observing in the visible wavelength ranges, dust is a major obstacle. It obscures our view through the processes of scattering and absorption of light. Scattering is related to the size a_g of the dust grain in comparison to the wavelength λ. If $a_g \ll \lambda$, the light is scattered approximately isotropically[2]. This is called Rayleigh scattering (after Lord Rayleigh, 1842-1919) and is behind the experience of a blue sky as well as of

[1] The lookback time is the time elapsed since the light was emitted.

[2] Rayleigh scattering only depends weakly on the scattering θ angle as $\propto (1 + \cos^2 \theta)$

a red sunset: the scattering is more effective at smaller wavelengths ($\propto \lambda^{-4}$), so during the day, more blue light from the Sun gets scattered downwards towards us than red light, whereas at the time of sunset, the Sun's radiation travels a proportionally longer path and more blue than red light is scattered away from the direct line of sight. Here, the visible radiation from the Sun is scattered mostly by Nitrogen and Oxygen in the atmosphere. This phenomenon plays a role when observing objects from the ground, but also for space telescopes due to dust in interstellar space. Infrared light is hence much less affected by dust scattering than visible light.

Light can also be absorbed by dust and gas which then enters a higher energy state (i.e. is warmed) and can re-radiate the heat at a later time. Due to absorption being more effective at smaller wavelengths, infrared light is also less subject to absorption by gas and dust. Silicates and hydrocarbon are believed to be the most abundant dust grains in the interstellar medium (ISM) and are responsible for some absorption (and emission) features in the NIR and MIR. Shorter wavelength radiation is absorbed more readily by gas and dust; for example, UV photons from massive young stars can be absorbed by atomic hydrogen and re-emitted again later in any direction, effectively removing radiation from the line of sight. Dust grains are heated when absorbing UV photons and re-radiate the energy at wavelengths depending on factors such as the emissivity of the grains[3] and the incident wavelength. They do not emit as blackbodies; the emission rather follows a so-called grey-body law taking into account the emissivity of the dust[4] . Observations in the longer infrared wavelength band, i.e. the FIR or sub-mm, can hence detect the cool clouds of dust (and gas) that surround stellar nurseries.

The effect of scattering in the optical can be seen in the image of the centre of the Orion nebula, a young star forming region in the Galaxy, Fig. 1.1: the left panel shows an image observed in visible light, the right panel shows the same region in the NIR. The vast majority of possibly proto-stellar objects or very young, small stars, seen as red points in the NIR, are hidden by dust in the optical.

The effect of scattering and absorption together is called extinction and is wavelength dependent, as we have seen above. This generally results in a reddening of

[3]The emissivity ϵ of the dust is the ratio of the energy radiated by the grain to the energy radiated by a blackbody. It depends on the optical depth τ as $\epsilon = 1 - e^{-\tau}$

[4]A grey-body allows for the re-emission of some incident radiation in contrast to a black-body; more details in chapter 6.

Figure 1.1: — The centre of the Orion Nebula and the effect of dust for observing. The **left** panel shows an image taken in the optical, the **right** panel shows an image taken in the NIR by VISTA. Objects that are hidden by dust are revealed in the NIR image. Credit: ESO.

starlight when observing in the optical because the extinction is stronger in the blue than in the red wavelengths. Infrared imaging is hence of great value for dusty objects, including stellar nurseries still embedded in their dusty birthplace (as shown in Fig. 1.1), disks around proto-stellar objects and dusty galaxies. An interesting class of objects are heavily obscured galaxies with high star formation rates where the FIR and sub-mm pick up the characteristic heat of dust warmed by massive, young stars; there is evidence that those galaxies are more numerous in the past and play an important role in our current knowledge of galaxy formation. They will be discussed in sections 1.4 and 1.5.

The next section will introduce some past and current infrared instruments and the scientific discoveries made with them.

1.2 Infrared telescopes and surveys

Infrared radiation is scattered and absorbed by molecules in the atmosphere and infrared observations from the ground have to make use of atmospheric windows where transmission is fairly unhindered. Fig. 1.2 shows the atmospheric transmission from the ultra-violet (UV) to the radio wavelengths. Infrared detectors are therefore sensitive to specific atmospheric windows and use different materials to achieve this sensitivity. The very first infrared detector, the thermometer, is not very practical for most astronomical purposes; military advances during WII resulted in the first useful infrared detector made of PbS (Lead Sulfide), using the photoconductive effect and sensitive to radiation between 1-3 μm. At the end of the 1950s, PbS was replaced by semiconductor alloys one of which is HgCdTe (Mercury Cadmium Telluride) which is still used today albeit in much larger arrays, for example in the VISTA camera. PbS and HgCdTe based detectors are photon detectors where photons interact with bound electrons introducing a current, voltage or resistance change that is measured. Another class of detectors are thermal detectors where a change in temperature induces changes in the physical properties, typically the resistance, of the detector. Bolometers are thermal detectors; the SPIRE instrument on board the Herschel Space Observatory consists of ultra-cooled bolometer arrays, see chapter 3 and Griffin et al. (2010) for more details.

In the 1980s, IR arrays replaced the single pixel detectors used until then for infrared observations. They are much more sensitive, allowing for decreases in exposure time, and exhibit a larger dynamic range so that under- or overexposure is less likely.

The atmospheric windows in the NIR, see Fig. 2.1, allow for ground-based NIR telescopes with detectors sensitive to the appropriate wavelength range. In fact, some optical telescopes, like the Keck Observatory in Hawaii and the dedicated Sloan Foundation telescope in New Mexico, also make use of the windows to extend their observing capabilities into the NIR up to 1 μm. Several photometric systems[5] have been constructed since the start of astronomical infrared observations, starting with the extension of the Johnson & Morgan broadband filters UBV (Johnson & Morgan, 1953) to include the RI bands where the I band has an effective wavelength of about 800nm

[5] A photometric system is comprised of a number of filters each with a known sensitivity to incident radiation, together with a set of standard stars to supply standard magnitudes and colours (magnitude differences between different wavelength bands) for the calibration of measured flux.

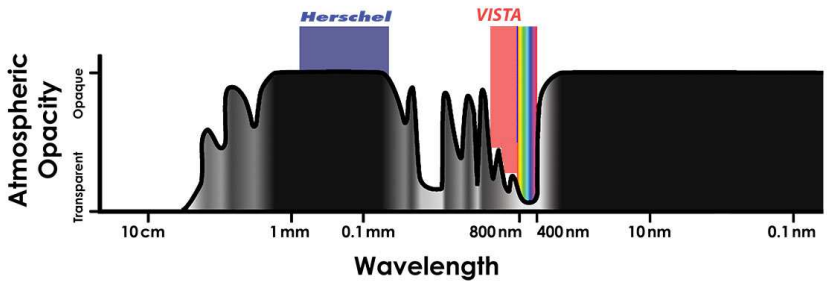

Figure 1.2: — The large scale atmospheric transmission in the wavelength ranges X-ray to radio. The atmosphere is transparent in the optical and shows intermittent absorption features and windows in the NIR, labeled with 'VISTA'. Many different absorption features are left out for clarity, but can be seen readily in Fig. 2.1, showing the transmission function of VISTA in the NIR. In the wavelength bands in which *Herschel* observes, the atmosphere is opaque to the radiation, hence the need to observe from space. The small atmospheric windows at 450 and 850 μm at which SCUBA observes are not displayed; the high altitude of SCUBA ($\sim$ 4000m) means that the observations are less affected by the water vapor which is responsible for the majority of the atmospheric absorption at these wavelength ranges.

(Bessell, 1979), to the creation of the near-infrared specific $JHKLM$ filters (Bessell & Brett, 1988), see table 2.1 for the VISTA specific filters $ZYJHK_s$.

A large infrared survey of lasting scientific impact is 2MASS (two Micron All Sky Survey) using 2 dedicated telescopes, one in Arizona and another in Chile to cover both hemispheres, and each using a 256x256 HgCdTe detector, and completed in 2001. It mapped the sky in the 3 NIR bands JHK_s providing a huge database of infrared objects. 2MASS detected a new class of objects, the coolest brown dwarfs[6] at the time, of spectral class "L" (Kirkpatrick et al., 1999), with temperatures $\sim 1500 - 2000$K (Reid et al., 1999). Here, the NIR is not only important to detect the radiation from such low temperatures, but also to distinguish the brown dwarfs from high-redshift QSOs and to measure absorption bands from characteristic metals in the atmospheres of the brown dwarfs.

Another ground-based telescope with far reaching impact is the UKIRT (United Kingdom Infrared Telescope) on Mauna Kea in Hawaii, a 3.8m telescope using a wide field camera (WFCAM) consisting of 4 HgCdTe arrays, 2048x2048 each, with a field-of-view (FOV) of 0.19deg^2, operating in the 4 photometric bands $YJHK$. The UKIRT Infrared Deep Sky Survey (UKIDSS) started in 2005 (Lawrence et al., 2007), and mapped 7500 deg^2 of the northern hemisphere in varying depths, generally 3 magnitudes deeper than 2MASS. Some of the science highlights from UKIDSS are the detection of the most distant quasar to-date at $z = 7.08$ (Mortlock et al., 2011) and the discovery of the coolest brown dwarfs at the time (Lodieu et al., 2009) with temperatures < 1000K. VISTA, the latest NIR ground telescope is situated at the ESO Paranal site and has been operating since October 2009. The VISTA filters are very similar to the WFCAM filters with the exception of the K_s filter, see section 2.0.1 for more detail. Six large public surveys (Arnaboldi et al., 2007) are conducted with VISTA, see Fig. 1.3, varying in depth and breadth, one of which is VIKING, of medium depth and over 1500deg^2. First data releases have been made public (Arnaboldi & Retzlaff, 2011) and first science results include the detection of T-dwarfs (Lodieu et al., 2012) and the construction of selection constraints for high-redshift QSO (Findlay et al., 2012) as well as the identification of VIKING counterparts to *Herschel*-ATLAS objects (this work).

[6]Brown dwarfs are objects of mass $< 0.08M_\odot$, the theoretical limit for hydrogen ignition; they radiate in the infrared with a peak wavelength proportional to their temperature and are often not detectable in the optical.

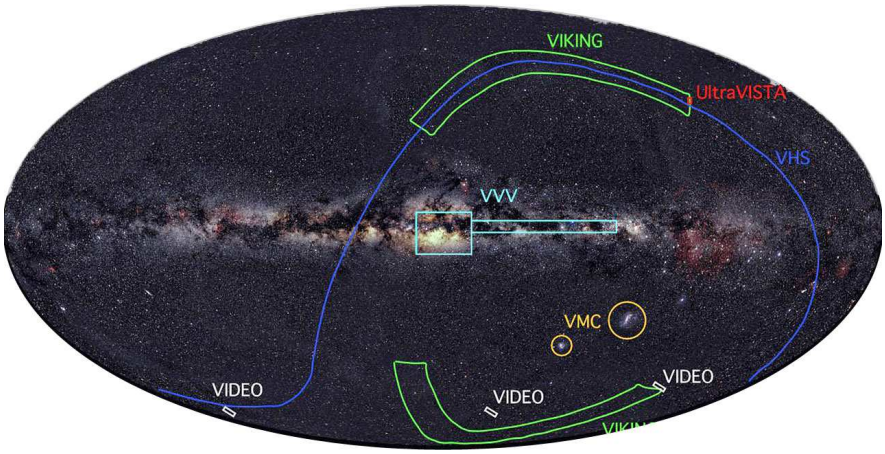

Figure 1.3: — Sky coverage of the six VISTA public surveys on the sky. Credit: ESO.

At longer wavelengths, our atmosphere becomes increasingly opaque to the infrared radiation. Some narrow windows have been exploited with the Submillimetre Common-User Bolometer Array (SCUBA, Holland et al., 1999) on the JCMT (James Clerk Maxwell Telescope) on Hawaii, operating since 1997. It uses two arrays of bolometer detectors to observe at 450 and 850 μm with a FOV of 2.3arcmin^2. A very successful survey with SCUBA has been SHADES (SCUBA HAlf Degree Extragalactic Survey) (Mortier et al., 2005) investigating the population of high-redshift dusty galaxies believed to undergo high rates of star formation (e.g. Dye et al., 2008; Serjeant et al., 2008; Takagi et al., 2007). The sub-mm wavebands are ideally placed to select high redshift cool galaxies because of the strong negative k-correction[7] at those wavelengths, see Fig. 1.4. SCUBA is being replaced by SCUBA-2, currently commissioning, using more cutting edge technology bolometers that provide more pixels and an increase in the FOV to 50arcmin^2.

Most of the MIR, FIR and sub-mm is absorbed by our atmosphere and we have to

[7]The k-correction is a flux density correction factor (in the case of magnitudes, it is an additional term) to take the $(1+z)$ shift in wavelengths bands into account; for example if we observe some flux in the NIR broad band J and the galaxy lies at $z = 1$, the rest-frame, i.e. emitted, wavelength is situated in the optical R band. The magnitude k-correction is generally positive, so that the source becomes fainter with redshift; a "negative" k-correction means then that the source is brighter in the rest-frame at higher redshifts, as can be seen in Fig. 1.4. A theoretical treatment of k-correction is supplied by Hogg et al. (2002)

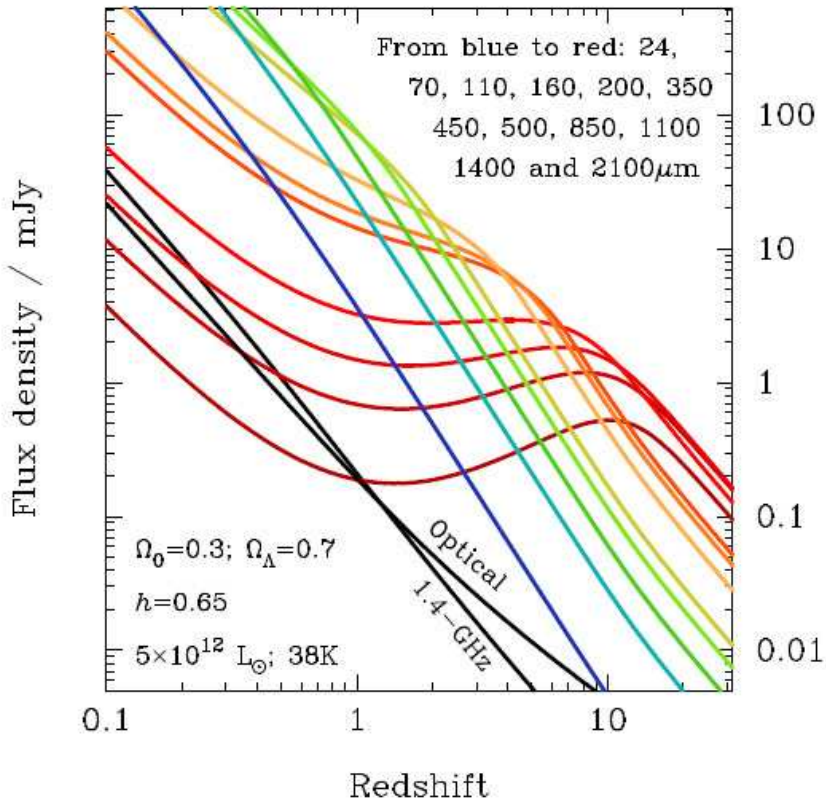

Figure 1.4: — Predicted flux density of a typical distant sub-mm-selected galaxy. At longer wavelengths, the flux density is nearly independent of the redshift for $1 < z < 10$. This phenomenon is termed negative k-correction and allows for the detection of those galaxies out to high redshifts. Credit: Blain et al. (2002), their fig.4.

send telescopes into space to observe in those wavelengths. The first and very successful IR space telescope was IRAS (InfraRed Astronomical Satellite[8]), observing at 12, 25, 60 and 100 μm and starting operation in 1983 (Clegg, 1980). In its 10 months survey time it detected around 25,000 galaxies at 60 μm, of which only $\sim$ 50% were already listed in optical catalogues, six new comets and, most interesting for our purposes here, discovered a high number of starburst galaxies (Soifer et al., 1987), i.e. galaxies with very high star formation (few $M_{\odot}yr^{-1}$ to $10^3 M_{\odot}yr^{-1}$) detectable in the infrared by warm dust emission. Those starburst galaxies were often of irregular shape consisting of two merging galaxies; the merging of the gas and dust is believed to be the trigger of an intense star forming burst. The fraction of mergers and interacting systems increases with increasing FIR luminosity (Sanders et al., 1988). Comparing the radio/FIR ratio of IRAS galaxies, studies discovered the tight correlation between radio and FIR, thought to be due to the synchrotron emission of supernova remnants (e.g. Dickey & Salpeter, 1984; Unger et al., 1989). Sanders et al. (1988) find that the fraction of AGN (Active Galactic Nuclei) increases with increasing luminosity and propose that ULIRGs (Ultra luminous infrared galaxies, $L \geq 10^{12}$) represent the early, hidden (by dust) stages of QSO. Smith et al. (1998) find that $\sim$60% of LIRGs (Luminous Infrared galaxies, $L \geq 10^{11}$) harbour AGN, but note that starburst generated supernovae could in some cases mimic the observed AGN radio signature. IRAS produced large databases of which the PSC (Point Source Catalogue) is the biggest with nearly 250,000 objects.

Building on the success of IRAS, the Infrared Space Observatory (ISO)[9] was launched in 1995 (Kessler et al., 1996). ISO was able to observe in the wavelength range 2.5 to 240 μm, extending further into the longer wavelengths than IRAS and hence into higher redshifts. A direct comparison between the local flux density counts from IRAS and the counts at higher redshifts with ISO showed an excess of infrared luminous galaxies (that are optically faint) in the past. Follow-up redshift surveys placed the starburst galaxies at redshifts $z > 1$ with a peak at $z \simeq 2$ helping in constructing the "downsizing" scenario in galaxy evolution (Cowie et al., 1996), see section 1.4 for more detail. This discovery was also confirmed by 850 μm number counts from SCUBA (Hughes et al., 1998; Smail et al., 2002) and HST observations (Chapman et al., 2003) and the evidence of strong dust extinction using the UV slope method of Meurer et al. (1999).

[8] IRAS was a joint project of the US, UK and the Netherlands.

[9] An ESA project with the participation of ISAS and NASA

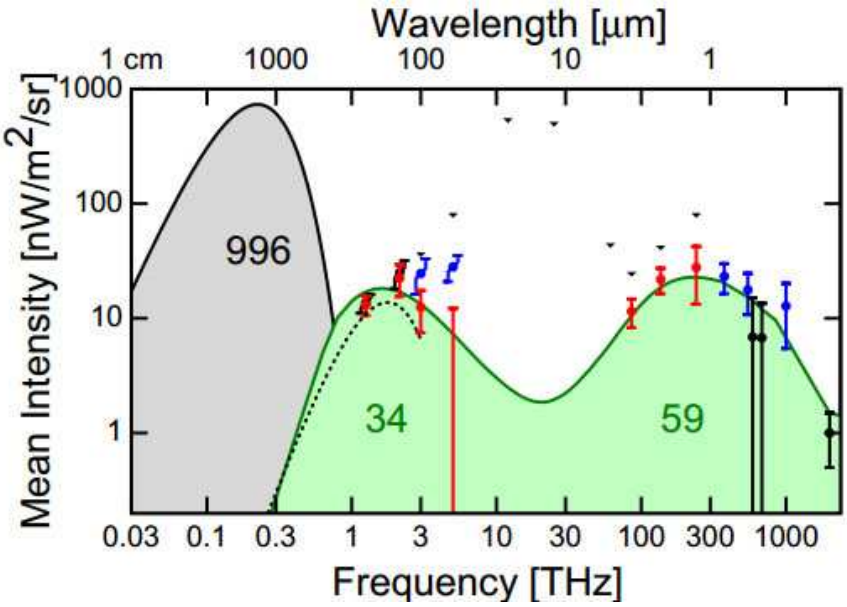

Figure 1.5: — The mean intensities from the optical to the microwave as measured by HST (optical/near-infrared) and COBE (microwave and far-infrared). The numbers in the bumps are the integrated intensities. The energy density for the CMB (Cosmic Microwave Background, grey) is about an order of magnitude higher than that for both the CIRB (Cosmic Infrared Background, left green bump) and the optical background (right green bump) together. The CIRB and optical backgrounds are of similar energy density. This is evidence that around half of the starlight in highly starforming regions is absorbed by dust and then re-radiated in the FIR at a rest-frame peak of about 100 μm. Credit: fig.1 from Wright (2004).

The detection of a cosmic FIR background (CIRB Puget et al., 1996; Wright, 2004) with the Cosmic Background Explorer (COBE) satellite also added evidence to the scenario of an excess FIR in the past; the CIRB turned out to be at least as strong as the background from stellar emission (UV to NIR) whereas the local galaxies only emit about 30% of their total radiation, the bolometric luminosity, longward of the NIR (Elbaz, 2005). Fig. 1.5 shows the mean intensities found with COBE: bumps represent the Cosmic Microwave Background (CMB, see section 1.3), the CIRB which peaks at around 100 μm and the Optical Background. In the NIR, NASA's Hubble Space Telescope (HST) includes some observing capabilities: NICMOS (Near Infrared Camera and Multi-Object Spectrometer) was installed in 1997 and operates in the wavelength

range 0.8-2.5 μm. The wide-field cameras (now WFC3, installed 2009) include filters up to 1.9 μm. The Advanced Camera for Surveys (ACS, installed 2002) longest wavelength filter operates at 850nm; the observations of the Hubble Ultra Deep Field (HUDF) did include 150 orbits using this filter, as well as 100 orbits each for the NICMOS 1.6 and 2.0 μm filters[10].

The Spitzer Space Telescope started its operation in 2003; after the exhaustion of the liquid helium supply for the cooling of the instruments in 2009, Spitzer is still able to observe at the shortest wavelengths 3.6 and 4.5 μm in the so-called warm mission. For our purposes, two instruments are of interest: IRAC (InfraRed Camera), operating at 3.6, 4.5, 5.8 and 8 μm and MIPS (Multiband Imaging Photometer for Spitzer) for the wavelength bands centered on 24, 70 and 160 μm. The warm mission has been used just recently to detect an exoplanet two-thirds the size of Earth by a dip in its near-infrared lightcurve (Stevenson et al., 2012). In the realm of galaxy formation, Spitzer was able to confirm the downsizing scenario and to quantify it further using MIPS to detect high redshift dusty galaxies (Pérez-González et al., 2010). Spitzer detected galaxies have been subjected to follow-up observations and spectroscopy, finding for example that $\sim$ 22% of 24 μm detections in a small southern field of 4 deg^2 are AGN (Sacchi et al., 2009) or enabling the calculation of photometric redshifts and the determination of luminosity functions (Rodighiero et al., 2010).

The Balloon-born Large-Aperture Submillimeter Telescope (BLAST) has been designed as a precursor to the SPIRE instrument on board *Herschel* with receivers at 250, 350 and 500 μm allowing for the detection of the dusty peak at rest-frame 100 μm at higher redshifts. BLAST flew successfully several times until 2010. The positional uncertainty at those long wavelength is relatively high; Dye et al. (2009) find radio counterparts with accurate positions to 57% of 250 μm selected BLAST sources which enables the follow-up with HST and Spitzer to compile multi-wavelength catalogues. Dunlop et al. (2010) examine the 20 brightest sources with multi-wavelength data and conclude that they are a mixture of low-redshift spirals and LIRGS and higher redshift dusty starburst with a median redshift of $z \simeq 1$. Chapin et al. (2011) find a median redshift of $z = 1.1$ and a median temperature of 30K for a BLAST sample cross-matched

[10]The HUDF is the successor of the HDF which started as an experiment in 1995 pointing the HST at a dark patch of sky 2.5 arcmin across for 10 consecutive days with stunning results.

with observations at 870 μm. The results seem to give support to the theoretical assumption that bands of increasing wavelength are able to detect increasingly cooler galaxies at increasingly higher redshifts.

BLAST is especially interesting for the purposes of this thesis, because the *Herschel* SPIRE instrument is built on BLAST's blueprint, with improvements in the resolution of a factor of two. Still, the positional accuracy is of the order of a few arcsec, making it challenging to select optical and near-infrared counterparts, so useful for determining redshifts, luminosities, masses etc. A first and important step in profiting from the SPIRE observations is hence the cross-matching with observations in shorter wavelength, in the absence of radio data, and the determination of photometric redshifts, both a large part of the work undertaken for this thesis.

Finally, a new mid-infrared space telescope has been launched in 2009: WISE (Wide-field Infrared Survey Explorer), observing in 3.4, 4.6 and 12 μm with a resolution of around 6 arcsec. The WISE catalogues have recently been cross-matched to *Herschel* sources (Bond et al., 2012), using techniques described here.

As can be seen in Fig. 1.5, the evolution of galaxies can only be explained when adding the crucial far-infrared component, the hidden star formation; this is discussed in section 1.4. Multi-wavelength catalogues are of enormous value in piecing together the history of galaxies and our universe.

We give a short introduction into the current knowledge of the birth and evolution of our universe as a whole in the next section, before we debate in more detail how individual galaxies are believed to have been seeded in the early universe and the manner in which they grew.

1.3 Cosmology

Cosmology is the study of the universe as a whole. This includes its birth, evolution, size, shape and its eventual demise. It provides the framework in which galaxy evolution plays out and supplies a quantitative tool for distance measurements; it is hence important for this work.

Modern cosmology started with the discovery that galaxies, then classified as nebulae, are extra-galactic, the so-called "island universe" theory already favoured by Slipher (1917) measuring velocities of 25 nebulae and confirmed by Hubble (1926). Being able

to deduce the distances to some nebulae with high velocities from Cepheid light curves, (Hubble, 1929) discovered that they are speeding away from us with a speed that is directly proportional to its distance from us. From the Copernican principle which states that we do not occupy a privileged position in the universe, we have to follow that this behaviour is observed from every point of the universe; it is comparable to the stretching of a large rubber sheet or the inflation of a balloon.

Comparing the redshift z and the distance d of a galaxy, Hubble derived his law:

$$v = H_0 \times d \tag{1.1}$$

where v the recession velocity with $v = cz$ for $z \ll 1$ and H_0 the Hubble constant. A unitless way to describe the Hubble constant is: $H_0 = 100 \times h\,\mathrm{km\,s^{-1}\,Mpc^{-1}}$. Observational evidence suggests that $h \simeq 0.7$ (Spergel et al., 2007); this is the value used in this work unless stated otherwise. This "constant" does vary with time with H_0 being the value at the current time t_0; the more general parameter is the Hubble parameter $H(t) \equiv \dot{a}(t)/a(t)$, depending on the scale parameter $a(t)$ which is a measure of how much space is stretched at time t with respect to t_0. With the help of the scale parameter, we can introduce co-moving coordinates that move with the expansion so that the position of a galaxy stays fixed in those coordinates. The scale parameter translates then between co-moving coordinate and distance.

The discovery of the expansion of our universe also allows a backward thought experiment: further back in the past all galaxies in the universe must have been much closer together. From those considerations, the Big Bang theory was born, the idea that the whole universe was born from an infinitely dense environment in the past. The Big Bang theory is now strongly supported and we have strong evidence that our universe was born 13.7 billion years ago from a dense and hot singularity, expanding and cooling down ever since. The most compelling evidence is provided by the CMB (Cosmic Microwave Background, see also section 1.2 and Fig. 1.5); theoretical reflections about early thermonuclear reactions led to the conclusion that if the Big Bang is indeed true, then we should be able to detect the afterglow of its birth at the temperature of a few Kelvin, corresponding to a peak at a few mm wavelength of a blackbody spectrum, in the microwave range. This prediction by Alpher et al. (1948) was not taken particularly serious until the CMB was discovered serendipitously in 1965 (Penzias & Wilson, 1965), silencing in one stroke most opponents to the Big Bang theory.

Einstein had laid the theoretical foundations of mathematical cosmology in 1905 and 1916 with the special and general theory of relativity. From then on, space and time were intrinsically linked together, expressed in the notion space-time. The geometrical interaction between matter and space-time gives rise to gravity, a phenomenon that Newton could predict but not explain. Space and time are linked by a metric. The simplest metric is a three-dimensional generalisation of Pythagoras' theorem that also includes the time axis. This assumes that we live in a flat universe, i.e. a world in which the three angles of a triangle add up to 180 degrees. We can also imagine a curved universe: with a positive curvature where the angles add up to a sum that is greater than 180 degrees (closed universe, e.g. a sphere) or with a negative curvature where the sum is smaller than 180 degrees (open universe, e.g. a saddle). All three scenarios had been contemplated as possible, each of them predicting a different future for our universe: a closed universe would lead to an eventual slowing of the expansion followed by a collapse, a flat universe would slow indefinitely, but never actually stop expanding, and in the open case, the universe would continue to expand forever.

The theoretical model of our universe includes three key parameters: the Hubble parameter $H(t)$ (or its current value H_0), the Ω- or density parameter and the deceleration parameter q_0. We have already introduced the Hubble parameter and explain now the concept of Ω, after which we will shortly cover q_0. Ω is closely related to the so-called critical density ρ_{crit} which is the density of matter in the universe needed for it to be flat; we know that gravity plays an important role and the amount of matter will dictate how much gravity is exerted and how the universe behaves. ρ_{crit} is just the right amount to keep the expansion going, but at an increasingly slower rate. To distinguish different kinds of density parameters, we introduce here Ω_m, the matter density of the universe. The Ω_m-parameter is defined as the ratio of the matter density to the critical density:

$$\Omega_m(t) = \frac{\rho(t)}{\rho_{crit}(t)} \qquad \text{where} \qquad \rho_{crit}(t) = \frac{3H^2(t)}{8\pi G} \tag{1.2}$$

where G is Newton's gravitational constant. The value[11] of Ω_m indicates therefore how our universe will behave in the future: if $\Omega_m \leq 1$ it expands forever if $\Omega_m > 1$

[11] The usual practice is to use the terms Ω_m, ρ etc. for present-day values and specify the time t only if different from now.

it re-collapses eventually. From calculations on primordial nucleosynthesis we expect that visible matter only constitutes a fraction of around 4% of the energy density, i.e. $\Omega_m \sim 0.04$ which is what is directly measured in the observable universe, and is insufficient for a flat universe with $\Omega = 1$. Many lines of evidence, of which the dynamics of galaxy clusters was the first, suggest though that there is a large amount of matter we cannot see because it doesn't interact with electromagnetic radiation, so-called dark matter. We can deduce the amount of dark matter that should be in our universe for example by observing the rotational behaviour of galaxies and galaxy clusters, which cannot be explained by visible matter alone. The nature of dark matter particles is still not entirely clear, but we now rule out the hot version, fast moving neutrinos, in favour of slow moving dark matter, i.e. cold dark matter, and also find evidence that dark matter is non-baryonic[12]. It is estimated that the dark matter density $\Omega_{dm} \approx 0.26$; with the density for baryonic matter $\Omega_b \approx 0.04$ we hence conclude that $\Omega_m \approx 0.3$. However, temperature fluctuations in the CMB measured from balloon-borne experiments (Balbi et al., 2000; de Bernardis et al., 2000), suggested that our universe has a flat geometry and we should measure $\Omega_m \simeq 1$. A value of a total Ω close to unity seemed to pose a problem though when using the Friedmann equation; we can show that the value of $\Omega(t_{nuc})$ at the time of nucleosynthesis, i.e. when the universe was about 1 sec old, must have been within 10^{-17} of unity to be able to explain a value close to unity today. This high amount of fine-tuning to explain current values seemed unsatisfactory. Help came in the form of the theory of cosmic inflation (Guth, 1981): a period of intensely accelerated expansion (i.e. inflation) in the early universe which pushes $\Omega(t_{nuc})$ towards unity. The values of $\Omega_m \approx 0.3 - 1$ were hence plausible and predicted that we live either in an open or a flat universe, but that expands forever.

The total energy content of the universe remained uncertain until the end of the last century when two teams of researchers announced results from studies with Type 1a supernovae that changed our outlook on the matter density again (Perlmutter et al., 1999; Riess et al., 1998). Type 1a supernovae can be used as standard candles because it is believed that they all attain the same maximum brightness during the explosion. They showed that more distant Type 1a supernovae were fainter at a given redshift than was expected from Hubble's law for local Type 1a supernovae implying an acceleration

[12] Baryonic particles are made of quarks; this includes protons and neutrons. Non-baryons are either leptons, such as neutrinos, or an entire new class of particles.

of the expansion of our universe. This result was surprising indeed, as the researchers believed that the expansion is slowing down due to gravity and had set out to quantify the deceleration parameter q_0, a dimensionless measure of the rate at which the universe is slowing down.

Einstein introduced the so-called cosmological constant, denoted Λ, in 1917 to ensure his field equations would lead to a stable universe, i.e. neither contracting nor expanding, as was believed to be true at the time. A positive value of Λ does imply some sort of repulsion that would effectively overcome gravity. Λ had generally been assumed to be zero, but the discovery of an accelerating universe led to the belief that the value of Λ might be positive to explain the acceleration. Other explanations, apart from assuming a positive cosmological constant, include the postulation of a "vacuum energy" and the supposition of a modification of Einstein's theory of gravity. The jury is still out on what exactly causes the observed acceleration of the expansion of the universe; we call the underlying, unknown force "dark energy" and denote its energy density with Ω_Λ.

Strong evidence from the Type 1a supernovae (see above), the measurement of the CMB (BOOMERanG and WMAP Komatsu et al., 2011; Spergel et al., 2007) and redshift surveys (2dF Galaxy Redshift Survey: e.g. Cole et al., 2005; Colless et al., 2001; Percival et al., 2001 or SDSS: e.g. Tegmark et al., 2004; York et al., 2000) place constraints on the total value of Ω and its constituents; the favoured values are currently $\Omega \approx 1$, $\Omega_m \approx 0.3$ and $\Omega_\Lambda \approx 0.7$ confirming that we live in a flat universe. Those values are now generally used in the calculations of distance and luminosity.

All of the above is now encapsulated in the idiom of standard cosmology that we live in a ΛCDM (lambda cold dark matter) universe. In this model, the geometry is flat (i.e. Euclidian) and dominated by dark energy ($\sim 70\%$) that is responsible for the recent acceleration of the expansion; visible, or baryonic matter is only a small fraction of the matter ($\sim 4\%$) and galaxies live in dark matter halos providing the remaining 25-30% of the energy density. The implications for a theory of galaxy evolution are detailed in the next section.

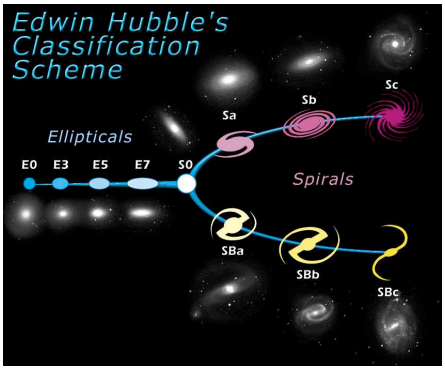

Figure 1.6: — Hubble's galaxy classification scheme, the "tuning fork". The ellipticals are arranged from left to right according to their "ellipticity", a measure that also depends on the observed angle. S0 galaxies display a central bulge and a disk, but no arms and are also called "lenticular" galaxies. Galaxies that do not fit into this scheme are classified as "irregulars". Credit: skyserver.sdss.org

1.4 Galaxy formation and evolution

Since Hubble firmly placed the galaxies outside the Milky Way, they have been regarded as the building blocks of our universe, forming bigger structures such as clusters and filaments that provide the fabric of our universe. Any theory on galaxy formation should be able to explain the observed diverse properties of galaxies, including their sizes and shapes, the supermassive black holes at the centres of a significant fraction of galaxies (AGN), the ranges in luminosities, the luminosity function (representing galaxy number counts depending on luminosity) and the star formation rates. Hubble was one of the first to classify galaxies based on morphology with the most basic differentiation into ellipticals and spirals (Hubble, 1926), see Fig. 1.6. This classification scheme, also called the Hubble tuning fork, suggested at first an evolution from ellipticals to spirals which resulted in ellipticals often called early-type and spirals late-type galaxies. There is no evidence for such an indicated evolution though; in effect, there is more evidence to suggest that any evolution would progress in the opposite way, as we will see shortly. The early and late terms stuck though, unfortunately.

Galaxy morphology is also related to other properties, such as colour, mass, dust/gas content etc. Local early-type galaxies tend to be more massive, redder and devoid of gas or dust, effectively unable to sustain further star formation and hence evolving passively

with an aging stellar population. Local late-type galaxies tend to be smaller, bluer, with varying amounts of gas and dust fueling ongoing star formation in their spiral arms. Galaxy properties also depend on their environment, for example in denser regions, such as in the cores of big clusters, we find predominantly early-type galaxies. We also observe a smooth increase with redshift in maximum luminosity at which rapid star formation takes place up to redshifts $z \simeq 2$, the "downsizing" scenario (Cowie et al., 1996). The downsizing effect is not limited to only luminosity and star formation, but is also seen in relation to AGN activity. The higher redshift universe seems hence generally different from what we observe in the local universe: intense star formation occurring in high mass galaxies coupled with a higher fraction of AGN at high redshifts as compared to the universe of today where star formation is mostly confined in smaller spirals and where the AGN fraction has decreased. We also observe different metallicities[13] of early- and late-type galaxies that are believed to originate from different starforming patterns: observed metal ratios of early-types can be explained by a single starburst and subsequent passive evolution whereas the ratios in late-type galaxies depend on continuous star forming through gas infall. HII rotation curves of galaxies have shown a flattening at high radius incompatible with Newtonian theory of gravity (or Einstein's), but can be explained if we assume that galaxies reside in massive dark matter halos (see section 1.3).

Unfortunately, we cannot follow a single galaxy backwards in time and observe how it evolved; but any reasonable theory of evolution should be able to re-create the observed properties of a galaxy population at a given redshift.

In the framework of a ΛCDM universe (our standard or concordance model, see section 1.3), galaxy formation and evolution plays out as follows. From COBE observations, it was clear that the CMB temperature varies slightly depending on position in the sky; those temperature fluctuations, or anisotropies, were measured with improved sensitivity with WMAP (Wilkinson Microwave Anisotropy Probe), launched in 2001 (Spergel et al., 2007; Wright, 2003).

From the anisotropies, we can deduce that the size of baryon density perturbations at the end of inflation is of the order of 10^{-5} in relation to the baryon density. During the next ∼300,000 years those perturbations did not grow because matter and radiation were still interacting, the outward pressure from the radiation matching the tendency

[13] Astronomers regard any element heavier than helium as a metal.

of matter under gravity to collapse. This differs for non-baryonic dark matter: it does not interact with radiation and any initial density perturbations can grow unhindered by radiation pressure[14]. After about 300,000 years, at $z \sim 1100$, the epoch of recombination, the universe was cool enough for atoms to form and radiation uncoupled from baryonic matter causing baryonic perturbations to grow now under the influence of gravity. The baryonic clumps are attracted to the dark matter clumps which are already much larger, allowing the former to grow at a faster rate than would have been possible without the existence of the latter. Without the dark matter clumps, baryonic matter would not have been able to grow at a fast enough rate to develop into the galaxies we see at the present epoch, further evidence for the existence of non-baryonic dark matter. Computer models (e.g. the Millennium Simulation, see Springel et al., 2005) that evolve the initial dark matter perturbations find great consistency with the large scale structure observed at the present.

How do the dark matter halos and their embedded baryonic matter evolve within the ΛCDM framework? The subsequent evolution is governed by gravity attracting matter to overdense regions and causing collapse under self-gravity. During collapse, the gas inside the halo, the baryonic matter, is shock-heated; the amount of gas able to cool puts an upper limit on the (baryonic) mass of the galaxy forming from the cooling gas cloud. The conservation of angular momentum leads to the formation of a circular disk. As a result, the centre of the halo is very dense and the disk drags the halo dark matter gravitationally, explaining the rotation curves measured. Disk global instabilities aid the formation of large molecular clouds from which stars can form by collapse of local overdensities. The star formation can be kept up by continuous infall of gas from the outer regions of the halo and bulges or bars can form as a consequence of angular momentum re-distribution. Within the ΛCDM scenario, it is found from simulations that smaller objects collapse first which leads to the suggestion that the galaxies and halos we observe today were formed by subsequent mergers, building up hierarchically. Mergers are observed with increasing numbers at increasing redshift, beautifully twisted pairs of galaxies such as the Antennae or the Mice galaxies, lending credence to the hierarchical model of galaxy evolution. When disk galaxies merge, they form spheroids; if the original spirals still contained enough gas, a so-called "wet" merger, or the galaxy can still accrete gas from outside in the halo (both more likely at

[14]The dark matter perturbations can only grow once the universe is matter-dominated, at $z \sim 3200$

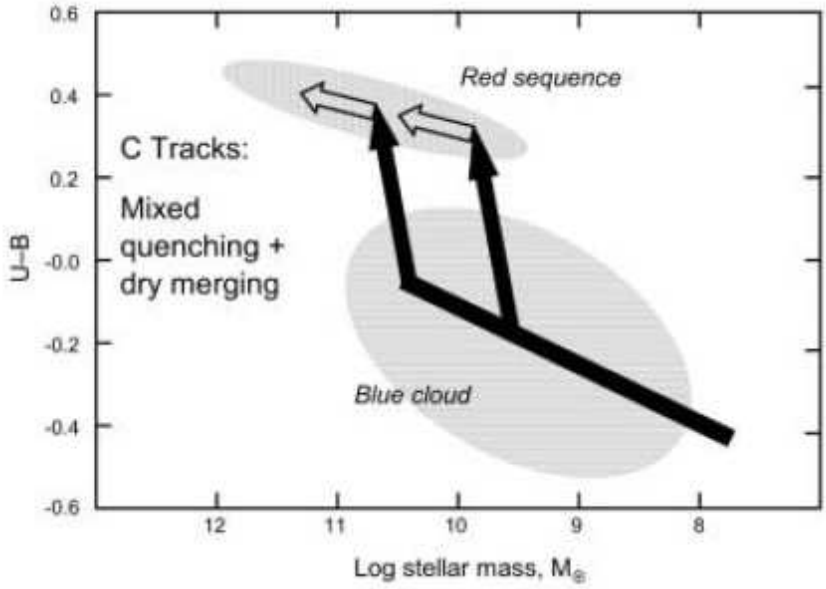

Figure 1.7: — Evolutionary paths from the Blue Cloud to the Red Sequence. Two tracks are considered to both contribute to the observed galaxy distribution: spirals with low gas content in the Blue Cloud merge and the resulting galaxy moves onto the Red Sequence; there it can gain further mass through dry mergers. This path is represented by the right arrow. Spirals with high gas content can be involved in several wet mergers before moving onto the Red Sequence; a path indicated by the left arrow. Credit: Faber et al. (2007), their fig.10.

higher redshifts), a new disk can form again through the process of angular momentum re-distribution. In dense environment facilitating mergers, such as at the cores of galaxy clusters, we should hence find predominantly large spheroids; this is exactly what we observe.

The schematic in Fig. 1.7 shows the evolution of the galaxy population from blue, i.e. late-type spiral, (in the "blue cloud") to red, i.e. early-type spheroid, (into the "red sequence"). Several mechanisms have been evoked to explain this shift. A galaxy is involved in a number of wet mergers, building up its mass, before star formation is quenched (e.g. through the lack of available gas) and it moves to the red sequence where it might build up more mass through "dry" mergers, i.e. mergers without gas; this is indicated by the left vertical arrow in Fig. 1.7. Alternatively, a galaxy's gas expires early, it moves onto the red sequence and aquires more mass through dry mergers. Faber et al. (2007) find that a mixed scenario, involving both mechanisms, matches the properties of distant and local ellipticals best.

How can this scenario explain the downsizing effect we observe, i.e. the increase with redshift in maximum luminosity at which rapid star formation takes place? From about redshift $z \simeq 1$, we observe a high number of massive galaxies undergoing rapid bursts of star formation depleting their gas whereas it is the rather smaller galaxies, spirals and some ULIRGS, undergoing bursts today; it seems rather anti-hierarchical, implying that massive ellipticals formed earlier than the smaller spirals, but it still fits into the ΛCDM model if we consider what happens in dense environments. Gas-rich disk galaxies there merged early, forming massive ellipticals early, leading to a strong starburst obscured by dust; the central black hole grows through gas accretion resulting in a luminous AGN phase. Hence we detect LIRGS and ULIRGS in the sub-mm at this epoch and predominantly in the cores of galaxy clusters. The early formation of massive ellipticals and subsequent rapid star formation also leads to the observed metal ratios.

The ΛCDM paradigm seems hence capable of explaining roughly what we observe. There are a number of more detailed evolutionary processes that are an active field of research, such as the issue of ellipticals in the field (e.g. Geha et al., 2012; Tonnesen & Cen, 2012), the passive evolution of galaxies in the red sequence (e.g. Salim et al., 2012; Skelton et al., 2012), or investigations on the transformation of galaxies from the

blue cloud to the red sequence, transiting the so-called "green valley" (e.g. Gonçalves et al., 2012; Krause et al., 2012).

1.5 Sub-mm Galaxies

The term "sub-mm galaxy" is used for a class of galaxies detected by sub-mm instruments and has been introduced for galaxies first detected with SCUBA. It is generally used more loosely now, including galaxies detected at lower wavelengths, e.g. the *Herschel* detected galaxies are also included in this class. In this short section we summarize our current knowledge about sub-mm galaxies, some of which has already been discussed in earlier sections, especially in the last section, but is focused here around this special class of galaxies and its importance.

IRAS detected a local ($z < 0.3$) population of infrared luminous and ultra-luminous galaxies (LIRGs and ULIRGs); these are some of the most luminous galaxies in the local universe, radiating most of their energy in the FIR and exhibiting either highly-obscured star formation or AGN activity. The vast majority of IRAS galaxies are gas-rich spirals and a significant minority show evidence of interacting, but their overall contribution to the local luminosity density is rather small. The discovery of this class spiked an interest in the higher redshift equivalents of such extreme galaxies. For an excellent overview of IRAS galaxies, see Soifer et al. (1987).

First results from ISO showed that the number density of IR luminous galaxies was much higher in the past; even though a merger model of galaxy evolution does indeed predict some excess in the earlier universe, the strength of the excess, a factor of ~ 10 compared to a non-evolution model, was far too large to be explained on this account alone (Elbaz et al., 1999). This was evidence that IR properties of galaxies have evolved quite actively since about $z \approx 2 - 3$.

At around the same time, the detection of the CIRB (Cosmic Infrared Backgound, Puget et al., 1996) showed that the local luminosity function extrapolated to high redshifts could not account for the observed background and a sub-mm survey with

SCUBA revealed that the number count of sub-mm galaxies at $z > 1$ are a few orders of magnitude greater than expected if assuming a non-evolving model of galaxies during this time (Hughes et al., 1998; Smail et al., 1997). Evidence was also accumulating from different wavelengths (e.g. Elbaz, 2005, and references therein); searching for the Lyman break in different photometric bands it was possible to select very high redshift galaxies (LBG = Lyman Break Galaxy) which showed evidence for strong dust extinction, much more than would be anticipated using the dust extinction from Meurer et al. (1999) based on local starbursts.

By the beginning of this century, it was clear that sub-mm galaxies play an important role in the history of star formation and galaxy evolution, but the very nature of those galaxies was still uncertain (Smail et al., 2002). The distinction between massive, young stars and AGN as the power source of the intense radiation in a sub-mm galaxy is difficult, and both could also be present at the same time, especially if optical counterparts are not present to find AGN specific broad lines in their spectra. From X-ray limits, Smail et al. (2002) estimate that the fraction of AGN within the high-z sub-mm population, detected at 850 μm with SCUBA, is roughly in agreement with local findings of 20-30%, but caution that this needs to be confirmed with more sensitive X-ray observations. Smail et al. (2002) also find that at least half of their sub-mm galaxies lie at $z > 2$ with a median temperature of $T = 37$K using a dust emissivity index $\beta = 1.5$ from the best grey-body fit to the sub-mm continuum. A similar median temperature is found by Dunne et al. (2000) in a local sample of 60 μm selected galaxies, followed up with SCUBA, in SLUGS (SCUBA Local Universe and Galaxy Survey), also discussing the possibility of a much colder dust component at around $T \approx 20$K for a higher value of β.

Assuming no contribution from an AGN, FIR luminosities of $> 10^{12} L_{\odot}$ and SFRs of several hundreds $M_{\odot}\mathrm{yr}^{-1}$ are inferred for SCUBA galaxies (Hughes et al., 1998), making them the most extreme galaxies with respect to dust content and star formation. Models that included a combination of starburst, cirrus and AGN contribution were able to reproduce the observed number counts from both IRAS and SCUBA (Lagache et al., 2003; Rowan-Robinson, 2001); those models predicted a peak in star formation at $z \approx 1$ with a plateau out to $z \sim 2 - 3$. Using a stacking analysis[15], Serjeant et al. (2008) find evidence that sub-mm-selected galaxies at redshifts $1 < z < 1.5$ seem to prefer

[15] A stacking analysis involves the averaging of detected fluxes at pre-determined positions on maps.

denser environments in contrast to the local sub-mm population. Dye et al. (2008) find a median (photometric) redshift of $z = 1.52$ for the galaxies in the SHADES sample, using positions of radio/24 μm counterparts (Ivison et al., 2007) for the creation of a multi-wavelength catalogue.

Using BLAST and a $P(D)$-analysis[16], Devlin et al. (2009) show that 500 μm selected galaxies (with 24 μm counterparts) can account for all of the observed CIRB, effectively resolving the CIRB into individual galaxies; the majority of the CIRB is accounted for by galaxies at $z \geq 1.2$ where the peak of the dust emission is redshifted into the sub-mm wavelength range. From radio and 24 μm counterparts to BLAST sources, Dye et al. (2009) find a median temperature of 26K and a median redshift of ~ 0.6, significantly lower than median redshifts detected by SCUBA surveys at 850 μm. Having only identified 56% of the BLAST sources, they consider the possibility that a vast majority of the unidentified sources would reside at much higher redshifts; they also explain that the much lower median temperature of the BLAST sample might originate from selection effects, themselves caused by the limiting sensitivity of the detector, that lead to detecting galaxies with higher temperatures predominantly at higher redshifts.

Whereas BLAST surveys spanned areas of $\leq 10\text{deg}^2$, the vastly increased survey area of the *Herschel* surveys allows to overcome statistical uncertainties due to small sample sizes. The SDP (Science Demonstration Period) field for the *Herschel*-ATLAS (H-ATLAS) survey already encompassed $\sim 14\text{deg}^2$, detecting $\sim$ 6000 250 μm sources at 5σ (Rigby et al., 2011) and finding optical counterparts for $\sim$37% (Smith et al., 2011). Median redshifts for the sources with optical counterparts is $z \approx 0.25$ with evidence for a significant fraction of unidentified sources to be at $z > 1$; the lower redshift galaxies are estimated to have a median dust temperature of $T \approx 26$K (Smith et al., 2012), again significantly lower than the temperatures estimated for SCUBA galaxies, but consistent with results from BLAST. The luminosities (and hence SFRs) and dust masses are also more moderate, compared to the higher redshift SCUBA galaxies. The picture that emerges for *Herschel* detected galaxies seems to show two distinct populations (e.g. Amblard et al., 2010; Kampen et al., 2012; Roseboom et al., 2012; Rowlands et al., 2011): a low-z population, consisting of moderately star-forming (blue) galaxies and a

[16] A $P(D)$-analysis uses a confusion probability distribution to account for the biases in the source number counts from confusion, survey flux limit and also Eddington bias, see Condon (1974) for the theoretical foundations.

high-z population, much closer in their properties to the "classical" sub-mm galaxies of SCUBA with high FIR luminosities and intense star formation.

In this thesis, we are mainly concerned with the low-z population when matching the H-ATLAS sources of the GAMA 09 field to the NIR detections of VIKING. This thesis is organised as follows. Chapters 2 and 3 introduce the VISTA VIKING and *Herschel*-ATLAS data respectively. The identification process of VIKING objects to *Herschel*-ATLAS 250 μm sources is discussed in detail in chapter 4, as well as the results of our matching algorithm. Chapter 5 presents our photometric redshift algorithm and a discussion of the method together with a comparison of its performance to recent studies. In chapter 6 we construct the 250 μm luminosity function in redshift slices and compare our results to recent studies. A dust attenuation law for a cross-matched ultra-violet sample is compiled and used to calibrate star formation rates deduced from the ultra-violet in chapter 7. Our conclusions are presented in chapter 8.

Chapter 2

VISTA VIKING data

"Sweet to the eye is that which is seen" *Volsunga Saga, chapter 5*

The Visible and Infrared Survey Telescope for Astronomy (VISTA) is a 4m wide-field telescope at the ESO Paranal observatory in Chile (Emerson et al., 2006; Emerson & Sutherland, 2010). The camera (VIRCam, Dalton et al., 2004) has 16 near-infrared detectors and an instantaneous field of view of $0.6\,\mathrm{deg}^2$, and its filter set includes the five broad-band filters Z,Y,J,H,K_s with central (effective) wavelengths $0.88 - 2.15\,\mu$m. The data processing (Lewis et al., 2010) is a collaboration of the Cambridge Astronomy Survey Unit (CASU) and the Wide Field Astronomy Unit (WFAU) at the Royal Observatory in Edinburgh (ROE). The data used in this paper is from the Vista Science Archive (VSA) produced and maintained at ROE, released internally on the 14th April 2011; this is our preliminary object catalogue. The VSA builds on the WFCAM Science Archive (WSA), providing similar access and functionality[1] (e.g. image cut-outs, SQL queries etc.). Sources are extracted after the merging of individual frames and are listed in tables together with astrometric and photometric information.

The next three subsections give a short introduction into the photometric system of VISTA, the data processing pipeline and the photometric calibration, before we will explain how our sample of VIKING objects was selected and how we implemented the star-galaxy separation.

[1] for a detailed description of the functionality and the access options, see Hambly et al. (2008)

Table 2.1: VISTA filter definition and limiting magnitudes. The limiting magnitudes are calculated assuming a seeing of 0.8", airmass of 1.2 and extinction of 0.05 (default) and are aperture magnitudes (Vega) using a 2" diameter.

bandpass	range (μm)	λ_{eff} (μm)	5σ, 60s
Z	0.84-0.93	0.878	21.3
Y	0.97-1.07	1.021	20.6
J	1.16-1.34	1.254	20.2
H	1.49-1.79	1.646	19.3
K_s	1.99-2.31	2.149	18.3

2.0.1 VISTA photometry

The VISTA photometric system, defined by the $Z\,Y\,J\,H\,K_s$ broad-band filters, is a close relative of the UKIRT's WFCAM system (Hewett et al., 2006). The J and H bands have been produced to Mauna Kea Observatories (MKO) specifications (Tokunaga et al., 2002); the Z and Y bands are new, designed for the WFCAM and introduced in Hewett et al. (2006). The motivation for the two new broad-band filters lies in the desire to be able to distinguish between brown dwarfs and high redshift quasars, using colours for which observations at wavelength shortward of 1.2 μm are necessary. The SDSS z band proves unsatisfactory as the filter includes a long red tail, towards wavelength where both brown dwarfs and high-z quasars have steeply increasing flux densities.

The main difference of the VISTA photometric system to the UKIRT's system consists in the use of the K_s filter instead of the K filter, both MKO specifications. The K_s (read K short) filter has been specially designed for 2MASS to cut off at 2.3 μm to reduce the thermal background emission longward of 2.3 μm, see fig. 2.1. Table 2.1 lists the wavelength range, the effective wavelength and the magnitude limits for the VISTA filters.

2.0.2 Instrumental artefacts

Compared to WFCAM, some instrumental artefacts are less consequential for VIRCam. Especially the cross-talk, commonly occuring for WFCAM, seems to be rather

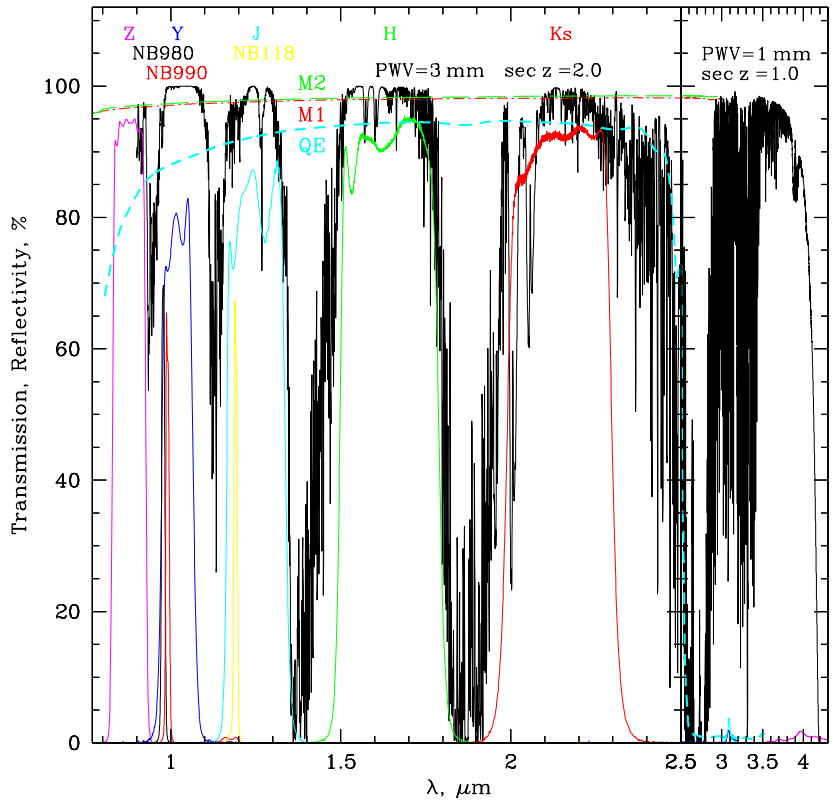

Figure 2.1: — Transmission functions for the VIRCAM filters shown by the coloured, solid lines. the solid black lines show the atmospheric transmission, the cyan dashed line represents the quantum efficiency (QE), the red (M1) and green (M2) dashed lines show the reflectivity of the primary and secondary mirror respectively. Some leaks, although weak, to longer wavelengths are seen in the right hand-panel. In addition to the 5 broad band filters, there are 3 narrow band filters, labeled NB980, NB990 and NB118 at 0.98, 0.99 and 1.18 μm respectively. The figure is from the VIRCAM/VISTA User Manual, their Fig.8

absent for VIRCam. Cross-talk artefacts are invoked by saturated stars, showing up as doughnut shaped or half-moon like features on either side or below and above the star. Persistence, where a saturated image from an earlier exposure imprints on subsequent images, also prevalent in WFCAM images, is minimal for VIRCam.

Local maxima around saturated stars are falsely interpreted as detections by the source extraction software; they are automatically removed by the pipeline in the band merging process. For a single band exposure though, there is no obvious way in how to deal with the extra detections. This is the main reason why we require additional J-band detection for our K_s-selected catalogue, see section 2.1.1.1.

2.0.3 Photometric calibration

Accurate photometry is difficult to achieve in the near-infrared due to large absorption features of mainly water vapour and carbon dioxide in the atmosphere, that are highly variable with time and airmass. As we have seen in section 2.0.1, the filters have already been designed with those features in mind, especially the K_s filter, but some absorption remains and must be dealt with in any photometric calibration plan. The long-term goal is to achieve an accuracy of $\sim 2\%$, similar to the UKIRT's photometric calibration (Hodgkin et al., 2009).

For each exposure and each detector on VIRCam, instrumental magnitudes, an objects apparent brightness as detected by an instrument, are calculated for standard stars within the field as:

$$m_{instr} = -2.5 \log_{10}(f) \tag{2.1}$$

where f the object's flux in counts per second. The instrumental magnitudes are then extinction corrected and compared to the magnitudes of standard stars, an average of 200, in the same field. The difference in the magnitudes provides a measure of the zeropoint, the calibration magnitude, defined as the magnitude yielding a flux of 1 count/sec. The median ZP of the nights zeropoints is then used to calculate an object's magnitude:

$$m = -2.5 \log_{10}(f) + ZP \tag{2.2}$$

The CASU pipeline for photometric calibration uses 2 different sets of standard stars to calculate the ZP: 2MASS stars and Standard Field stars. The 2MASS stars have been used with success for the calibration of WFCAM photometry and shown to be

accurate to 2%, see Hodgkin et al. (2009). A colour term is introduced to correct for the differences in the *JHK* filters between 2MASS and VISTA and the *Z* and *Y* magnitudes are extrapolated from the *J* band and *J*-*H* colours. The 2MASS standard stars are the primary set of standard stars used for the photometric calibration, although the magnitude range is restricted to about 12-14 in all bands because at brighter magnitudes, VISTA's higher resolution leads to saturation, and at fainter magnitudes, the 2MASS limiting magnitude is approached.

Other standard stars (e.g. UKIRT or 2MASS Touchstone Fields) are observed during non-science operation and achieve fainter magnitudes than the 2MASS stars, supplementing the magnitude range.

Photometric errors introduced by the geometric pixel distortion, up to 3.5% in the corners of the field of view as compared to the centre, also have to be corrected for. The astrometric calibration, as outlined in the next section, quantifies the pixel distortion depending on the pixel position.

2.0.4 Astrometric calibration

After the transformation from pixel to celestial coordinates, the astrometric precision is compared to that of the 2MASS point source catalogue (PSC). It is found that the precision is better than about 100mas (milli-arcsec), dominated by 2MASS systematic errors.

The pixel scale varies slightly across the field of view. The distortion is radial in nature, with the strongest distortions in the corners of $\sim 1\%$.

2.1 VIKING

The VISTA Kilo-degree INfrared Galaxy (VIKING, Sutherland et al., in prep.) survey is one of the public, large-scale surveys ongoing with VISTA. The survey has been planned to cover around $1500\,\mathrm{deg}^2$ of extragalactic sky in the five broad-band filters, including one southern stripe (including the H-ATLAS SGP stripes), one equatorial strip in the North galactic cap (including the GAMA 12h and 15h fields) and also the GAMA 9h field. The median image quality is ≈ 0.9 arcsec, and typical 5σ magnitude limits are $J \approx 21.0, K_s \approx 19.2$ on the Vega system or $J \approx 21.9, K_s \approx 21.0$ on the AB system, on average 1.4 magnitudes deeper than UKIDSS-LAS.

2.1.1 VIKING matching sample

The GAMA 9h field (G09) has been observed by VISTA as part of the VIKING survey up to late 2010. It comprises an area of approximately 55 $\deg^2$, contained within RA between 128 and 141 degrees and Dec between -2 and $+3$ degrees (see figure 3.1 with the VIKING area outlined, in section 3.1.1).

The data has been processed by the pipeline in CASU, ingested into the VSA database maintained at (ROE) and released internally on the 14th April 2011.

2.1.1.1 Selection criteria

For our matching object catalogue, we request a 5σ K_s band detection from the source table. The source table has been produced by merging object catalogues from observations in individual filters using nearest neighbours within a pairing radius of 2". We also require a J band detection to exclude the large majority of spurious detections (bright star halos, satellite trails, false detections around a saturated star etc). In addition, we only use sources that are primary detections (best source in overlap regions) with error bits smaller than 256 (only informational error quality conditions), and sources flagged as saturated or noise (in the mergedClass attribute) were excluded. This results in 1,376,606 objects in our VIKING catalogue from the G09 field.

When using SDSS DR7 counterparts to our VIKING objects, we proceed as follows: we require the nearest primary detection (not deblended or a deblend, not saturated, in best field[2]) within 2" from the SDSS DR7 PhotoObj table. Both SDSS and VISTA have positional uncertainties with an rms $< 0.1''$ and a nearest neighbour match is hence considered appropriate.

2.1.1.2 Star-galaxy separation

The likelihood ratio method we employ to match both catalogues (see chapter 4), uses the magnitude distribution of the true counterparts which will depend on the morphological type of the VIKING objects. The VSA uses a shape parameter calculated from the brightness profile of the objects and the point-spread-function (PSF) on each individual detector to classify objects as stars and galaxies. The galaxy sample is

[2] if an object has been detected in more than one field, the detection from the field with the best seeing and the least errors is classified as primary

optimised for completeness, leading to a stellar sample that is optimised for reliability. We have hence started building our stellar sample by using the VSA stellar probability $\geq 95\%$. This puts 464,033 objects firmly into the stellar class.

The remaining objects were then matched to the SDSS database to obtain $g-i$ colours for a classification on the $J-K_s$ vs $g-i$ colour-colour diagram. This follows the procedure used by Baldry et al. (2010) to select a highly complete galaxy sample for the GAMA input catalogue, in conjunction with a SDSS shape parameter. For objects with $r < 19.8$, we employ their prescription for the classification, using a combination of shape and colour parameters. However, most of our objects are much fainter than the $r < 19.8$ cut used by Baldry et al. (2010), and here the SDSS morphological classification is unreliable, as was evident when we used a sub-sample with available spectroscopic redshifts. For objects with an SDSS counterpart fainter than $r > 19.8$, we then classify via the position on the colour-colour diagram. Fig. 2.2 shows the colours of the VIKING sample, the location of our stellar locus and the chosen separation line.

The remainder of VIKING objects that have not been classified above, i.e. objects with VSA stellar probability < 0.95 and without an SDSS counterpart, are separated as follows: objects with $(J-K_s)_{AB} > 0.21$ are classified as galaxies and those with $(J-K_s)_{AB} < -0.34$ as stars. The logic of this can be seen on the colour-colour diagram: even without $g-i$ information, these objects must lie respectively above/below the black separation line in Fig. 2.2. This leaves a stripe at intermediate $J-K_s$ colour where the colour classification remains ambiguous: just over 12,000 objects fall into this category. Here, we look at the VSA shape classification again and relax our earlier cut of 95% to 70%, classifying objects as stars or galaxies with a cut at $pStar = 0.7$. Finally, we move 573 objects classified as stars to the galaxy class as they have confirmed non-stellar redshift of $z > 0.002$ from SDSS spectra: those are mostly confirmed QSOs. This classification results in a sample of 847,530 galaxies and 529,076 stars[3].

[3]In the catalogue, we will include the flag 'sgmode' which indicates how we have arrived at the classification: **1** VSA star with pStar$>$ 0.95, **2** uses Baldry et al. (2010) for objects with $r < 19.8$, with slight modifications, **3** colour-colour selection for objects with $r \geq 19.8$, **4** $(J-K_s)_{(AB)}$ colour selection for objects without SDSS counterpart within $2''$, **5 / 6** VSA pStar$=$ 0.7 cut for objects without SDSS counterparts and ambiguous in $J-K_s$ colour. The sgmode flag is changed by appending a zero to the initial flag if the object was moved from the star class to the galaxy class having a confirmed non-stellar redshift.

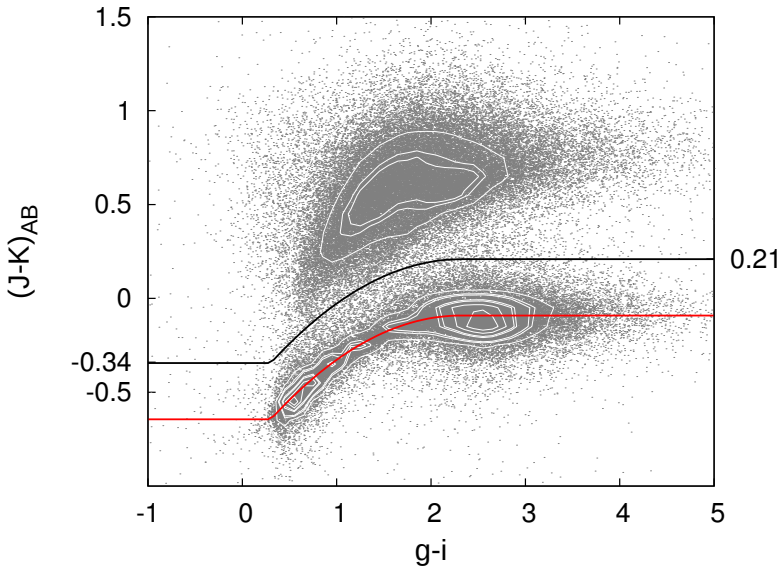

Figure 2.2: — The colour-colour diagram of VIKING objects with SDSS counterparts. The red line shows the stellar locus, obtained from fitting a quadratic equation in the range [0.3,2.3] to the sample with VSA probability of being a star > 0.95. The black line is offset +0.3 mag from the locus, representing the adopted star/galaxy separation cut. Objects without SDSS identifications are classified according to their $J - K_s$ colour only, leaving a stripe of $-0.34 < (J - K_s)_{AB} < 0.21$ where the colour-based classification is ambiguous.

Using this method of classification, QSOs without spectra in SDSS are mainly classified as stars, selected by morphology. This is clearly not ideal, because objects in the star sample are less likely to be identified as reliable counterparts to the SPIRE sources. A more detailed separation, taking QSO properties into account, will be explored in future work (Hoyos et al. in preparation).

Chapter 3

Herschel data

> "Herschel removed the speckled tent-roof from the world and exposed the immeasurable deeps of space, dim-flecked with fleets of colossal suns sailing their billion-leagued remoteness" *Mark Twain*[1]

3.1 The Herschel Space Observatory

The Herschel Space Observatory (HSO, Pilbratt et al., 2010) is a telescope in the submillimetre (sub-mm) range with a 3.5m primary mirror, three science instruments (two photometers and a high resolution spectrometer) and was launched in May 2009. It is now in operational orbit around the L2 point, 1.5 million kilometres from Earth. The science instruments are passively cooled through liquid helium securing about 3.5-4 years of cold observation. The first design dates back to the 1980s when the telescope was named FIRST (Far InfraRed and Submillimetre space Telescope), subsequently called Herschel to mark the 200th anniversary of the birth of the astronomer in 2000. The science motivation behind the conception lay in observing the wavelength range where dust heated by stars emits, a range that is difficult to observe from the ground, see chapter 1.

Two instruments survey in 5 passbands, centred on wavelengths 100 and 160 μm (PACS, Poglitsch et al., 2010) and 250, 350 and 500 μm (SPIRE, Griffin et al., 2010). The beams have full width at half maximum (FWHM) of respectively 8.7, 13.1, 18.1,

[1] Mark Twain, "Tales of Wonder", p.223

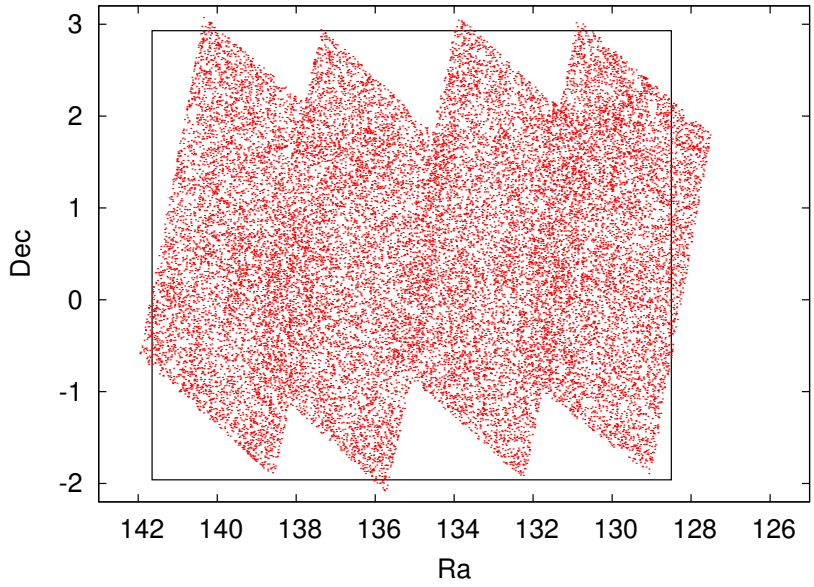

Figure 3.1: — Positions of the H-ATLAS sources in the G09 field from the Phase 1 catalogue. The black solid line represents the outline of the area observed as part of the VIKING survey.

25.2 and 36.9 arcsec, with 5σ point source sensitivities of 132, 126, 32, 36 and 45 mJy in the above 5 passbands.

3.1.1 Herschel-ATLAS survey

The Herschel Astrophysical Terahertz Large Area Survey survey (H-ATLAS, Eales et al., 2010) is a large open-time key project carried out with the HSO. The full survey will cover approximately 550 deg^2 of high galactic latitude sky in six patches. The G09 field is part of the area covered and Fig. 3.1 shows a SPIRE source positions map with the VIKING observed area outlined.

The survey covers the wavelength range $100 - 500\,\mu$m, providing imaging and photometry using the onboard instruments SPIRE and PACS, see section 3.1. The maps and data reduction are discussed in detail in Pascale et al. (2011) and Ibar et al. (2010), and the source catalogue creation, see next section for more detail, is described in Rigby et al. (2011).

The H-ATLAS fields have been selected for low cirrus foreground, and overlap with

a number of other existing and planned surveys to profit from multi-wavelength data. A few important overlapping surveys are the Sloan Digital Sky Survey (SDSS, York et al., 2000) in the optical, the Galaxy And Mass Assembly (GAMA, Driver et al., 2009) survey which includes a spectroscopic redshift survey of mostly SDSS objects (see Baldry et al., 2010, for the target selection) and the VISTA VIKING imaging survey (Sutherland, in preparation) in the near-infrared.

The data was obtained in parallel mode with both PACS and SPIRE scanning the sky simultaneously with an angular velocity of ~ 60 arcsec/s.

3.1.1.1 H-ATLAS source catalogue creation

The Phase 1 catalogue (Dunne et al., in preparation) from which we draw our H-ATLAS sample is obtained by extracting sources from a map generated using a naive map making technique. Here, naive corresponds to a noise matrix that is caused by white noise only, i.e. the noise in the map is uncorrelated with respect to time as well as being uncorrelated between detectors. Future releases will use the MADmap algorithm assuming uncorrelated noise between detectors only so that the noise within detectors can be correlated with time.

In the three SPIRE bands, sources are identified using the Multi-band Algorithm for source eXtraction (MADX, Maddox et al. in preparation). The noise levels in the PACS bands proved higher than expected leading to the decision to use just the SPIRE bands for a simultaneous 3-band source extraction. After background subtraction and PSF filtering, sources with a S/N > 2.5 are identified on the 250 μm map and a Gaussian is fit to the peak to estimate the position at sub-pixel level and to obtain the point-source flux. The 250 μm maps were chosen because they suffer less from source confusion. The position thus obtained is then used on the 350 and 500 μm maps, after pixel interpolation to allow for the different pixel sizes, to measure the 350 and 500 μm fluxes of an object, identified on the 250 μm map. This results in a catalogue consisting of 26,369 objects in G09 with S/N $> 5\sigma$ in at least one of the three SPIRE bands.

The positions of the sources identified on the 250 μm SPIRE map are also employed on the 100 and 160 μm PACS maps. Because of the higher than expected noise levels, fluxes are estimated using apertures of 10" and 15" respectively. The flux errors are calculated by placing apertures on random positions on the PACS maps. Nevertheless,

because of the much higher uncertainty in the PACS fluxes, PACS data was not included in the Phase 1 catalogue distributed to the H-ATLAS team and used here. For a detailed description of the source catalogue creation see Rigby et al. (2011).

3.1.1.2 H-ATLAS matching sample

For the matching process we use a 250 μm selected sub-sample from the Phase 1 G09 catalogue, requiring S/N ≥ 5 in 250 μm. We find that 22,000 of these SPIRE positions are within the region observed by VIKING up to late 2010 (an area of approximately 55 deg^2, contained within RA between 128 and 141 degrees and Dec between -2 and $+3$ degrees, see fig. 3.1 and section 2.1.1), and these comprise our catalogue used in the matching hereafter.

The Phase 1 catalogue supplies optical counterparts from SDSS (Hoyos et al., in preparation) using a similar LR technique to that presented here, and discussed as well in Smith et al. (2011). The optical counterparts have been used to obtain photometric redshifts which are also supplied with the catalogue.

Chapter 4

Counterparts to sub-mm sources

> "The brightest flashes in the world of thought are incomplete until they have proven to have their counterparts in the world of fact." *John Tyndall*[1]

The difficulty in combining different wavelength observations lies in deciding which objects are truly associated and which objects are unrelated background objects. Matching sub-mm sources to objects observed in much shorter wavelengths is particularly difficult, because the large sub-mm beam sizes, and hence the comparatively lower angular resolution, and high confusion noise increase the positional uncertainties which in turn force us to increase the radius we employ searching for plausible counterparts. The increased search radius, together with the high surface density of objects from optical/near-infrared surveys, is responsible for the ineffectiveness of a simple closest neighbour method.

A method often employed consists of matching sub-mm sources to radio or mid-infrared sources first (Biggs et al., 2011; Dye et al., 2009; Ivison et al., 2007), before utilising the multi-wavelength data that is already available for the radio/mid-infrared counterparts, or making use of the more accurate positions to improve on the matching technique. Dye et al. (2009) are matching their BLAST sample, with a significance $> 5\sigma$ in at least one of the 250, 350 and 500 μm bands to 1.4 GHz radio and 24 μm Spitzer catalogues. The positions thus obtained, using averages if they found a counterpart in

[1] John Tyndall, 1820-1893, physicist

the radio as well as in the mid-infrared, are then applied to search for counterparts in photometric redshift catalogues within a 3 arcsec radius.

This is advantageous because of the radio/far-infrared correlation (Hainline et al., 2009; Ivison et al., 2010; Jarvis et al., 2010; Michalowski et al., 2010), the lower surface density and the high positional accuracy of radio sources (Dunlop et al., 2010; Dye et al., 2009; Ivison et al., 2007). Traditionally, the matching of sub-mm sources to radio and mid- or far-infrared catalogues has relied on an approach using the P-value of a possible identification. The P-value of an object at distance r from the sub-mm source embodies the probability that an object could have been at distance r by chance. We will explain this approach in detail in section 4.1.

Unfortunately, identifying optical/near-infrared counterparts via radio counterparts is not yet practical for H-ATLAS, see section 3.1.1, since current radio telescopes cannot deliver the required area/depth combination; Hardcastle et al. (2010) found 187 radio-loud sources within the H-ATLAS Science Demonstration Phase (SDP) field, less than 3% of all available sources. This may improve though in future with SKA (Square Kilometre Array) and its precursors LOFAR (LOw Frequency ARray), ASKAP (Australian Square Kilometre Array Pathfinder, Johnston et al., 2008) and MeerKAT (Schilizzi et al., 2008).

Roseboom et al. (2010) have used Spitzer source positions for the identification (and source extraction) process of the Herschel Multi-Tiered Extragalactic Survey (HerMES) sources, taking advantage of the small positional uncertainties at $3.6\mu m$ and $24\mu m$. Mid-infrared data is available for only small patches within the H-ATLAS observed fields, see the work of Bond et al. (2012), using WISE (Wide-field Infrared Survey Explorer) data and Kim et al. (2012), using Spitzer IRAC legacy data.

An alternative approach is to match the sub-mm sources directly to an optical or near-infrared catalogue. This approach has been used in conjunction with the already mentioned P-value. After choosing an appropriate cut-off value for the P-value, usually 0.05, potential matches are declared a secure identification if they achieve a P-value equal or smaller. A secure match has hence a probability of 5% or less of just being a random background object. We will expand on this method in section 4.1 where we also explain the limitations of this approach.

Recently, a different approach has been employed for finding multi-wavelength counterparts to sub-mm sources, based on Bayes statistics. It uses information on the po-

sitional uncertainty probability distribution of the sub-mm sources and the magnitude distribution of the optical/near-infrared objects. It involves the ratio of infinitesimal probabilities and is called the likelihood ratio method, LR for short. Section 4.2 explains this method in detail as well as its advantages over the P-value method. We will then use the LR technique in the next chapter to find VIKING identifications to the H-ATLAS sources.

4.1 P-value method

The basic principle of this method is straight forward: a possible match at distance r from the sub-mm sources with magnitude m is evaluated and ranked against other matches by estimating the probability P that there is at least one object at distance $\leq r$ and with magnitude $\leq m$ by chance, the so-called P-value. This is inherently a Poisson process where the random variable is the number of objects found at randomly chosen positions with an average rate μ of objects per unit surface. This approach has first been systematically introduced by Downes et al. (1986) who searched for optical counterparts (from the Palomar Observatory Sky survey and UK Schmidt plates) to radio sources at 2.7GHz with the VLA. If μ the expected number of objects within a radius r of the sub-mm position, with

$$\mu = \pi r^2 N(\geq m) \tag{4.1}$$

then

$$P_0 = \exp(-\mu) \tag{4.2}$$

the Poisson probability that no object is found within the radius r and hence

$$P = 1 - P_0 = 1 - \exp(-\mu) \tag{4.3}$$

the probability that at least one object is within the radius r, the P-value. For $\mu \ll 1$ we get $P \approx \mu$. It is usual to set an a priori limit for the P-value below which an identification is deemed secure. Most research teams require either $P \geq 0.05$ (2σ significance level) or $P \geq 0.01$ (3σ significance level).

Two issues arise with this approach: firstly, a correction has to be incorporated because we effectively consider objects in different magnitude classes; secondly, we

do have a statistical measure of a chance identification, but can we then deduce the probability that this is really the true identification? Both issues are related as will become clear.

Downes et al. (1986) consider an object with a P-value of P^*. This is the probability that the object is found at this radial distance r and with this magnitude m. There are most likely to be other combinations of r and m with $P \leq P^*$ and objects with those combinations (which are too faint to be seen on the plate) would be preferred candidates; summing up the expected number of those events, Downes et al. (1986) obtain a correction term and the new P-value is:

$$P^* = P^*(1 + \ln(P_c/P^*)) \tag{4.4}$$

where P_c the so-called critical Poisson probability with $P_c = \pi r_s^2 N_t$ and r_s the search radius and N_t the density at the plate limit, assuming that $P^* \ll 1$. This addresses the first issue by considering all magnitude classes (and radial distances). The second issue remains unresolved, because $1 - P^*$ is still not the probability that the object is indeed the correct identification: we are again left with the probability of a chance identification only.

The correction that Downes et al. (1986) have calculated is actually negligible in their case, but they acknowledge that it will be important for future deeper surveys. Indeed, the surface density of current CCD imaged surveys can be much higher though than the one from the Palomar or UK Schmidt plates (e.g. in the HDF the surface density reaches 0.1 arcsec^{-2}) and the correction becomes important. Some authors apply this analytical correction (Biggs et al., 2011; Chapin et al., 2009; Dannerbauer et al., 2010; Dunlop et al., 1989; Ivison et al., 2002, 2007; Pope et al., 2006), others find their own solutions to compensate for all possible combinations of r and m, some examples below.

Lilly et al. (1999) attempt to identify optical, mid-infrared and radio counterparts to 12 sub-mm sources from the UK-Canadian submillimeter survey. They are calculating a correction term to the P-value by using a Monte-Carlo method to estimate the distribution of the P-value with random positions on their matching catalogue. They find correction factors, as a function of the search radius, the magnitude and the P-value, that are as large as 6.5 for $P \leq 0.01$ and ~ 3.5 at $P \sim 0.5$. As Clements et al. (2004) state, the advantage of utilising the data itself to correct the raw Poisson probability

is, that it can take the clustering and varying magnitude limit into account. Clements et al. (2004) also use a Monte-Carlo method to estimate the distribution of the P-values in their data. They then use this distribution to calculate the probability of a certain P-value occurring. This technique is explained in detail in Dye et al. (2009) who use the normalised distribution $D(S)$ of the value $S = r_{sep}^2 n(< f)$ of objects as separation r_{sep} and with flux f at random positions to obtain the probability $P(< S)$. This is then the probability of a potential counterpart to a sub-mm position to have a value of S by chance. We will be using a similar approach later to estimate the probability of a mis-identification when using the LR method in our matching of VIKING objects to H-ATLAS sources, see section 4.3.1.

The correction factor, either analytical or empirical, will always depend on the choice of the search radius. A larger search radius will result in higher corrected P-values (or equivalent, it will increase the expected number of wrong identifications $= N \times P$) and an increased risk in wrongly identifying a brighter galaxy; with a smaller radius we can miss true identifications. If we assume Gaussian errors, and most authors do, we can use the standard deviation in the positional errors and determine the search radius cutoff by deciding what percentage of true counterparts we are willing to miss., e.g. at a search radius of $r = 2.5\sigma$ we should only miss $\sim 1\%$ of the true counterparts. We can calculate the expected number of wrong identification by summing up the P-values of the identifications. If the standard deviation of the positional error is not known, it can be estimated from the data by computing the angular distance distribution of objects in the matching catalogue from the sub-mm position and fitting a Rayleigh distribution $f(r) = \frac{r}{\sigma^2} \exp(-\frac{r^2}{2\sigma^2})$. [2] Ivison et al. (2007), matching SCUBA $850\mu m$ sources to radio and mid-infrared objects, have used this method to calculate the 1σ positional errors by fitting Gaussian distributions to the individual RA and Dec offsets. Both best-fits results in $\sigma \simeq 3''$ which leads to their adopted search radius of $8'' \sim 2.5\sigma$ that should include $\sim 97\%$ of all counterparts.

A similar procedure was also used by Smith et al. (2011) when investigating the positional error distribution of the H-ATLAS sources in the SDP field. Their model for the fit to the RA and Dec offset distributions includes the effect of clustering. The clustering signal is deduced from fitting the histogram of the radial offsets θ of all SDSS

[2] If positional errors in RA and Dec are normally distributed, then the positional error in the radial separation r is a Rayleigh distribution.

objects to their neighbours within 50 arcsec to the angular correlation function using a simple power law of the form $\omega(\theta) = A\theta^{-\delta}$. The 1σ positional error is then estimated by fitting a sum of Gaussians, one of them using the radial offset and convolved with the correlation function. This leads to a 1σ positional error of $\sigma_{pos} = 2.4''$, using the mean of the deviations in RA and Dec. They subsequently use a 10 arcsec search radius to match r band selected SDSS objects to the SPIRE sub-mm sources, in effect using $> 4\sigma_{pos}$ which should include $> 99.998\%$ of all counterparts. We adopt this search radius for the matching of the VIKING objects to the SPIRE sources, as we are adding our VIKING counterparts to the already existing H-ATLAS Phase I catalogue and hence the search radius is fixed. See section 4.2.1 for more detail on the H-ATLAS positional error distribution.

We subsequently estimate the percentage of missed identifications in a similar way as Dye et al. (2009) and find it to be not more than $\sim 5\%$. As explained in section 4.2.1 though, there is some evidence for a departure from Gaussian errors in RA and Dec for the SPIRE instrument.

Dye et al. (2009) have calculated the optimal search radius cutoff. Subsequently they have not used the resulting value of the standard deviation $\sigma \approx 8''$ to calculate the cutoff radius though, instead they have used the radius at which the number of expected false identifications equals the number of expected excluded counterparts. This resulted in a search radius of $r = 21'' = 2.6\sigma$ at which they expect 3.2% of false identifications and the same percentage of missed counterparts, calculated using the Rayleigh cumulative distribution function $1 - \exp(-\frac{r^2}{2\sigma^2})$.

Borys et al. (2004) have used yet another way of finding (or rather justifying) the optimal search radius. For a radius θ they determine the number k of optical objects within that radius around SCUBA sub-mm sources. Then they are calculating the Poisson probability P_{k+} that k sub-mm objects or more have at least one counterpart inside the radius by chance, using the surface density up to the magnitude limit. The radius at which this probability is minimised should be the optimal search radius. As the authors state, this approach is purely theoretical and does not take clustering or lensing into account.

So what are the typical identification rates of sub-mm sources when using the Poisson statistic? They are hard to compare from the literature because they depend

strongly on the wavelengths involved, the depths of the catalogues, the surface densities, the S/N cuts and the P-value cutoff for a secure identification. Recent radio identifications to sub-mm sources achieved a rate of $\sim 60-75\%$ (Biggs et al., 2011; Chapin et al., 2009; Dye et al., 2009). The identification rate to mid-infrared catalogues can be equally high (Dye et al., 2009; Pope et al., 2006). Matching SCUBA, AzTEC and MAMBO sub-mm sources to PACS far-infrared objects, Dannerbauer et al. (2010) achieve an identification rate of 39%.

Matching to large, high surface density optical or near-infrared catalogues has not been attempted using the P-statistic. A substantial fraction of sub-mm sources will have more than one object within the necessary large search radii and the P-values cannot be trusted to calculate which of the possible matches is more likely to be the true counterpart. A fainter but closer object could have a lower P-value, when in fact the brighter galaxy at greater distance is the true counterpart. As a consequence of high surface densities, the P-values become a lesser tool in deciding whether an object is a true counterpart or just an unrelated background object. The LR method, discussed in the next section, will address this issue.

4.2 Likelihood ratio method

As we have seen in the last section, an object that is very near the source will have a preferable P-value. In reality, considering the matching of optical or near-infrared objects to sub-mm sources, the positional uncertainties in the surveys involved make this occurrence rather unlikely. Preferably, we would like to use a method that can incorporate the positional uncertainty distribution, i.e. the distribution of the offsets of the true counterparts to the sub-mm positions.

We would also like to include the magnitude limit of the matching survey, the fraction of counterparts we are likely to find, considering that some true counterparts might just be too faint to be detected.

Finally, we would like to introduce a way of comparing the probabilities of all possible counterparts to a source. If the surface densities involved are low, we will rarely encounter the case where there is more than one possible counterpart within the search radius. In this case, the P-value which presents the probability of this object (with magnitude m and at distance r to the source) existing by mere chance, is a valuable tool

in selecting a counterpart. If we are dealing with more than one possible counterpart, we encounter the problem to compare P-values. A more distant, brighter object can have the same P-value as a close faint object. More than one possible counterpart can have P-values below the P-value cut-off. For the optical and near-infrared surveys considered here, with surface densities that make this case increasingly likely, we need hence a method that can help us deciding between different possible counterparts.

The likelihood method (LR) has the potential to address all issues mentioned above, if the positional uncertainties are known or can be estimated. It uses the ratio of two probabilities: the probability that a true counterpart is observed at a distance r from the source and with magnitude m and the probability that an unrelated background object is observed with the same properties:

$$L = \frac{P(r, m, id)}{P(r, m, chance)} \tag{4.5}$$

The probability $R = P(id|r, m)$ that an object at distance r and with magnitude m is a true counterpart, also called the reliability, is then:

$$R = P(id|r, m) = \frac{L}{L + 1} \tag{4.6}$$

using Bayes' theorem and the theorem of total probability.

This approach has been used by de Ruiter et al. (1977) to match optical objects to radio sources. The magnitude information is not used in the analysis and the reliabilities are based on the distance alone. They define the dimensionless offset r as

$$r = \left[\frac{\triangle\alpha^2}{\sigma^2_{\alpha_{rad}}} + \frac{\triangle\delta^2}{\sigma^2_{\delta_{rad}}} \right] \tag{4.7}$$

The Poisson probability that the first chance object is found within a distance r is then $p(r|c) = 1 - \exp(-\lambda r^2)$ with $\lambda = \pi\sigma_\alpha\sigma_\delta\rho(b)$ and $\rho(b)$ the surface density of objects at the galactic latitude b. This is the P-value as described above. The probability $dp(r|c)$ for the first object to be found between r and $r + dr$ is hence

$$dp(r|c) = 2\lambda r \exp(-\lambda r^2)dr \tag{4.8}$$

de Ruiter et al. (1977) are assuming that the positional error distribution is Gaussian. The radial error follows hence a Rayleigh distribution and the probability $dp(r|id)$ for a true counterpart to be observed between distance r and $r + dr$ is then

$$dp(r|id) = r \exp(-r^2/2)dr \tag{4.9}$$

and

$$L = \frac{dp(r|id)}{dp(r|c)} = \frac{1}{2\lambda}\exp(\frac{r^2}{2}(2\lambda - 1)) \tag{4.10}$$

The reliability is then, with Bayes theorem and the theorem of total probabilities:

$$p(id|r) = \frac{dp(r|id)p(id)}{dp(r)} = \frac{\frac{dp(r|id)}{dp(r|c)}\frac{p(id)}{p(c)}}{\frac{dp(r|id)}{dp(r|c)}\frac{p(id)}{p(c)} + 1} = \frac{\frac{p(id)}{p(c)}L}{\frac{p(id)}{p(c)}L + 1} \tag{4.11}$$

de Ruiter et al. (1977) introduce $p(id) = \theta$, the fraction of radio sources with an optical counterpart and argue that it follows that $p(c) = 1 - \theta$ if we assume that if the true counterpart exists, it is always the nearest to the source. This assumption is necessary because they have used it in deriving $dp(r|c)$. The reliability R_i for an individual identification is hence:

$$R_i = p(id|r) = \frac{\frac{\theta}{1-\theta}L_i}{\frac{\theta}{1-\theta}L_i + 1} \tag{4.12}$$

de Ruiter et al. (1977) do not use the above reliability to access the individual identifications; they rather employ a minimum likelihood value L_{min} above which a counterpart is deemed to be a secure identification. The reliability of the whole set of secure identifications is assessed by fixing L_{min}, which would be equivalent of a minimum reliability if θ is known. The authors chose a cut-off value of $L_{min} = 1.8$ which is a trade-off between the completeness and the reliabilities; this leads to $\theta \sim 0.25$, i.e. the probability of a radio identification is 25%. This seems to be acceptable to the authors in view of it being consistent with other research so far. The reliability of the sample is then calculated as

$$R = 1 - (\frac{\sum_{L>L_{min}} p(c|r)}{N_{id}}) \tag{4.13}$$

with N_{id} the number of radio sources with counterparts with $L > 1.8$. This results in an overall reliability of $R = 0.84$ and $R = 0.94$ for two different sets of plates.

The completeness of the sample can be calculated by summing up over the non-identified sources:

$$C = 1 - \Big(\sum_{L<L_{min}} p(id|r)/N_e\Big) \tag{4.14}$$

where $N_e = \sum p(id|r)$ the number of expected identifications. They achieve a high completeness of $C = 0.95$ and $C = 0.98$ for the two sets of plates.

Benn (1983) try to establish a cross-matching algorithm with particular reference to optical identification to radio sources. They are using the same likelihood ratio method,

but determine the probabilities slightly differently. The probability that an identification exists[3], the θ in de Ruiter et al. (1977), here denominated Q, is incorporated into the probability $dp(r|id)$ from the start, so that $dp(r|id) = Qr \exp -r^2/2dr$, using the same dimensionless offset r, see equation 4.7. The probability of a chance object between r and $r + dr$ is simplified: $dp(r|c) = 2\pi n' r dr$ where $n' = n\sigma_{alpha}\sigma_{delta}$ and n the background surface density. This eliminates the assumption of the true counterpart being the nearest to the source when using Poisson statistics, as de Ruiter et al. (1977) did, see eq. 4.8. The reliability of an object is then equivalent to equation 4.6. From $\sum R = QN$ where N the number of radio source, one can estimate Q using iterations.

Benn (1983) argue that the reliabilities can be further constraint by including the magnitude information of the possible counterparts. The magnitude distribution of the background objects, here denoted by $b(m)$ is in general steeper than the distribution of the true counterparts, denoted $i(m)$. The likelihood ratio value of an object can therefore include the magnitude of the optical object by multiplying with the factor $i(m)/b(m)$.

Prestage & Peacock (1983) are considering similar probabilities, without magnitude information, in their LR analysis of optical counterparts to radio sources, but use inequalities to constrain the reliability to eliminate the need to estimate $P(id)$, the probability that a true counterpart exists down to the survey limit, denominated Q in Benn (1983), but dependent on the radio source here. The probability that the true counterpart to an individual source does not appear on the optical plate is:

$$1 - P(id) = \Pi_i[1 - P_i(id|r)] \qquad \text{hence} \qquad P(id) = 1 - \Pi_i[1 - P_i(id|r)] \tag{4.15}$$

where i runs over all possible counterparts of a source. From this follows that $P(id) \geq P_i(id|r)$. With the theorem of total probabilities it follows:

$$\frac{P(id|r)}{1 - P(id|r)} = \frac{P(id)}{P(c)} \frac{P(r|id)}{P(c|r)} = P(id) \times L \tag{4.16}$$

if setting $P(c) = 1$, the probability of a chance object appearing on the plate. From this and $P(id) \geq P_i(id|r)$, it can easily be shown that $P(id|r) \geq 1 - 1/L$, the lower

[3] used here with a slightly different meaning than in de Ruiter et al. (1977): θ is the probability that the first object encountered around a radio source is the true identification, Q is the fraction of sources that have optical counterparts up to the survey limit.

limit on the reliability. From $P(id) \leq 1$ it can also be shown that $P(id|r) \leq L/(1+L)$, hence:

$$1 - \frac{1}{L} \leq P(id|r) \leq \frac{L}{1+L} \tag{4.17}$$

The value of $P(id)$ should have been considered when calculating the likelihood ratio though, as in Benn (1983), and in effect, they have just avoided using a prior. Conservatively they use the lower limit of equation 4.17 when quoting a value for the reliability. They consider optical objects as a secure identification if $L > 10$ (resulting in an identification rate of 41%), a cut-off value which is arbritrary and which they do not discuss.

Sutherland & Saunders (1992) extended the likelihood ratio by incorporating information about other potential counterparts to one source in the calculation of the reliability, and also including additional information (denoted by c) which can be, for example, colour information or star/galaxy classification This is especially useful in a situation where the matching catalogue has a high surface density so that there is a high probability of there being more than one possible counterpart. The reliability R_j that the jth candidate for one source is the true counterpart is then:

$$R_j = P(id|r, m, c)_j = \frac{L_j}{\sum_i L_i + (1 - Q)} \tag{4.18}$$

where i runs over all candidates for the source and Q is the probability of finding a genuine counterpart above the limiting magnitude in the survey, as in Benn (1983). In contrast to equation (4.6), this includes information about other possible counterparts to the source. To clarify this, equation 4.6 is the reliability *without* information about other candidates for the same source (e.g. picking one candidate at random from a concatenated list of all candidates for a large number of sub-mm sources), while equation 4.18 is the reliability given the set of all candidate matches for one given source.

Sutherland & Saunders (1992) define $q(m, c)$, the probability distribution of the true counterparts with magnitude m and additional property c and $f(r)$, the probability distribution of the positional errors where r the separation from the source positions, as:

$$2\pi \int_0^{+\infty} f(r) r dr = 1 \quad \text{and} \quad \int_{-\infty}^{M_{lim}} q(m, c) dm dc = Q \tag{4.19}$$

where M_{lim} the limiting magnitude in the matching catalogue. It is usually assumed that the positional errors are independent of the magnitude and other additional information, so that $P(m, r, c, id) = P(m, c, id)P(r, id)$. If $n(m, c)$ is the surface density of unrelated background objects per unit magnitude, the likelihood ratio is then:

$$L = \frac{P(m, c, r, id)}{P(m, c, r, chance)} = \frac{q(m, c)f(r)}{n(m, c)} \tag{4.20}$$

In practice, the involved probabilities have to be estimated from the data by fitting simple models.

We have used this approach in our matching of the H-ATLAS sub-mm sources to the VISTA VIKING object catalogue. Therefore, we have to estimate the probability distribution $f(r)$ of the positional errors and the magnitude distributions $q(m)$ of the true counterparts and $n(m)$ of the background objects. The latter is derived by simply using the surface density of the VIKING objects. The next two sections will deal with the positional errors of the H-ATLAS sources and the magnitude distribution of the true matches. After this we will estimate the fraction of counterpart that we expect to mis-identify.

4.2.1 Positional error distribution

We adopt the simple model that the H-ATLAS source positional errors are Gaussian with equal rms σ_{pos} in each of RA and Dec; then the normalisation condition above requires

$$f(x, y) = f(r) = \frac{1}{2\pi\sigma_{pos}^2} \exp(-\frac{r^2}{2\sigma_{pos}^2}) \ . \tag{4.21}$$

where $r = \sqrt{x^2 + y^2}$ is the radial position difference , and we note $f(r)$ has units of (solid angle)$^{-1}$. Smith et al. (2011) have estimated the positional errors of $> 5\sigma$ SPIRE sources, using histograms in RA and Dec of the total number of SDSS sources within a 50 arcsec box around the SPIRE 250 μm centres and taken the clustering of the SDSS objects into account. They fit the sum of the Gaussian positional errors and the clustering signal, convolved with the Gaussian errors, to the resulting histograms. For a more detailed description of the derivation of the positional uncertainties, see section 2.1 of their paper. To be able to use their results, we measure the correlation of our VIKING objects to the SDSS objects, constructing the corresponding RA and Dec histograms, with VIKING objects within a box around the SDSS positions. The 1σ VIKING

position errors are $< 0.2''$ and therefore negligible compared to the SPIRE errors. We hence adopt the weighted mean 1σ positional uncertainty of $\sigma_{pos} = 2.40'' \pm 0.09$ quoted in Smith et al. (2011) and assume the errors to be symmetric in RA and Dec.

In theory, the positional uncertainty should depend on the S/N values and the full width at half maximum (FWHM) of the observations. Ivison et al. (2007) derive[4] the positional uncertainty as $\sigma = 0.6 \times \frac{\mathrm{FWHM}}{\mathrm{S/N}}$. Following Smith et al. (2011), we adjust the formula to match our mean positional error by inserting a scaling factor of 1.09, so that:

$$\sigma_{pos} = 0.655 \times \frac{\mathrm{FWHM}}{\mathrm{S/N}} \tag{4.22}$$

with the SPIRE mean FWHM= $18.1''$. For each SPIRE source, the positional uncertainty from equation 4.22 is then used in our LR calculation. We also set a minimum of $\sigma_{pos} = 1''$ for sources with high S/N, as there are limitations to the minimum positional accuracy from SPIRE and SDSS maps, as discussed in Smith et al. (2011). We adopt a conservative search radius of 10 arcsec which would include 99.996% of the real counterparts assuming Gaussian errors; in practice, there is evidence for slightly non-Gaussian wings (see Hoyos et al., in preparation), but this radius still includes almost all genuine matches.

4.2.2 Estimation of $q(m)$ and Q

We estimate the probability distribution $q(m, c)$ of the true counterparts by using the background subtracted sample of candidate matches, as outlined in Ciliegi et al. (2003). For each class (c =galaxies and c =stars), we estimate $q(m)$ from the data as follows:

- create a magnitude distribution $total(m)$ of all objects within a search radius of 10 arcsec around the SPIRE sources
- background subtract $total(m)$ to obtain the so-called $real(m)$ distribution
- normalise $real(m)$ so that $q(m) = \frac{real(m)}{\sum_{m_i} real(m_i)} \times Q_0$

where we sum over bins of magnitude. The background is determined from the number density $n(m)$ measured from the whole catalogue, scaled to a 10 arcsec circle. The

[4] a derivation of this formula can be found in the appendix of Ivison et al. (2007)

normalisation factor Q_0 is an estimate of the probability of finding a counterpart in the VIKING survey down to the 5σ survey limit, Q in equation (4.19)[5].

A reasonably accurate value of Q_0 is important, since this enters the reliability formula above, equation 4.18. Simply estimating Q_0 via a stacking analysis (summing $real(m)$ and dividing by the number of SPIRE sources) is not ideal, since source clustering and/or genuine multiple counterparts will tend to overestimate Q_0 by multi-counting, and therefore reliability estimates will be biased high.

To avoid this multi-counting problem, we decide to estimate $1 - Q_0$, the fraction of SPIRE sources without a VIKING-detected counterpart, hereafter called blanks: these will be mostly real sources fainter than the VIKING limit, but also including counterparts outside the search radius and spurious SPIRE detections (if any). We start by counting the observed blanks to a given search radius r; we then need to correct for those sources that have VIKING candidate matches, where the match(es) are in fact unrelated to the SPIRE source. The number of true blanks is the number of observed blanks, plus the number of true blanks that have been matched with a random VIKING object. To estimate the latter, we create a catalogue of N (=number of SPIRE sources) random positions and cross-match with the VIKING catalogue. Hence, defining $\bar{R}$ as the number of blanks at random positions, R the number of random positions with a VIKING source within 10" and $\bar{S}$ the number of observed SPIRE blanks, we can calculate the number $\bar{S}_t$ of true SPIRE blanks as follows:

$$\bar{S}_t = \bar{S} + \left[\bar{S}_t \times \frac{R}{N}\right] \Leftrightarrow \bar{S}_t = \frac{\bar{S}}{1 - R/N} = \frac{\bar{S}}{\bar{R}/N} \tag{4.23}$$

Dividing by N provides us then with the fraction of the SPIRE sources that are true blanks, $\bar{S}_t/N = \bar{S}/\bar{R}$, which is our estimate for $1 - Q_0$. Thus, we only need to divide the number of SPIRE blanks by the number of random blanks, for a given search radius.

For our default search radius of 10 arcsec, we obtain $1 - Q_0 = 0.25$, or $Q_0 = 0.75$. We could use this value in our subsequent LR analysis; however, it depends on the value of the search radius and the Q, as defined in equation (4.19), of the VIKING catalogue is independent of the search radius. We would like to obtain an estimate Q_0 of Q that is independent of the radius and so repeat the above procedure for radii in

[5] Ciliegi et al. (2003) have introduced the constant Q_0 as the value of Q as estimated from the data.

the range 1-15 arcsec. The values we obtain for the fraction of true blanks are shown in Fig. 4.1 as black points.

We then model the dependence of the true blanks on the search radius as follows: a SPIRE blank at radius r is a source whose counterpart is either fainter than the VIKING limit, or lies outside the search radius, or both. The former probability is $1 - Q_0$, this is the first term in equation (4.24). The probability of the counterpart to reside outside the search radius can be calculated from the positional error distribution $f(r)$, leading to our second term in equation (4.24). The third term follows if we assume that both possibilities are independent of each other, and using the standard probability result $P(A \text{ or } B) = P(A) + P(B) - P(A \text{ and } B)$. Our model for the dependence of the true blanks on the search radius r is then:

$$\begin{aligned} &(1 - Q_0) + (1 - F(r)) - (1 - Q_0)(1 - F(r)) = 1 - Q_0 F(r) \\ &\text{where} \quad F(r) = \int_0^r P(r')dr' = 1 - e^{-\frac{r^2}{2\sigma^2}} \\ &\text{and} \quad P(r) = 2\pi r f(r) \end{aligned} \tag{4.24}$$

Fitting this model to the data, we obtain $Q_0 = 0.73 \pm 0.03$ as our best-fitting value. Fig. 4.1 shows the best fit model as the black line and the black filled circles as our data points ($\bar{S}/\bar{R}$ for each radius).

The model underestimates the number of SPIRE blanks in the data in the range $4'' \leq r \leq 8''$ and overestimates the data for $r > 10''$. This might show some evidence for clustering of the VIKING objects which we have not explicitly considered, but which is accounted for in the value of the mean positional uncertainty $\sigma_{pos} = 2.4''$ by Smith et al. (2011); they convolve their model with the clustering signal of the SDSS sources to obtain the value we adopt here. It might also demonstrate that the Gaussian approximation for the SPIRE positional errors, our equation (4.21), is not entirely accurate. This is also evident when investigating histograms of distances of VIKING and SDSS objects to SPIRE sources. We see slightly higher numbers of objects at distances of around 10 arcsec than expected if we assume a Gaussian error distribution. This assumption is examined and will be discussed in Hoyos et al. (in preparation).

Our fitted value of $Q_0 = 0.73$ is consistent with the value of $Q_0 = 0.75$ from the datapoint at our search radius of 10 arcsec, and is more conservative. We hence adopt the fitted value $Q_0 = 0.73$ for our subsequent LR analysis.

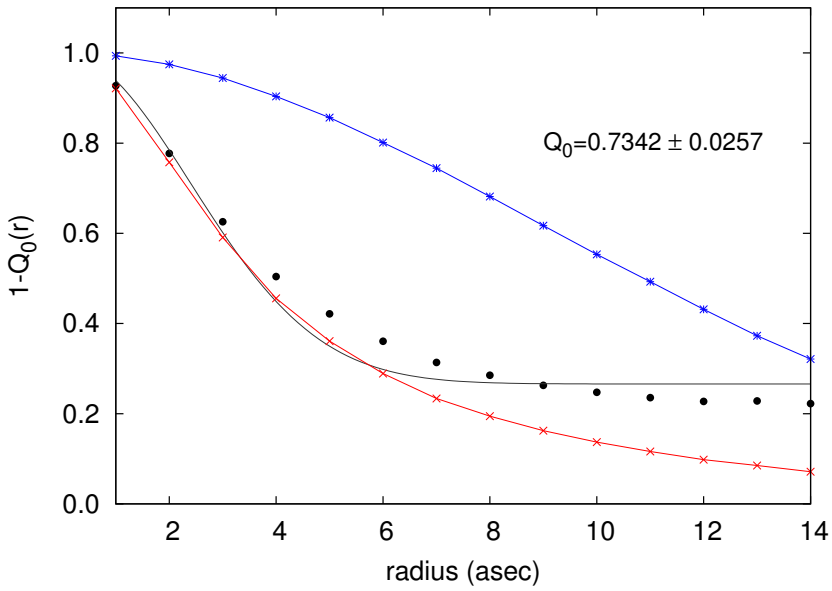

Figure 4.1: — Illustration of the procedure to estimate $1 - Q_0$. The red crosses show the fraction of blank SPIRE sources within search radius r, while the blue stars show the same fraction for random positions. The black filled circles represent the data points obtained from dividing the number of blank SPIRE positions by the number of blank random positions, our estimate for $(1 - Q_0)F(r)$. The black line represents the best fit to the model $(1 - Q_0)F(r)$, see equation (4.19), with $Q = 0.7342 \pm 0.0257$.

Having estimated the general value of Q_0, we still need to know the individual contributions from stars and galaxies, Q_{0s} and Q_{0g} respectively, with $Q_0 = Q_{0s} + Q_{0g}$. A drawback of the above approach is that we cannot separate our blank SPIRE fields into stars and galaxies. Therefore, we estimate the value of Q_{0s} in applying equation (10) of Smith et al. (2011), using a background subtracted sample of possible matches within 10 arcsec, yielding a value of 0.004. This is very small indeed and shows how unlikely it is that stars are detected with SPIRE. For our LR analysis we then adopt $Q_{0g} = 0.72$ and $Q_{0s} = 0.01$, the values for Q_0 used in the normalisation of $q(m)$ for galaxies and stars respectively .

4.2.3 Probability of mis-identifying a true counterpart

Given the above model, we now estimate $P(wrongID|m_{true})$, defined to be the probability that a true counterpart with a given VIKING K_s magnitude m_{true} is not the best candidate using our LR method. This situation occurs, if the true counterpart has a likelihood ratio value $L = L_i$ and there exists a chance match with $L > L_i$ for the same source. Hence:

$$P(wrongID|\, m_{true}) = \int_0^{L_{max}} P(L_i|m_{true}) \times P(chance > L_i)\, dL_i \tag{4.25}$$

The probability $P(chance > L_i)$ that there exists a chance match with $LR > L_i$ for one SPIRE source can be estimated through simulations. The steps of the procedure we have used are as follows:

1. Create N random positions on an area common to both VIKING and H-ATLAS in the G09 field

2. For each random positions, calculate the likelihood ratio L for random matches, if any, in the VIKING catalogue.

3. Create the distribution $D(L)$ of the highest likelihood ratio value for each random position.

From the probability distribution $D(L)$ of the highest LR values for candidate matches to random positions, we can calculate the probability that a given source has a chance candidate above L_i by chance:

$$P(chance > L_i) = \frac{1}{N} \int_{L_i}^{L_{max}} D(L)\, dL \tag{4.26}$$

A similar method has been employed by Dye et al. (2009) to calculate the probability of radio associations to the BLAST (Balloon-borne Large Aperture Submillimetre Telescope) sub-mm sources. Fig. 4.2 shows the resulting distribution $D(L)$ from $> 10^6$ random positions, together with the histogram of the likelihood ratio values of the candidate matches to the real SPIRE positions and of the subset of reliable counterparts.

The probability $P(L_i|m_{true})$, the first factor in the integral in equation (4.25), that a true counterpart with K_s magnitude m_{true} acquires the likelihood ratio L_i can be calculated analytically from the probability distribution $P_r(r) = 2\pi r f(r)$ of the

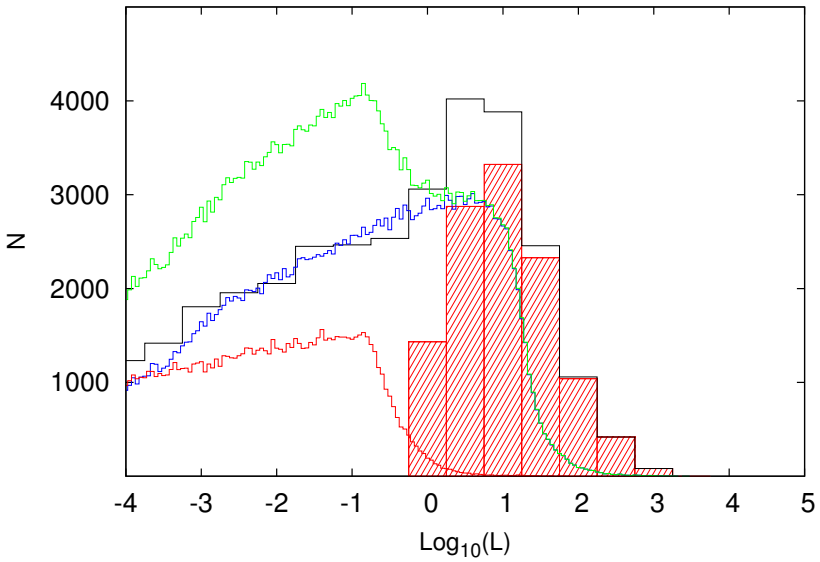

Figure 4.2: — The solid green line shows the distribution $D(L)$ of the highest L values of candidate matches to $> 10^6$ random positions in the G09 field. The peak at lower L values is due to stars whereas the plateau at $1 < L < 10$ is caused by galaxies; the individual distributions for stars and galaxies are shown as red and blue lines respectively. The black histogram represents the LR values of all candidate matches to the SPIRE positions. The filled red histogram represents the reliable matches only.

offsets. For a given $m = m_{true}$ we have $f_i = f(r) = L_i \times n(m_{true})/q(m_{true})$ and hence $P(L_i|m_{true}) = P_f(f_i)$. We can find the probability distribution $P_f(f)$ from $P_r(r)$ by performing a variable transformation:

$$P_f(f) = -P_r(r(f)) \times \frac{dr}{df} = 2\pi\sigma^2 \tag{4.27}$$

This is a surprisingly simple result, i.e. for Gaussian errors, $P_f(f)$ has a uniform distribution between 0 and its maximum value $1/2\pi\sigma^2$. We would like to note though that the positional uncertainty depends on the value of the SNR. For simplicity, we have used the value of $\sigma_{pos} = 2.4''$, allowing for most of the SPIRE sources to have a SNR value close to 5. A more detailed analysis could take into account the probability distribution of the SNR values of all SPIRE sources.

Having calculated the probability of a true counterpart with assumed magnitude m_{true} not being the best candidate in our LR method, we can then calculate $P(wrongID)$, the same probability integrated over the model magnitude distribution of the true counterparts:

$$P(wrongID) = \frac{\int_0^{M_{lim}} P(wrongID|m)\, q(m)\, dm}{\int_0^{M_{lim}} q(m)\, dm} \tag{4.28}$$

Using the distribution $D(L)$ from the random positions, our VIKING sample as described in section 2.1.1 to derive the magnitude distributions $q(m)$ and $n(m)$, as well as $\sigma_{pos} = 2.4''$, we obtain $P(wrongID) = 0.0493$. We hence expect to mis-identify around $\sim 5\%$ of the true VIKING counterparts to the SPIRE sources. This is likely to overestimate the true value because we have not taken the individual SNR values of the SPIRE sources into account.

4.3 Matching results

4.3.1 K_s identifications

There are 22,000 SPIRE sources within the sky area corresponding to the G09 VIKING object catalogue. Of those, 18,989 sources have at least one possible match within a search radius of 10 arcsec in the VIKING K_s band selected catalogue, with a total of 35,800 candidate matches; of which 30,659 are classified as galaxies (85.6%) and 5,141 are classified as stars (14.4%), as described in section 2.1.1.2. Table 4.1 shows the

number of SPIRE sources matched as a function of the number of candidate matches found per position.

There are 11,294 SPIRE sources with a best VIKING counterpart with a reliability of $> 80\%$ (11,282 galaxies/12 stars). This means we were able to match $\sim 51\%$ of the SPIRE sources with a high reliability. We will refer to the set of matches with $R > 0.8$ as "reliable" hereafter (as we show later, the mean reliability of this set is near 0.95). Fig. 4.3 shows the magnitude dependent distribution $q(m)/n(m)$ for galaxies and stars used in the calculation of the LR values. Fig. 4.4 and 4.5 show the magnitude distributions involved, of the background $n(m)$, of the possible matches $total(m)$ and of the background subtracted sample $real(m)$, in estimating $q(m)$. Also shown in the figures is the magnitude distribution for reliable counterparts. The reliable matches show a lower fraction of fainter counterparts compared to all candidate matches, representing the steep increase of fainter objects in the background number counts, causing lower reliability values for fainter matches.

We can estimate a false ID rate by summing up the complement of reliability values of the reliable matches:

$$N_{falseID} = \sum_i (1 - R_i) = 469.25 \tag{4.29}$$

corresponding to a mean reliability of 0.958 and a false ID rate of 4.2%.

4.3.2 VIKING and SPIRE colours

Figure 4.6 shows the ZJK colour-colour diagram of the 10,121 reliable counterparts (red) with 5σ detection in all 3 VIKING bands. Colours from randomly selected background galaxies are depicted in grey. The redshift evolution of the sub-mm selected mean galaxy template of Smith et al. (2012) is shown in green. The template has been artificially redshifted between $z = 0 - 1.5$ in intervals of $dz = 0.1$ and colours have been computed by integrating the product of the template SED with the VISTA response functions at each redshift interval. A small deviation from the Vega system is present in the VISTA Z-band and a measured offset (Findlay et al., 2012) has been added to the colours computed here to reflect this.

The median $Z - J$ and $J - K_s$ colours for the reliable matches are 0.97 and 1.64; for the background objects the median colours are 0.89 and 1.54. Performing a two-sided

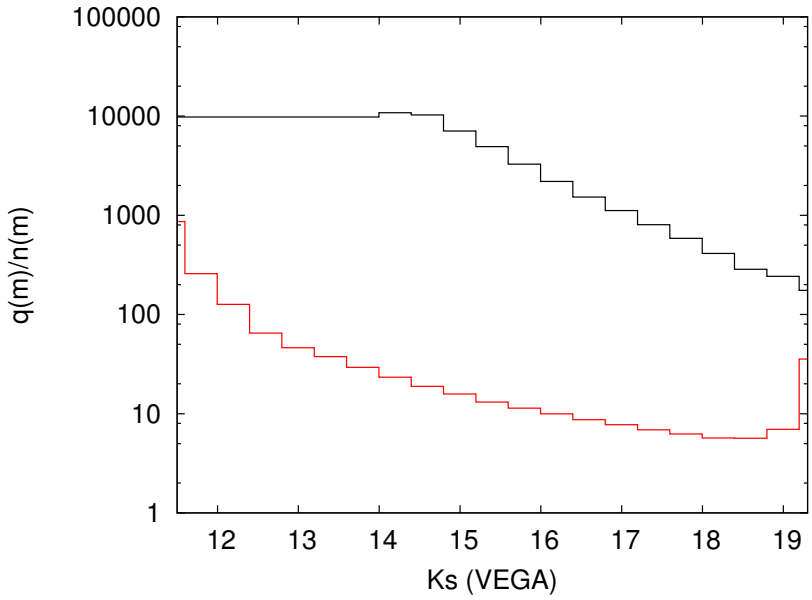

Figure 4.3: — The magnitude dependent part $q(m)/n(m)$ of the LR analysis, calculated from the data as described in section 4.2.2. The black line indicates the galaxy candidates, the red line shows the stellar candidates. The values for the bright bins for the galaxy distribution were extrapolated from the first bin that included more than 10 galaxies, at $m = 13.4$.

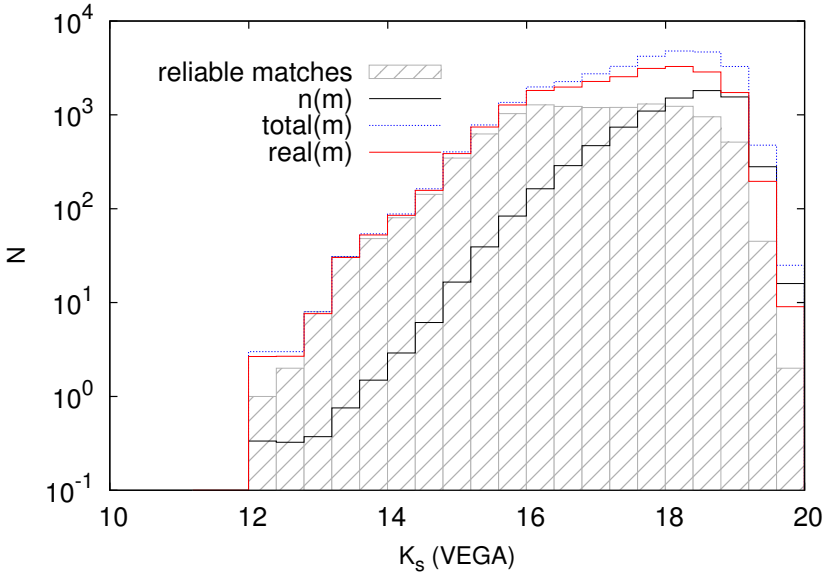

Figure 4.4: — The magnitude distributions involved in estimating $q(m)$ for galaxies. Here $n(m)$ (solid black) is the distribution of the background objects, calculated from the whole VIKING G09 catalogue, as described in section 2.1.1.2, and $total(m)$ (dashed blue) is the magnitude distribution of all possible matches within 10 arcsec. $real(m)$ (solid red) is the background subtracted distribution as described in section 4.2.2 and is significantly brighter than the background. The light grey shaded histogram represents the magnitude distribution of the reliable matches.

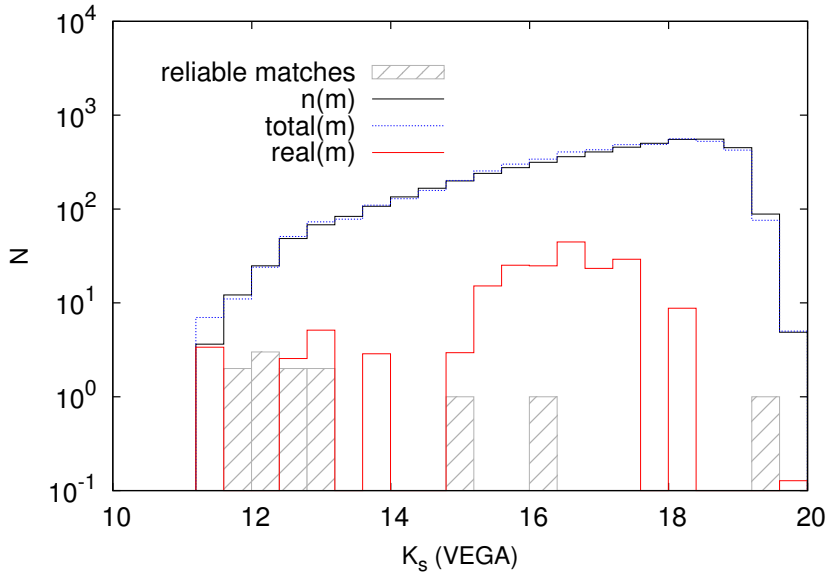

Figure 4.5: — The magnitude distributions involved in estimating $q(m)$ for stars. The colour scheme is as in Fig. 4.4.

Table 4.1: The distribution of the number of VIKING K_s band sources within 10 arcsec of the 250 μm SPIRE positions. Of the 22,000 sources in the VIKING area, 8118 have only one possible match within 10 arcsec and 59.7% of these are determined to be reliable. This emphasises the difference from a simple nearest neighbour match.

N(matches)	N(SPIRE)	N(reliable)	%
0	3011		
1	8118	4851	59.76
2	6619	4040	61.04
3	2968	1710	57.61
4	968	529	54.65
5	241	128	53.11
6	63	31	49.21
7	11	5	45.45
8	1	0	00.00
Totals	22,000	11,294	

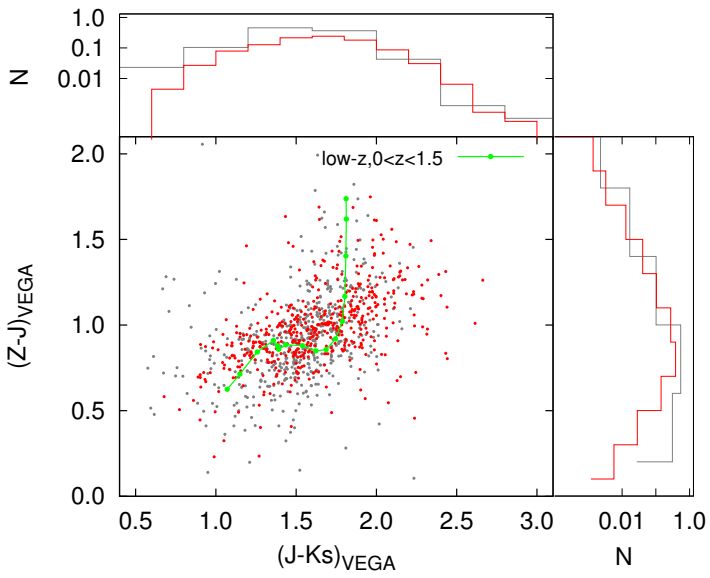

Figure 4.6: — VIKING colour-colour diagram of reliable counterparts (red) and background galaxies (grey) with 5σ detections in Z,J and K_s. The horizontal and vertical histograms show the distributions in $J - K_s$ and $Z - J$ respectively. The green points connected by a green line represent the evolutionary track of a typical H-ATLAS galaxy SED for $z < 0.35$ from Smith et al. (2011b) and calculated by Findlay et al. (2012).

K-S test on the $J - K_s$ and the $Z - J$ colours for reliable matches and the background objects enables us to reject at a significance of 99.96% that the two populations are drawn from the same distribution for either colour. Thus, we find evidence that the reliable matches to the SPIRE sources are slightly, but significantly redder than the population of all VIKING objects in the G09 field.

Within the search radius of 10 arcsec, 3011 sources have no 5σ K_s VIKING candidate, i.e. they are almost certainly fainter than the VIKING limit. Fig. 4.7 shows S_{250}/S_{350} histograms separately for the sources with a reliable match (best $R > 0.8$), sources with non-reliable match(es) (best $R < 0.8$), and for sources that are blank in VIKING (black, red and shaded red respectively). The blank sources (median=1.01) have distinctively redder colours than the sources with reliable matches (median=1.32), suggesting that they reside at higher redshifts with the peak of the dust emission moving to longer wavelengths. The colours of sources with unreliable matches (median=1.11)

lie in between the other two populations, indicating that they might be composed from members of both populations. The SPIRE fluxes for Fig. 4.7 (and Fig. 4.8) have not been corrected for confusion or Eddington boosting. Both effects are negligible for the 250 μm band, but become more pronounced in the 350 and 500 μm bands. If we do correct the fluxes, the median values for the ratios in Fig. 4.7 are shifted by +0.1; this does not affect our conclusions. A slight shift towards higher values is also seen in Fig. 4.8 and again, this does not affect any of the results.

From our value of Q_0, we expect around 60% of the unreliably matched sources to have a true counterpart, but for which we do not have a high enough reliability, with the remaining 40% being matched to unrelated background objects. Smith et al. (2011) find a similar trend in the distribution of the S_{250}/S_{350} colour of SPIRE sources in the SDP field matched to the SDSS r-band catalogue for the 3 different populations.

We also show a SPIRE colour-colour diagram of the sources in Fig. 4.8. The colours of the reliably matched and the blank sources are very similar to those in Smith et al. (2011), their fig. 9. This figure can also be compared to fig. 1 in Amblard et al. (2010). We add the evolutionary tracks of two templates: a low-z template compiled by Smith et al. (2012) from optical counterparts to SPIRE sources out to $z \simeq 0.35$ (blue line) and the sub-mm template from Lapi et al. (2011) (green line), thought to be appropriate for high-z H-ATLAS sources at $z > 1.2$. From the tracks of the two SED templates we can again suggest that the blank sources lie at higher redshifts in general than the sources with reliable matches. Assuming that the H-ATLAS sources are comprised of two distinct populations, see section 5.3, a lower redshift population with mainly normal galaxies (with a much higher star-formation rate than local normal galaxies), and a higher redshift population of dusty sub-mm galaxies (likely to be giant proto-spheroidal galaxies in the process of forming most of their stars), our blank sources could represent a mixture of the former at $z \gtrsim 0.7$ and the latter at $z \gtrsim 1.5$.

4.3.3 Multiple counterparts

The LR method assumes that there is only one true counterpart to each source, and assigns reliabilities self-consistently based on this, so that the sum of reliabilities cannot exceed 1. Thus, if more than one counterpart with $R > 0.2$ is present, we will not find a reliable match. If individual reliabilities add up to our threshold of 0.8, we could

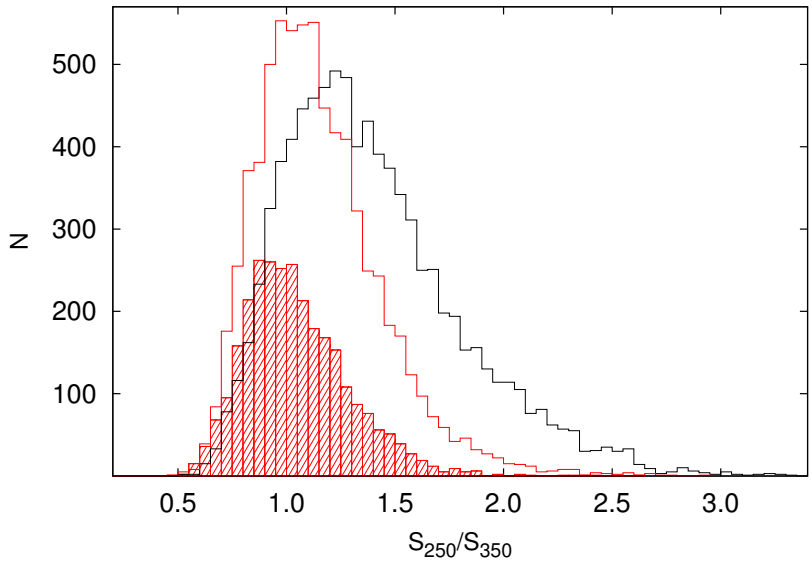

Figure 4.7: — Distribution of the SPIRE S_{250}/S_{350} colour. Black: sources with reliable matches. Red: sources that have unreliable matches only. Red shaded: blank sources. The blank sources show distinctively redder colours than the other two populations, suggesting they are at higher redshifts.

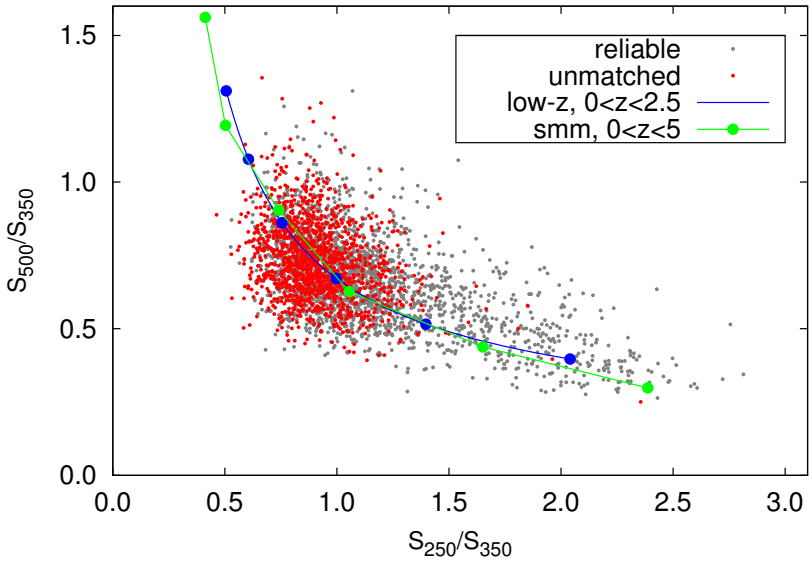

Figure 4.8: — Colour-colour diagram of SPIRE objects with 5σ detection in $250\mu m$ and $350\mu m$ and 3σ detection in $500\mu m$. The dark grey points represent SPIRE sources that have reliable counterparts, the red points show the colours of blank SPIRE sources. The blue points connected by the blue line represent the colours of a typical H-ATLAS galaxy SED for $z < 0.35$ from Smith et al. (2012). The dots are at an interval of $z = 0.5$, starting at $z = 0$ on the right hand side. The green points connected by the green line represent the colours of the sub-mm SED in Lapi et al. (2011). The points are at an interval of $z = 1$, starting with $z = 0$ on the right.

assume that these candidate matches are all associated with the sources, either through confusion or in a real physical sense (i.e. merging galaxies).

In our results, we find 1444 SPIRE sources that fulfill the above criteria and potentially have multiple true counterparts in VIKING. Most of those will have additional close chance objects within the search radius, denying a reliable identification, but some might be genuine mergers or constitute members of the same cluster. We can rule out a chance match by comparing the redshifts of all possible matches to one SPIRE source. Checking for available redshifts in the GAMA and SDSS spectroscopic redshift databases, we find matches to 37 sources whose redshifts are within 5% of each other. The mean redshift difference is 0.0011 with a maximum difference of $\triangle z = 0.0187$. Those could be either merging galaxies or members of the same cluster.

We use our photometric redshifts, see section 5.3, to select further candidates. We account for the higher errors in the photometric redshifts by allowing a redshift difference of 10% and also compare photometric redshifts of possible matches for which we do not have a spectroscopic redshift with spectroscopic redshifts of other candidates to the same source. We find 602 further sources where the SPIRE flux potentially originates from an interacting system or from galaxies within the same cluster. Fig. 4.9 shows a VIKING K_s image cutout around one of the those sources, HATLAS J091017.1-005538. Due to the uncertainties in the photometric redshifts, those sources can only be regarded as candidates and need further investigation to be confirmed as interacting systems or as members of the same cluster.

It would be interesting to confirm how many sources definitely do not have physically related multiple counterparts and are just unreliable matches, but this is difficult due to the sparsity of available spectroscopic redshifts and the uncertainties on the photometric redshifts. However, we can estimate the number of reliable identifications we are missing due to potentially multiple counterparts. From Table 4.1, we can see that the identification rate for reliable counterparts is approximately 60% without the presence of additional potential matches. We do not see a decrease in the identification rate for sources with two possible matches, suggesting that the true number of merging galaxy pairs is indeed low. For sources with higher numbers of possible matches, we have an increased possibility of having observed a galaxy cluster and so the identification rate for reliable matches falls. For instance, sources with 4 possible matches have an identification rate of around 55%, suggesting that we miss 5% of the reliable

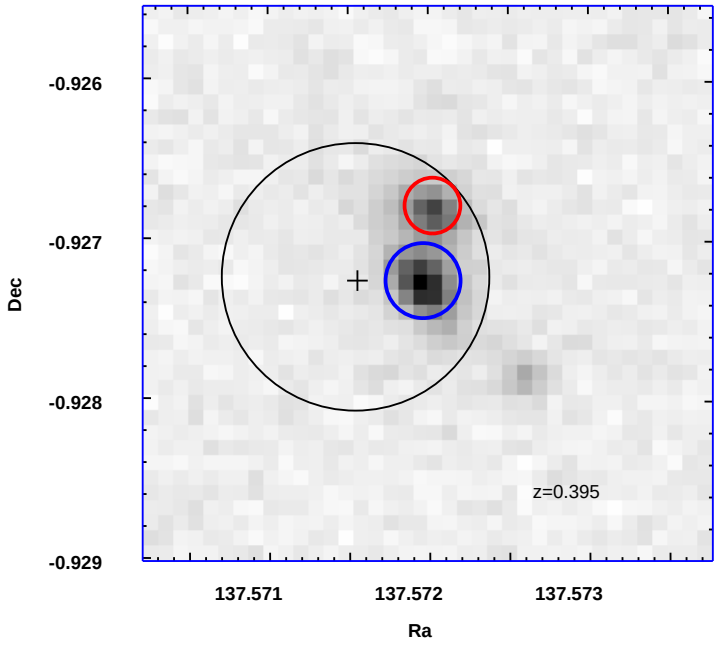

Figure 4.9: — VIKING K_s image of HATLAS J091017.1-005538, 15 arcsec on the side. The black cross indicates the SPIRE position and the black circle represents the $2\sigma = 2.9''$ positional uncertainty of this SPIRE source. The blue circled object has reliability $R = 0.74$, the red circled object has $R = 0.25$. The third candidate has negligible reliability, but could still be part of the interacting system.

matches, equivalent to 50 sources. Adding up the missed reliable matches of all sources with more than 2 possible counterparts, suggests that we are missing around 150 reliable VIKING counterparts due to additional matches within our search radius. This is a small number indeed, only around 10% of the number on our list of candidates for true multiple counterparts. There is evidence, from observation and simulation, for the merger rate to evolve with redshift and to peak at $z \simeq 1.2$ (Bell et al., 2006; Lotz, 2007; Ryan, Jr. et al., 2008), beyond the redshift of most of our reliable counterparts. Hence, we might miss a substantial fraction of mergers not because we find multiple candidates but rather because they hide in the fraction of blank SPIRE sources. This implies that our candidate list comprises mostly either chance alignments of galaxies or cores of clusters of galaxies resulting in confusion when observed with SPIRE.

4.3.4 Stellar matches

The far-infrared/sub-mm mainly detects cold, dusty objects. It is unlikely that stars are detected with SPIRE, unless they are post-AGB, shrouded in dust or have debris disks (e.g. Thompson et al., 2010). We have matched 12 SPIRE sources reliably to point-like objects. Their location on the $J - K_s$ vs $g - i$ colour-colour diagram is displayed in Fig. 4.10.

HATLAS J090450.4-014525 (884 in Fig. 4.10) displays galaxy-like colours and is listed as a QSO in the quasar catalogue of Véron-Cetty & Véron (2010). All other objects are consistent with having star-like colours.

Two blazars were identified by González-Nuevo et al. (2010) in the SDP field from cross-matching to radio observations. We match H-ATLAS J090910.1+012135 reliably to a point-like VIKING object (sgmode= 10, i.e. point-like object classified as a galaxy on the basis of a non-stellar spectroscopic redshift). H-ATLAS J090940.3+020000 is not matched reliably within our search radius of 10 arcsec. We find one possible VIKING counterpart within 10 arcsec of this SPIRE source: a bright point-like object ($K_s = 15.03$, sgmode= 10), lying at a distance of nearly 9 arcsec from the SPIRE position and therefore obtaining a low reliability. However, it lies within 1 arcsec of the known blazar PKS 0907 +022, the object identified as the blazar counterpart to H-ATLAS J090940.3+020000 by González-Nuevo et al. (2010). Despite the low reliability, there is hence evidence that our VIKING object is the counterpart to H-ATLAS J090940.3+020000. The colours of both VIKING objects are shown in Fig. 4.10 as blue dots. Blazars in the H-ATLAS Phase 1 fields are currently investigated by a team led by Marcos Lopez-Caniego with 14 candidates identified so far.

For the brighter stars, it is a possibility that the measured SPIRE flux originates from a galaxy that is too faint in the near-infrared to be detected by VIKING, or obliterated by the star, and the star is a chance projection. The reliabilities of star counterparts are on average lower ($\bar{R} = 0.85$) than for the reliable galaxy matches, due to the lower Q_0 value and the lower values of $q(m)$ (see Fig. 4.3).

4.3.5 Towards more complete identifications

So far we have estimated that 73% of SPIRE sources have counterparts in VIKING, while 51% have a reliable match; thus, the reliable sample comprises approx 51/73 =

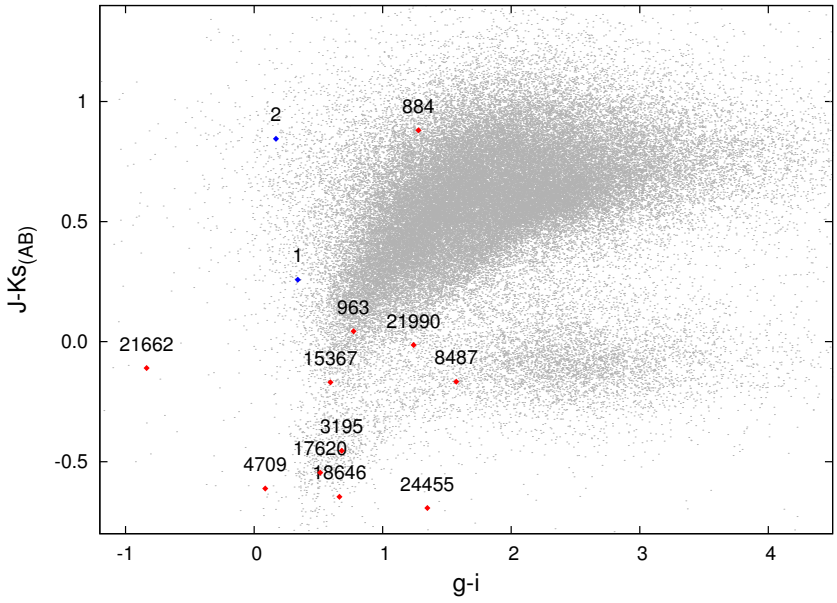

Figure 4.10: — Reliable stellar matches, represented by the red dots. For clarity we have labeled the dots with row numbers from the SPIRE catalogue and not with the full HATLAS names. HATLAS J090450.5-014525 (884) has galaxy-like colours and was originally selected to be a QSO target of the Sloan spectroscopic survey but has subsequently been rejected as a target. It is listed as a QSO in the Quasar and Active Galactic Nuclei catalogue by Véron-Cetty & Véron (2010) with redshift $z = 1.005$. The colours of the other objects are consistent with being star-like. The extreme $J - K_s = -2.67$ value of HATLAS J091233.9-004549 is not shown in the diagram and could be due to saturation. The blue dots represent the colours of the VIKING counterparts to the two blazars found in the SDP field, 1 =H-ATLAS J090910.1+012135, 2 =H-ATLAS J090940.3+020000

70 percent of all SPIRE galaxies with both $f_{250} > 32\,\mathrm{mJy}$ and $K_s < 19.2$. Of the remaining 49% of SPIRE sources, 14% are undetected in VIKING and 35% have one or more low-reliability match(es); overall we expect around half of these to be genuine matches.

To make this decisive, we would need follow-up observations such as radio[6] or ALMA (Atacama Large Millimeter/submillimetre Array, Wootten & Thompson, 2009) imaging giving a sub-arcsec position, or possibly optical/NIR spectroscopy of VIKING candidates (if we can identify SPIRE sources via unusually strong emission lines). This would normally be "decisive" in that a sub-arcsec radio/sub-mm position would either match a VIKING galaxy to very high reliability, or if not it would prove the source is fainter than the VIKING limit.

For non-reliable matches, the total reliability $\sum R_i$ for a given source is a good estimate of the probability that the SPIRE source has a real counterpart in VIKING, i.e. the probability that a follow-up will actually find a good match; therefore in a follow-up search we should target the non-reliable matches in descending order of total probability.

Assuming a lower limit of the total probability of 50% (70%) would result in an additional 2380 (1856) identifications for 2967 (2101) observing targets. We would then obtain a sample which is 85% (82%) complete to $f_{250} > 32\,\mathrm{mJy}$ and $K_s < 19.2$. If we would use all non-reliable positions as targets, regardless of the total reliability, we would only be able to reach a completeness of 89%. This effect can also be seen in Smith et al. (2011) where the sum of the reliabilities to all possible counterparts would result in a 44% identification rate, lower than expected from their value of $Q_0 = 0.59$. This shows that our (and their) reliabilities might be underestimated; this is more evidence for a likely non-Gaussian positional error distribution which will be addressed in future publications of the catalogue.

Of additional consideration is our candidate list for multiple identifications, see section 5.3. They display a total reliability of 80% by definition and would hence be included in a possible target list. It would be interesting to see how many of those could be confirmed as true multiple identifications.

[6] Better positions, and greater efficiency of IDs will be possible with the ASKAP radio survey EMU (Norris et al., 2011) which will have 10" angular resolution and cover a redshift range quite similar to H-ATLAS.

Fig. 4.11 shows the distribution of the total reliabilities for the non-reliable SPIRE positions together with the number of additional identifications we would expect if we followed up all SPIRE positions down to 50 or 70 percent.

It is also useful to compare to the results of Dunlop et al. (2010); as described above, they identified a much smaller sample of 20 BLAST 250 μm sources, but benefiting from the very deep multiwavelength data in GOODS-S. In their sample, all candidate identifications with $z < 1.2$ are brighter than $K_s < 19.6$, while all at $z > 1.2$ are fainter; this suggests that the 3011 sources without a VIKING counterpart have a high probability of being at $z > 1.2$, and the same applies for the 3194 sources with low-reliability matches $\sum R < 0.2$.

Since the flux ratio f_{870}/f_{250} strongly increases with redshift for typical SMGs, the non-identified sources are therefore good targets for ALMA 870 μm follow-up snapshots; this could give a relatively efficient method for selecting luminous high-z SMGs.

4.4 Comparison to optical identifications

4.4.1 Reliable counterparts

In this section we compare our results with the optical identifications supplied with the H-ATLAS G09 Phase 1 source catalogue. This used a similar likelihood ratio method with an r-band selected sample down to $r = 22.4$, as explained for the SDP data in Smith et al. (2011). The VIKING K_s-band should be better placed than the optical r-band in identifying counterparts to the SPIRE sources. As discussed in the introduction, at higher redshifts ($z \geq 0.5$), the K_s band is detecting flux from the near-infrared restframe, while the r band is restframe blue/UV; thus K_s is much better able to detect dusty galaxies. We therefore expect a higher number of reliable identifications from matching with VIKING than with SDSS. To be able to compare our results, we cross-match our VIKING candidate matches with the SDSS database (DR7) within 2" and choose the nearest (primary) object.

We concentrate on the reliable counterparts of both surveys. The Phase 1 catalogue lists 9623 reliable optical counterparts (36.5%) to 26,369 5σ SPIRE sources in the G09 field; of the reliable counterparts, there are 8587 (39.0%) in the VIKING observed area.

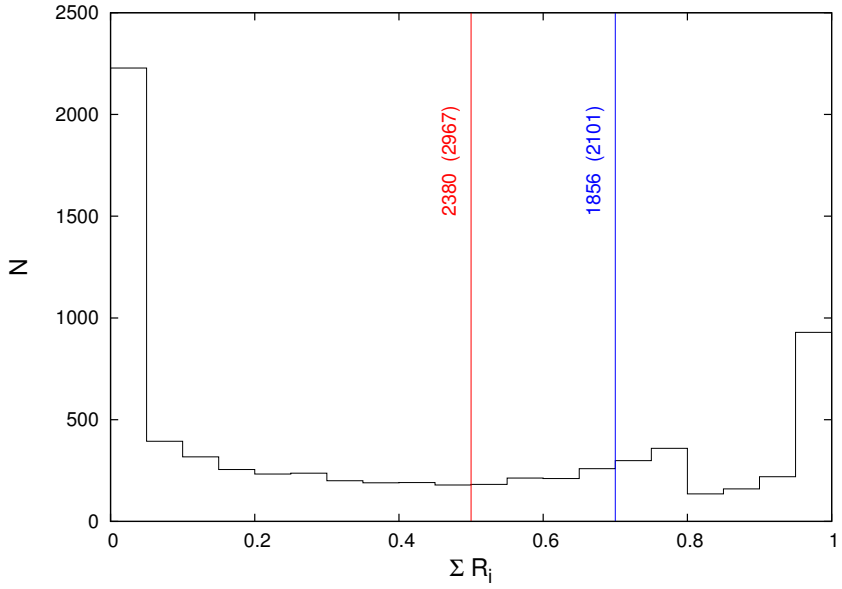

Figure 4.11: — Total reliability distribution of the non-reliable SPIRE sources. For the 7391 sources without a reliable counterpart, we sum the reliabilities of all possible VIKING counterparts per source. This total reliability is an estimate of the probability that the SPIRE source has a real counterpart in VIKING. If we include all SPIRE positions with total reliabilities greater than 50% for a follow-up, we will have to observe 2967 positions and expect to gain 2380 additional reliable VIKING counterparts (red line and text). The blue line and text show the equivalent for a 70% total reliability.

Table 4.2: — Comparison of the reliable counterparts to the SPIRE sources using optical r-band and near-infrared Ks-band matching. In the area corresponding to the VIKING preliminary source catalogue, we match reliably 51.3% of all SPIRE sources. This is a significant increase in the identification rate compared to the 39.0% of sources that are matched reliably to a SDSS object.

band	N(SPIRE)	N(matches)	N(reliable)	N(reliable) in VIKING area	with SDSS in VIKING area	N(reliable) not reliable in K_s	r
K_s	22,000	35,800	11,294 (51.3%)	11,294 (51.3%)	8,750	-	3,732
r	26,369	36,839	9,623 (36.5%)	8,587 (39.0%)	8,587	1,024	-

In comparison, we are able to match 11,294 SPIRE sources (51.3%) reliably to VIKING K_s objects.

We find a reliable K_s counterpart for 3732 SPIRE sources without a reliable optical counterpart. Of the 3732 positions, 1717 are blank in SDSS ($\sim 21\%$ of all SDSS blank fields), i.e. they are too faint to be detected in SDSS. Fig. 4.12 shows the K_s magnitude distribution of the counterparts to the 1717 SPIRE positions that are optical dropouts (red solid line). Unsurprisingly, the magnitudes are rather faint, with a median of $\tilde{K_s} = 18.26$, compared to the magnitudes of all reliable K_s counterparts with a median of $\tilde{K_s} = 17.07$.

The remaining 2015 SPIRE positions have optical counterparts, but their reliabilities lie below the threshold of $R > 0.8$. Fig. 4.12 (black solid line) shows the r modelmag distribution of the 3085 candidate matches to those 2015 SPIRE sources from which we can see that they belong mostly to the faint end of the overall magnitude distribution.

Conversely, there are 1,024 sources with optical reliable counterparts for which we did not find a reliable K_s counterpart. Only 121 of those positions are blank in K_s, mainly due to quality issues like saturation or bad pixels; the remaining 903 sources share 2261 VIKING candidates, of which 706 have reliabilities with $0.5 < R < 0.8$. Comparing to our multiple candidates, see section 4.3.3, we find that 590 of our 903 sources are indeed included in our candidate list of 1444 sources. We also find 14 sources that have confirmed multiple counterparts (by spectroscopic redshift). Over half of the reliable matches we miss when compared to the optical identifications, could hence be genuine multiple counterparts.

It is interesting to consider for how many SPIRE sources the VIKING and SDSS matching disagree on reliable counterparts. 7563 SPIRE sources ($\sim 88\%$ of the reliable optical matches in the VIKING area, $\sim 67\%$ of the reliable VIKING matches) are matched reliably in both surveys. Here, 7404 are matched to the same object. This leaves only 159 SPIRE sources (2.1% of matches) where the identification disagrees. Some of those are deblending issues; often though we find that the reliable optical counterpart is too faint in the K_s band and/or the VIKING counterpart is too faint

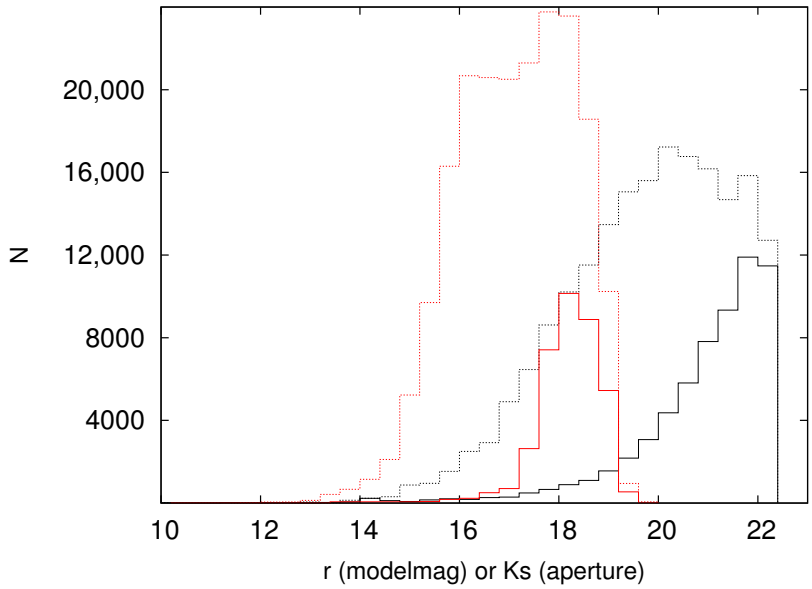

Figure 4.12: — The magnitude distributions of reliable K_s counterparts to SPIRE sources without reliable optical counterparts. The black histograms show r (modelmag, AB) distributions, the red histograms show K_s (aperture, Vega) magnitude distributions. The dashed histograms represent all reliable counterparts. The black solid line shows the r magnitude distribution of the non-reliable optical matches to SPIRE sources with reliable K_s counterpart. The red solid line shows the distribution of K_s magnitudes of optical drop-outs with reliable K_s counterpart.

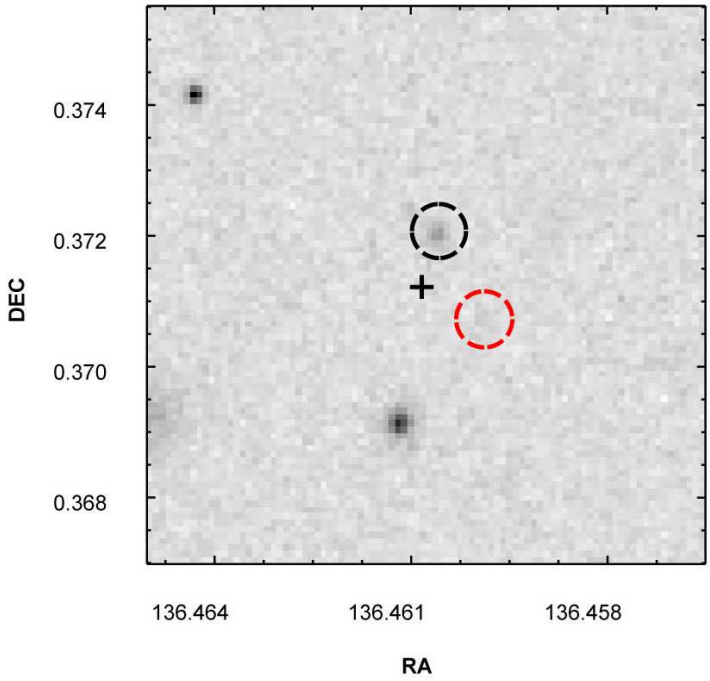

Figure 4.13: — VIKING K_s image of HATLAS J090550.5+002216, 30" on the side. The black cross marks the SPIRE position. Red circle: reliable SDSS counterpart ($R = 0.85$), black circle: reliable VIKING counterpart ($R = 0.96$). In the optical, the VIKING counterpart is detected with $r = 23.16$, fainter than the limit of $r = 22.4$ used in the matching by Smith et al. (2011).

or not detected in the r-band, resulting in different identifications. Fig. 4.13 shows an example, HATLAS J090550.5+002216.

4.4.2 Stellar counterparts

Of our 12 reliable stellar matches, 7 have reliable SDSS counterparts. Here, 2 have been classified as galaxies in the Phase 1 catalogue, HATLAS J091233.9-004549 and HATLAS J085353.2+001648 (10930 and 21662 in Fig. 4.10). Both are clearly stellar, showing diffraction spikes in both SDSS and VIKING images. The reliabilities of the stellar matches to the remaining 5 sources are high with $0.43 < R < 0.78$.

Conversely, in the optical catalogue there are 21 reliable stellar matches: of these,

19 are in the VIKING area, of which 5 are matched reliably to a VIKING star, 7 stellar objects are not included in our VIKING sample due to saturation in K_s, and 7 more are matched, but do not reach $R > 0.8$ (but have reliabilities > 0.4).

Chapter 5

Photometric redshifts

> "Very soon the heavens presented an extraordinary appearance, for all the stars directly behind me were now deep red, while those directly ahead were violet. Rubies lay behind me, amethysts ahead of me." *Olaf Stapledon*[1]

Information on the distance of objects is needed for a wide range of areas in astronomy. The construction of a 3D picture of our observable universe, its large-scale structure, demands the knowledge of distances. Any attempt on understanding or describing the evolution of certain properties of galaxies (e.g. luminosity, star formation rate, gas content etc.) necessarily has to include the ages of the galaxies. Because of the finite speed of light, we are looking back in time when observing the distant universe. Distance is hence a sort of proxy for the relative ages of galaxies.

A shift of the SED of nearby galaxies towards longer wavelengths was observed by Hubble (1929) from which he concluded that the galaxies are moving away from us. Because the shifts increase with growing distance, he also concluded that the universe is expanding. This shift is called redshift, as optical wavelengths moved towards the red. Section 5.1.1 provides more detail on the redshift of a galaxy and how it can be obtained, while section 5.1.2 provides the link between redshift and distance in an expanding universe.

[1] Olaf Stapledon, 1886-1950, from Star Maker, 1937

For investigations that rely more on a statistical knowledge of redshifts of a large number of galaxies, e.g. large-scale structure and baryon acoustic oscillation measurements, spectroscopic redshifts are time-consuming and cost-intensive and are often impossible to obtain for very faint objects. It is hence of interest to find a method to estimate redshifts efficiently, even though accuracy is lost. This is where photometric redshifts play a dominant role.

In its original meaning, a photometric redshift (photo-z) is an estimate of the true (cosmological) redshift of an object using broadband photometry. The photometric information corresponds to a very low resolution approximation of the spectral energy distribution (SED). Other information can be used, for example angular size or some shape parameter, extracted from imaging. Here, we concentrate on the photo-z derived from optical and near-infrared photometry.

It has been pioneered by Baum (1962) using photometry in 9 different bands ranging from the ultraviolet (UV) to the near-infrared. The early attempts fitted SED templates, either observed or from theoretical stellar population models, to the photometry (either as magnitudes or colours). With the advent of CCD photometry and, to some extent of HST which obtained data on galaxies too deep for spectroscopy, calculating photo-z become more of a necessity. The template-fitting method has been refined and is still in use today, see section 5.2.1. From the mid-90s photo-z have also been estimated using fits derived from photometry of objects with spectroscopic redshift (the so-called training set). These empirical methods are described in detail in section 5.2.2. Hybrid methods, using a training set to improve on the selection of the SED template for an object are also available and are discussed together with the template methods. In section 5.2.2.2 we describe the method we are using to derive the photo-z of our VIKING-HATLAS sample and section 5.3 presents our results.

5.1 Distance measures in the Universe

5.1.1 Cosmological redshift

How do we measure the distance to an astronomical object from observing its light? As was discovered in the 1920s (Hubble, 1929), the observed light of galaxies is shifted more and more towards the longer wavelengths, so-called redshifted, the further away it is from us. This was already a known phenomenon called the Doppler effect: light from a source moving away from the observer appears stretched and hence redshifted. Observing all galaxies to be redshifted with increasing redshift for increasing distance[2], this is one of the key evidences that we live in an expanding universe. The redshift of a galaxy is therefore directly linked with its distance to us. Because it is due to the expansion of the universe, it is called the cosmological redshift. Hereafter, redshift always signifies cosmological redshift.

The redshift z is defined as:

$$z = \frac{\lambda_{obs} - \lambda_{em}}{\lambda_{em}} \qquad \text{or} \qquad z = \frac{\nu_{em} - \nu_{obs}}{\nu_{obs}} \tag{5.1}$$

where the subscripts *obs* and *em* refer to the wavelength or frequency at the time of observation and emission respectively.

If we know a priori the SED of a galaxy and we can sample light from different wavelengths ranges or a certain range then we can theoretically derive a redshift for this galaxy which in turn should supply us with a distance. Very reliable redshifts are obtained from spectroscopy, mainly by identifying known emission or absorption lines of the observed part of the galactic spectrum and noting by how much the feature has been redshifted in comparison to the spectrum of a reference galaxy. Redshifts acquired from an SED or parts of it are called spectroscopic redshifts (spec-z).

A current redshift survey underway is the GAMA survey (Driver et al., 2009), as mentioned in earlier sections. This spectroscopic survey at the Anglo-Australian Telescope (AAT) with the AAOmega (Smith et al., 2004) spectrograph obtains optical

[2]The so-called Hubble law. The distances involved were measured independently from Cepheid light curves.

spectra for ∼340,000 galaxies down to $r = 19.8$ using the 580V and 385R gratings. Up to 400 spectra can be acquired simultaneously within 2 deg field with a spectral resolution 37$\mathring{A}$ FWHM. Redshifts are obtained via cross-correlation with a template library.

5.1.2 Cosmological distances

In an expanding universe, the distance between two points changes constantly and several distance measures are available. Derived from the Robertson-Walker metric, the relationship between proper distance[3] D_P and redshift z is:

$$D_P(z) = c \int_0^z \frac{dz'}{H(z')} \tag{5.2}$$

where $H(z)$ the Hubble parameter as a function of redshift. Using the current value of the Hubble parameter, H_0, we simply get Hubble's law: $D_p = \frac{c}{H_0} z$ which is a good approximation for small distances. Currently used values for the Hubble parameter are $H_0 = 100h$ s^{-1} km^{-1} Mpc^{-1} where $0.70 < h < 0.75$.

The comoving distance D_C is defined as being constant for objects moving with the Hubble flow, i.e. with the expansion speed. The line-of-sight comoving distance is defined as:

$$D_C(z) = \frac{c}{H_0} \int_0^z \frac{dz'}{E(z')} \qquad \text{with} \qquad E(z) = \sqrt{\Omega_M (1+z)^3 + \Omega_k (1+z)^2 + \Omega_\Lambda} \tag{5.3}$$

where Ω_M quantifies the matter content, Ω_k the curvature and Ω_Λ the dark energy content of the universe. There is strong evidence that we live in a flat universe, so $\Omega_k = 0$; current best estimates from the Wilkinson Microwave Anisotropy Probe (WMAP) for the other cosmological parameters are $\Omega_M = 0.258 \pm 0.030$ and $\Omega_\Lambda = 0.742 \pm 0.030$, see Dunkley et al. (2009). We use the comoving distance in section 6.4.1 when calculating the 250 μm luminosity function.

Another distance measure, the luminosity distance D_L, is obtained by comparing the observed flux with the emitted luminosity. Knowing an objects bolometric luminosity

[3] distance measure between two points if we could measure instantaneously

does in theory allow us to deduce its distance from the bolometric flux observed. The bolometric flux S of an object at a distance D_L is given by:

$$S = \frac{L}{4\pi D_L^2} \tag{5.4}$$

and the luminosity distance can be deduced from the Robertson-Walker metric. If we only observe a certain wavelength or frequency range, as is usual with broadband photometry, then we need to include a factor that corrects for the flux being observed in a different band than it was emitted, the so-called k-correction. It is defined as the ratio of the observed over the emitted (differential) luminosities, $K = L_\nu / L_{(1+z)\nu}$. We also need to account for the redshifting of the bandwidth. together, it follows for the differential luminosity:

$$L_\nu = \frac{4\pi D_L(z)^2}{(1+z)} S_\nu K \tag{5.5}$$

In a flat universe $D_L = (1+z)D_C$; this leads to:

$$L_\nu = 4\pi D_C(z)^2 (1+z) S_\nu K \tag{5.6}$$

This equation is used in section 6.4.1 to calculate the 250 μm luminosities.

5.2 Photo-z codes

A huge variety of different approaches have been used to estimate redshifts from broadband photometry with a real surge over the last decade or so. A rough but important distinction of the methods available is into template based methods and empirical methods. Template based methods use SEDs (observed or synthetic) to compare the observed photometry to the expected photometry from each SED at different redshifts to choose the best fit. Empirical methods employ training sets of galaxies with known photometry and known redshift (mostly from spectroscopy) to find parametric fits to the data which allows the computation of redshifts for galaxies without known redshift.

Both types of approaches show advantages and disadvantages. Most empirical methods perform better if a complete training set is available (Collister & Lahav, 2004;

Hildebrandt et al., 2010), but cannot extrapolate very well. It is hence important that the training set represents the evaluation set (galaxies for which we would like to estimate the redshift) well in the distributions of redshift, ideally also in morphology and other physical parameters. Template based methods are better placed to extrapolate, but do depend crucially on the set of SEDs selected and their calibration. The set of SEDs should be representative of the types in the evaluation set. Care must be taken to incorporate adequate dust extinction and evolution of the SED with redshift. On the positive side, template based methods provide galaxy types and k-corrections in addition to the photo-z.

A recent comparison of the performance of 17 existing photo-z codes has been performed by Hildebrandt et al. (2010). They test systematic errors with PHAT0, a simulated catalogue of $> 180,00$ objects with $0 < z < 4$ of which 11,000 are without redshift. The catalogue is created by using one of the codes, a template-based method, and the performance of the other codes is measured by how good the codes are at recovering the redshifts. A second catalogue, PHAT1, consists of real data from the GOODS-N field with photometry in 14-18 bands from the NUV to MIR; it contains $\sim$ 2000 objects $\sim 25\%$ of which possess a spec-z for use as a training set. On the whole, empirical methods are performing well in PHAT0, but show generally a higher scatter in PHAT1, compared to template-fitting methods. The number of outliers, defined as $\triangle z > 0.15$ increases substantially for both template-fitting and empirical methods in PHAT1. The main reason for the worsening performance of the empirical methods is the very small number of objects available as a training set. For each photo-z code discussed in the next sections, we will also refer to their performance in the Hildebrandt et al. (2010) PHAT test.

In the following sections we will give an short overview of the most popular methods to date. We discuss template based and empirical methods separately and we devote a whole section to neural networks, the method of our choice to calculate photo-z for the HATLAS-VIKING sample.

5.2.1 Template fitting methods

Most template fitting methods use a mixture of empirical SEDs (from local galaxies) and theoretical SEDs (from stellar population synthesis models) to cover a wide range of spectral types and wavelengths. Theoretical templates are also employed to extent the empirical templates to shorter/longer wavelengths (UV/NIR) as the best observations are usually in the optical, and to extent them to higher redshifts.

A range of different template libraries is available and while most template-fitting codes come with a default library, some allow for the inclusion of extra SED and linear combinations of the templates. The most popular codes that are also publicly available are `hyperz` Bolzonella et al. (2000), `Le Phare` Ilbert et al. (2006) and `EAZY` Brammer et al. (2008).

The photo-z are calculated by minimising χ^2:

$$\chi^2 = \sum_{i=1}^{N_{filters}} \left(\frac{F_{obs,i} - F_{temp,i}(z)}{\sigma_i} \right)^2 \tag{5.7}$$

where i runs over all filters, F_{obs} and F_{temp} the observed and the template flux respectively and σ the uncertainty in the observed flux. The main source of catastrophic error lies in the degeneracy of galaxy colour and redshift: two template at very different redshifts can exhibit similar colours and the photo-z of the galaxy could deviate hugely from the true redshift. This error can be kept under control by using a minimal template library that reflects the galaxies best; increasing the number of templates might actually increase the potential for catastrophic outliers.

5.2.2 Empirical methods

The general principle for empirical methods is to find a parametrisation between the photometry, or possible other physical parameters, and the redshift. We concentrate here on some empirical methods that have been used for photo-z estimation with the exception of the neural networks, especially `ANNz`, which will be treated separately in the next section.

The earliest approach by Connolly et al. (1995) has been a quadratic fit to colours from $BVRI$ photometry, resulting in $\triangle z = 0.05$ for $B < 22.5$. They also show that the fluxes in the 4 bands are correlated by performing a Principle Component Analysis (PCA) enabling them to reduce the dimension to 2-3. Li & Yee (2008) also use quadratic polynomial fitting to the SDSS $ugriz$ magnitudes and colours, using a division into colour-magnitude cells of the training sample. In each cell they are using linear regression to obtain the coefficients of the polynomial; uncertainties due to the fitting process are estimated via bootstrapping[4] while errors due to photometry are investigated with a Monte-Carlo method assuming a Gaussian distribution for the photometric errors. Comparing with an independent set of objects with spec-z, they find that $\triangle z \sim 0.06$ for $0 < z < 1$. Their performance in PHAT0 is better despite the higher redshifts involved, but they still have one of the highest scatter and outlier rate compared to the other codes.

From DR7 onwards, SDSS data release include photo-z calculated using a nearest neighbour algorithm (Abazajian et al., 2009). The idea is intuitive: find k (100 in SDSS, 150 in PHAT) neighbours of the galaxy, with photometry but without redshift, in some magnitude/colour space of the training set. This set of neighbours is then used to calculate the coefficients of a low order polynomial. This can be cpu-intensive if the whole data set is searched for each galaxy we need a photo-z for. Often a so-called k-d tree indexing scheme is used to speed up the neighbour search, which takes the non-uniformity of the parameter distribution into account and ignores empty spaces, see Csabai et al. (2007).

A different variant to the nearest neighbour is the kernel regression method, see Wang et al. (2007), where the neighbours in the training set obtain different weights according to some function (the "kernel") of the distance. The estimated photo-z is then the weighted average of the spec-z of the neighbours. Wolf (2009) use this approach

[4] In bootstrapping, the process is run repeatedly with different draws from the original sample. The draws consist of selecting an object at random with replacement. An error can then be estimated from the scatter in the results.

with a Gaussian Kernel function producing a photo-z pdf for each galaxy from the weights which are in fact the photo-z probabilities. They achieve a good performance in PHAT1, with excellent bias and average scatter and outlier rate compared to other empirical methods.

A very popular class of method, next to neural networks (see section 5.2.2.1), to estimate redshift from photometry has been using decision trees in some form. Decision trees (DT, sometimes called regression trees) are sequential binary classifiers, at each level dividing data into two separate groups depending on some criteria from a root node comprising the whole data set down to the final nodes called leaves representing a subset of the data of some class or other parameter value. Two different methods have been used lately to estimate photo-z.

5.2.2.1 Artificial Neural Networks

A general definition of Artificial Neural Networks (ANNs) is given in Gurney (1997): "A neural network is an interconnected assembly of simple processing elements, units or nodes, whose functionality is loosely based on the animal neuron. The processing ability of the network is stored in the interunit connection strengths, or weights, obtained by a process of adaptation to, or learning from, a set of training patterns."

A wide range of applications for ANNs can be found, from medicine where they can be used to recognise illness patterns for diagnosis, to astronomy where they can be used to classify galaxy morphologies, spectra or indeed to estimate photometric redshifts, their relevance for us. The advent of ANNs started in the early 1940s (McCulloch & Pitts, 1943), modeling the functionality on the information processing of neurons in the brain. Not surprisingly, the first team was composed of neuroscientists and programmers at IBM. The motivation behind the development of ANNs is to facilitate pattern recognition and classification tasks. The most prominent aspects of the model (the artificial neuron) are the differently weighted input (connections to a neuron from other neurons that fire with different intensity) and the subsequent activation of the neuron depending on a threshold. Firing rules, or activation functions, decide on the

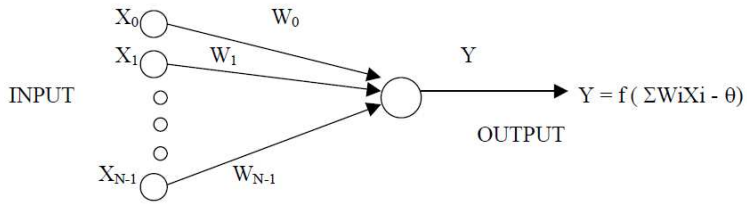

Figure 5.1: — Artificial network with a single layer architecture. N nodes produce N inputs for the output node. A bias θ is included. Figure from Lippmann (1987)

output, with artificial neurons being connected using the output of one neuron as part of the input for another. Fig. 5.1 shows the model of a simple one layer network. The learning process is emulated by allowing the weights for each input to be adaptable either in response to a pre-determined output (supervised learning), or just to the input data itself (unsupervised learning).

ANNs were not widespread until computing power became more readily available in the 1980s. They became more complex too and different network architectures were created, with multiple layers of nodes (the neurons) and a variety of activation functions. A short introduction follows, for a more detailed exploration of ANNs see Bishop (1995) and Gurney (1997).

The three important components of an ANN are the network architecture (the nodes and its connections), the activation rules and the learning rule. The network architecture states the number of input values, the number of layers of nodes, the number of nodes in each layer, the number of output values and the direction the information travels. Fig. 5.1 shows a single layer network, fig. 5.2 shows a two layer network. A layer of nodes that lies between the input and the output layer is called a hidden layer. The most important distinction between network architectures is that of feed-forward and feedback networks. In a feed-forward architecture, the inputs are processed in a strict forward rule, i.e. only outputs of nodes from a layer before the current layer are used as inputs and the current outputs are forwarded to the next layer only, as shown in the example in fig. 5.2. It is often represented in the form

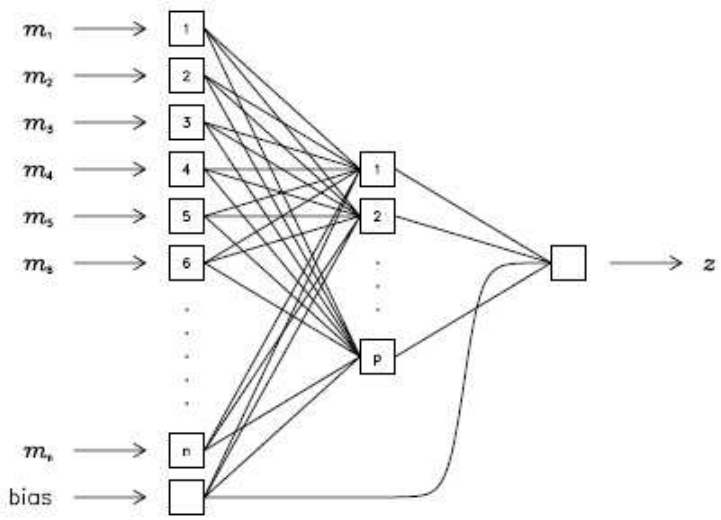

Figure 5.2: — ANN with a two layer architecture: one input layer (plus bias), one hidden layer and the output layer. Figure from Collister & Lahav (2004).

$N_{in} : N_1 : N_2 : ... : N_m : N_{out}$ where N_{in} (N_{out}) the dimension of the input (output) vector and N_i the number of nodes in the ith layer. In feedback networks, nodes can loop back to nodes in previous layers or to themselves and information can travel in any direction. Feed-forward networks have the advantage that the process can be represented as a unique function of the input variables and are often preferred if the model allows it.

Activation rules, sometimes called transfer functions, are the functions that determine the individual output at a node, depending on the weighted input. The function used are generally of three types: linear, threshold (Heaviside function) and sigmoid. The latter is the most closely modeled on the neuron and is represented as either $g(x) = \tanh(x)$ or $g(x) = \frac{1}{1+\exp(-(x-\theta)/\rho)}$ where x the input to this node from the previous layer and ρ and θ shape parameters (ρ makes the curve steeper with decreasing values, θ moves it along the x-axis). Fig. 5.3 shows the activation function with $\rho = 1$ and $\theta = 0$. A motivation for the use of the sigmoid can also be drawn from its relation to the posterior probability. This can be illustrated in the case of a single layer network that is a two-case classifier, i.e. a network with just an input and an output

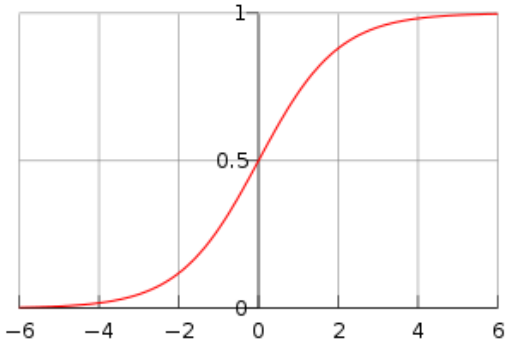

Figure 5.3: — Example of a sigmoid activation function with $\rho = 1$ and $\theta = 0$.

layer that sorts objects into two different classes C_1 and C_2 (see Bishop, 1995, p.82). The posterior probability $P(C_1|x)$ at the output node that the object is classified into C_1 is then:

$$P(C_1|x) = \frac{P(x|C_1)P(C_1)}{P(x|C_1)P(C_1) + P(x|C_2)P(C_2)} = \frac{1}{1+e^{-a}} = g(a) \tag{5.8}$$

$$\text{where} \qquad a = \ln\left(\frac{P(x|C_1)P(C_1)}{P(x|C_2)P(C_2)}\right)$$

The input a into the activation function can hence be interpreted as the natural logarithm of the odds of a classification into C_1.

In a feed-forward network, the output u_j at node j is:

$$u_j = \sum_i w_{ij} g(u_i) \tag{5.9}$$

where w_{ij} the weight of the connection between node i in the previous layer and node j in the current layer and u_i the output of node i in the previous layer.

How can a network learn? Given the architecture and the activation function, the outputs are determined by the weights, as shown in the previous equation. For a network to learn it has hence to be able to change its weights to adapt to a desired, predefined outcome (the training values). Presented with a training set of inputs plus fixed outcome values, the outputs of the network are then compared with the training output values and changed until the differences are minimised. Mathematically this can

be expressed by creating a so-called cost function E (a sum-of-squares error function):

$$E = \frac{1}{2}\sum_{k}(\mathbf{z}_k(\mathbf{w},\mathbf{x}) - \mathbf{z}_{t,m})^2 \tag{5.10}$$

where $\mathbf{z}_k(\mathbf{w},\mathbf{x})$ the network output depending on the weights $\mathbf{w}$ and the input $\mathbf{x}$ and $\mathbf{z}_{t,m}$ the training values and m runs over the set of training inputs. To avoid large numbers for the weights, a regularisation E_w term is usually added to the cost function:

$$E_w = \beta\sum_{i,j} w_{i,j}^2 \tag{5.11}$$

The mathematical task is now to find the minimum of the cost function, i.e. $\nabla E = 0$, which leads to the evaluation of derivatives of the cost function with respect to the weights. Several ways exist to achieve this for a feed-forward network, the most popular are the back-propagation and a quasi-Newton method.

In the back-propagation method we take advantage of the propagation of information in the output direction, i.e. the way that each node takes a linear combination of nodes of the previous layers as input. This allows us to use the chain rule to evaluate the partial derivatives of E with respect to the weights w_{ij}:

$$\frac{\partial E^m}{\partial w_{ij}} = \frac{\partial E^m}{\partial u_i}\frac{\partial u_i}{\partial w_{ij}} \tag{5.12}$$

for a particular training pattern m, for each node i and its weight w_{ij} which connects to the node j in the previous layer. Here, we have considered the cost function for one training set pattern only. The contribution of the whole training set is evaluated by adding the individual outcomes:

$$\frac{\partial E}{\partial w_{ij}} = \sum_{m}\frac{\partial E^m}{\partial w_{ij}} \tag{5.13}$$

Because u_i is a linear combination of outputs from the previous layer, we can propagate backwards using the chain rule. For a sigmoid activation function of form $g(x) = \frac{1}{1+\exp(-x)}$ with $g'(x) = g(x)(1-g(x))$, the complete formula reads:

$$\frac{\partial E}{\partial w_{ij}} = u_i^{(k-1)} - u_j^k(1-u_j^k)\delta_j \tag{5.14}$$

where $\delta_j = z_j - z_{t,j}$ for the output layer and

$$\delta_j = \sum_k w_{jk} u_k (1 - u_k) \delta_k \tag{5.15}$$

for hidden nodes where k sums over the nodes in the previous layer.

The weights are updated in the direction of the greatest decrease, i.e. in direction of $-\nabla E$, so the weights in our next iteration are:

$$w_{ij}^{(k+1)} = w_{ij}^{(k)} - \eta \frac{\partial E}{\partial w_{ij}^{(k)}} \tag{5.16}$$

where η is the so-called learning rate parameter. If too small, convergence can be very slow, if too big, oscillations about a local minimum can occur and the training process might not converge. Usually, η is chosen to decrease steadily to counteract both problems. The process stops either after a defined number of iterations or when a sufficiently small value of the cost function is obtained. As always when looking for extrema with the help of gradients, we find local minima and maxima and not global ones. This disadvantage can be counteracted by training the network several times, called a committee, each time starting with a different set of random values for the weights. The choice is then either to use the best-performing trained network, or to calculate some average. This process could in principle be used to generate a low-resolution probability distribution $P(z)$.

Another method for minimising the non-linear cost function and updating the weights is a quasi-Newton method where a local quadratic approximation is used (e.g. Bishop, 1995; Lahav et al., 1996). The cost function with respect to the weights is approximated using a 2nd order Taylor expansion:

$$E(w) \approx E(w_0) + (w - w_0) \nabla E(w_0) + \frac{1}{2}(w - w_0) \cdot \mathbf{H} \cdot (w - w_0) \tag{5.17}$$

where $\mathbf{H}$ is the Hessian matrix with elements $\partial E_{ij}/(\partial w_i \partial w_j)$. In a standard Newton method, the Hessian (and the inverse of it) is then computed from which the weight vector for a next iteration is calculated. This is repeated until some pre-defined error is achieved. The calculation of the Hessian and its inversion in each iteration is computationally expensive, $O(NW^3)$, where N the number of training objects and W the

number of weights. So-called quasi-Newton methods have been devised to circumvent this. In those methods, the inverse Hessian is approximated directly using only information from the first derivatives, reducing the number of computing steps necessary for each iteration to $O(NW^2)$.

The cost function does not consider noise on the input values. Those errors are propagated through the network and set a lower limit on the overall error for each output value. The Jacobian matrix $J_{ij} = \partial z_i / \partial x_j$ allows us to estimate the contributions of the input error:

$$\sigma_z^2 = \sum_i \frac{\partial z}{\partial x_i} \sigma_{x_i}^2 \tag{5.18}$$

summed over all training objects and z is a vector for more than one output value. Next to the variance due to noisy input values, a network variance is considered when using a committee due to different initial values for the weights which usually results in different local minima. The contribution of the network error is usually small; Oyaizu (2008) find it to be $\sim 1\%$ of the overall error in their evaluation of the errors on photo-z in both their test catalogues (simulated for DES and a SDSS sample). Both errors are then combined in quadrature to give an error on the output value.

Networks, as discussed so far, that undergo a training during which they are presented with target information are called supervised. Unsupervised networks use a learning process without target information. They are often used to find clustering in the input data or create a visual representation of the data. Some attempts have been made recently to employ unsupervised networks to estimate photo-z. Geach (2012) have used a subset with $z_{spec} < 1$ of the COSMOS DR1 catalogue, having complete photometry, resulting in 7651 objects, to estimate photo-z and to establish the performance of their SOM code. Using 12 available photometric bands, a committee of 10 networks and 382,500 iterations per network, they achieve $\sigma(\triangle z) = 0.03$, a very competitive value out to $z = 1$. Way & Klose (2012) show that SOMs are well able to compete with other empirical methods; they achieve a similar performance as Geach (2012) using the SDSS LRG catalogue and the PHAT0 synthetic catalogue.

The main advantage of using ANNs over template fitting methods, lies in the fact

that they do not use any prior assumptions about the outcomes, true of most empirical methods. Some bias is unavoidable though if the training set is not representative of the sample we would like to test. The learning process is tightly linked to the training set values and large, unquantifiable errors can be made when extrapolating outside of the training domain. ANNs deal very well with noise in the data if a validation set is used to avoid an over-training and if uncertainties in the inputs are known, its effects can be quantified via the Jacobian.

Its advantage over other empirical methods, for example polynomial fits, is that the cost function decreases quickly, as $O(1/N)$, by increasing the number N of hidden nodes, irrespective of the number of variables and is hence well suited to deal with a high number of variables.

Another advantage of ANNs is their adaptability: the dimension of the input vector can be increased and additional inputs can be introduced easily. In the estimation of photo-z for example, we can add additional photometry or define an additional galaxy class as output (if provided in the training set).

5.2.2.2 ANNz

`ANNz` is an artificial neural network that was created at Cambridge University by Collister & Lahav (2004), mainly for the estimation of photo-z[5]. It is a feed-forward, multi-layer network with a sigmoid activation function, see fig. 5.2. It uses a quasi-Newton algorithm for the minimisation, see section 5.2.2.1. As a supervised learning network it is presented with a training set where the true redshift (spectroscopic redhift) of each training object is known.

During the training of the network, and for the evaluation if true outcome values are available, a bias and the rms are reported.

$$bias = \langle \mathbf{z}_t - \mathbf{z}(\mathbf{w}) \rangle \qquad \text{and} \qquad rms = \sqrt{\frac{1}{N} \sum_m (\mathbf{z}_t - \mathbf{z}(\mathbf{w}))^2} \tag{5.19}$$

The bias and the rms for each iteration during the training process are evaluated on a

[5] `ANNz` is publicly available from http://www.homepages.ucl.ac.uk/ ucapola/annz.html

set different to the training set, the so-called validation set, to avoid over-training.

Collister & Lahav (2004) achieved a performance of $\sigma \approx 0.02$ with SDSS data for a representative training set. A training set consisting of 15,000 objects and a validation set consisting of 5,000 objects, with photometry in the SDSS bands *ugriz* and spectroscopic redshift were used to evaluate 10,000 objects. The spectroscopic redshift of the evaluation set were know as well which allowed the calculation of the standard deviation in the differences between the estimated photo-z and the spec-z. A comparison with the popular `hyperz`[6], a template fitting method, showed that if the training set is well chosen, `ANNz` performs better, the 1σ scatter of the codes being 0.029 and 0.070 for `ANNz` and `hyperz` respectively. Abdalla et al. (2011) have used 1.5 million galaxies from the Luminous Red Galaxy (LRG) catalogue with photometric information on the SDSS *ugriz* bands, 13,000 with spec-z out to 0.8, to evaluate the performances of 6 different, publicly available, redshift codes. LRGs have usually a well defined 4000Å break and photo-z are hence less uncertain, the main contamination coming from M-type stars, estimated to be around 5%. For this sample, `ANNz` performed very well, better that most other codes, especially in the intermediate redshift range $0.4 < z_{spsec} < 0.7$ where the training set is most complete. The performance of template fitting methods (including 2 that use Bayseian priors), depend very much on the specific template set used, but is usually slightly better at high redshifts, here $z_{spec} > 0.7$.

Regarding the simulated catalogue PHAT0 of Hildebrandt et al. (2010), `ANNz` performance is very competitive with one of the lowest outlier rate, bias and scatter, using the training set of 170,000 objects with $0 < z < 4$ (but few $z > 1.5$) and 10,000 photo-z estimated. The performance on the real catalogue PHAT1 is markedly worse, still with an acceptable bias compared to the other codes, but with a high scatter and the highest outlier rate. This is expected though with a training set comprising only about 500 objects drawn randomly from the set of ∼2000 objects with spec-z. The impact of the `ANNz` training size on its performance, using simulated catalogues, has been investigated by Firth et al. (2003), depending on the redshift range. For lower redshifts,

[6] `hyperz` is available for download at http://webast.ast.obs-mip.fr/hyperz/

$z < 0.5$, smaller training sizes of a few hundreds do give reasonable results for the rms in the scatter (see their fig.5), assuming that the redshift distribution of the training set is complete. For higher redshifts the number of training objects needs to increase considerably to achieve the same performance. Although the PHAT1 catalogue draws on GOODS data with a high rate of spectroscopic data (at the time), the catalogue is not complete out to the redshifts considered and 500 training objects are hardly enough for such a wide redshift range.

5.3 Photometric redshifts of the VIKING-HATLAS sample

The sub-mm wavebands benefit from negative k-correction with the effect that objects can be detected at least out to $z \gtrsim 5$ in the 870 μm band (Blain & Longair, 1993; Chapin et al., 2011). Selecting sources at 250 μm reduces the effectiveness of the negative k-correction, but models still predict a significant fraction of the SPIRE sources to reside at $z > 1$ (e.g. Amblard et al., 2010; Lapi et al., 2011).

A significant fraction of our VIKING counterparts ($\sim 28\%$) have spectroscopic redshift from the GAMA and SDSS redshift surveys. For the remainder, we will obtain photometric redshifts by combining the near-infrared photometry with optical photometric information from the SDSS survey. Objects with spectroscopic redshift from the GAMA survey are then employed as a training set to estimate the photometric redshifts using neural networks, see below.

SDSS matches are found for $\sim 68\%$ of the VIKING candidates within $2''$ by performing a simple nearest neighbour match. The remainder of the VIKING objects are too faint to be detected in the SDSS survey. For near-complete visible detections we have to wait for the VST KIDS survey[7], which will observe the VIKING areas down to 24.8, 25.4, 25.2 and 24.2 (10σ, AB) in u', g', r', i' bands respectively, thus giving detections in at least r', i' bands for nearly all VIKING objects.

[7] PI Konrad Kuiken at Leiden University

With a search radius of 2″ we are unlikely to identify a wrong SDSS counterpart. Using the surface density of the SDSS catalogue employed for the optical matching by Smith et al. (2011), we estimate around 2% (170 objects) of our subsample of reliable VIKING matches to have a wrong SDSS identification within 2″.

For photometric redshifts, we use a neural network method in which the photometry of objects with available spectroscopic redshifts provides the sample to train a network. Once trained, the network is then used to obtain photometric redshifts from the photometry of objects without reliable redshift information. The photometry in the different bands employed can differ, for instance we are using SDSS modelmags and VIKING Vega aperture magnitudes. In contrast, a template fitting method where the photometry is compared to the expected photometry from a class of different (empirical and/or theoretical) SEDs (Spectral Energy Distribution), needs to use very carefully calibrated photometry in all bands. The software used to obtain the photometric redshifts is `ANNz` (Collister & Lahav, 2004), a publicly available product, see section 5.2.2.2. We train a committee of 3 networks for each possible photometric band combination, recommended to minimise the network variance. The output of `ANNz` is the photometric redshift for each object together with a redshift error estimate which takes the photometric errors in each band into account.

We use 30,697 objects with photometry from SDSS and VIKING and spectroscopic redshifts from GAMA in our training set. The median spectroscopic redshift of the GAMA sample is $\tilde{z}_{spec} = 0.211$. The median redshift of the VIKING counterparts is expected to be higher and the training set should reflect this. Currently, there are no deeper spectroscopic surveys available that overlap with the VIKING area. There are though some deeper spectroscopic redshifts from surveys that are within the UKIDSS LAS [8] area (Hewett et al., 2006; Lawrence et al., 2007). Therefore, we undertake a comparison of WFCAM and VISTA photometry, to be able to use deeper photometric

[8] UKIDSS LAS is carried out with the UKIRT WFCAM, and images an area of $\sim 2500\,\mathrm{deg}^2$ in the *YJHK* filters to a depth K=18.4

information from the zCOSMOS[9] (Lilly et al., 2007) and DEEP2[10] (Davis et al., 2003) surveys. We match VIKING objects in a 4 deg^2 area in the H-ATLAS SDP field to objects in the UKIDSS LAS and obtain the mean and standard error for the difference in magnitudes (apermag3) in each of the bands *YJHK*. We are then able to use the LAS photometry for these samples by subtracting this mean from the LAS magnitudes and adding the standard error of the difference in quadrature to the photometric error. This allows us to use the deeper photometry and spectroscopic redshifts of zCosmos (1530 objects) and DEEP2 (238 objects), which overlap with the UKIDSS LAS survey (but not with VIKING), as a training set.

Adding all our subsamples together, we obtain an overall training catalogue with 32,465 spectroscopic redshifts. We then compile a photometric catalogue for all VIKING candidate matches with *ugriz* photometry (modelmags) and *YJHK* photometry (aperture magnitudes), where present. We attempt photometric redshifts where we have at least 2 infrared bands with good photometry.

Using the deeper spectroscopic redshifts from zCOSMOS and DEEP2 forces us to exclude the VIKING *Z* band in the training catalogue. Investigating how this influences our photometric redshifts, we create a second training catalogue, this time using just the GAMA subset (95% of the first training catalogue), so that we can include the VIKING *Z* band. The scatter in the differences between photometric and spectroscopic redshifts for objects with a spectroscopic redshift is slightly lower for this second training set, but this is to be expected because we compare only the lower redshift end. Assuming that the inclusion of deeper redshifts into the training set reflects the true VIKING redshift distribution better, we adopt the photometric redshifts from our first training catalogue, the GAMA-zCOSMOS-DEEP2 training set.

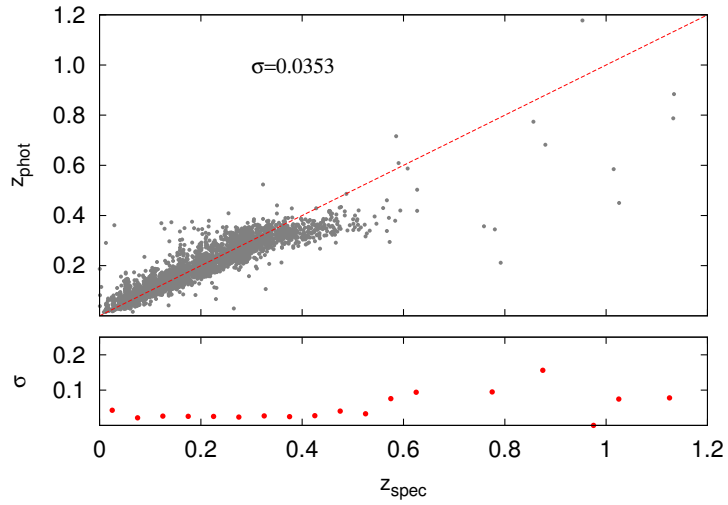

Figure 5.4: — Upper panel: photometric vs. spectroscopic redshift for 3147 reliable VIKING counterparts with spectroscopic redshift from either GAMA or SDSS. Lower panel: scatter of the difference $|z_{spec} - z_{phot}|$ for the same 3147 objects in redshift bins of $\delta z = 0.05$.

5.3.1 Photometric redshift distribution

We have measured the photometric redshifts for all of our 11,294 reliable VIKING counterparts, 8750 of which have SDSS matches within 2", as described in section 4. Spectroscopic redshifts exist for 3147 of the reliable VIKING counterparts which allows us to evaluate the accuracy of the photometric redshifts, see Fig. 5.4. The spectroscopic redshifts are taken from either the GAMA or the SDSS redshift survey. Where a redshift exists in both surveys for a VIKING object, we have used the GAMA redshift (quality flag $Q \geq 3$ only). Excluding 31 confirmed QSOs with $z > 1$, the scatter of the difference between our photometric redshifts and the spectroscopic redshifts is $\sigma = 0.0353$. This reduces to $\sigma = 0.0259$ for the normalised redshift distribution $\triangle z/(1 + z_{spec})$.

Also visible from Fig. 5.4 is the tendency for the photometric redshift to underesti-

[9] zCOSMOS is a redshift survey carried out on the ESO VLT with the VIMOS spectrograph on the COSMOS field

[10] DEEP2 is a redshift survey carried out with the Keck telescopes with a pre-selected redshift range of $0.75 - 1.4$.

mate the redshift at higher values of z; for $z > 0.3$, the bias amounts to -0.0889. The systematic underestimation is also found when comparing spectroscopic redshifts with the photometric redshifts from the H-ATLAS Phase 1 catalogue which used optical and near-infrared photometry from SDSS and UKIDSS-LAS, see Smith et al. (2011). They have employed a similar training set which suggest that we face an issue with the representativeness of our training set. The reason for the bias seems less likely to be a lack of spectroscopic redshifts at $z > 0.3$ but could rather be related to a difference in the colour distribution of galaxies in the training set and our VIKING galaxies. Clearly, more work is needed to investigate the reasons for the bias at $z > 0.3$ and, crucially, to assemble a more representative training set which is outside the scope of this thesis.

The redshift differences $z_{phot} - z_{spec}$ of the 31 confirmed QSOs with $z > 1$ are considerably worse, as the training set includes few high-z QSOs and also the near power-law spectra of QSOs means that QSO photo-z estimates are much worse than for galaxies.

Currently, we cannot estimate the accuracy of the photo-z of VIKING counterparts with just near-infrared photometry due to the lack of spectroscopic redshifts. In general, they have higher photo-z, as can be seen from Fig. 5.5.

Certainly, we are missing more reliable identifications at the higher redshift end than at lower redshifts. The lower panel in Fig. 5.6 shows a comparison of the expected redshift distribution, $real(z_{phot})$ of the VIKING counterparts to the redshift distribution of our reliable counterparts ($R > 0.8$). The expected distribution $real(z_{phot})$ can be calculated in a similar way as the magnitude distributions: from the $total(z_{phot})$, the photometric redshift distribution of the VIKING objects within our search radius of $10''$ and the background distribution $n(z_{phot})$, both shown in the upper panel of Fig. 5.6. Table 5.1 shows the fraction of reliable to expected counterparts per redshift bin, i.e. the completeness of our photometric redshift sample.

Dunlop et al. (2010) have calculated very accurate photometric redshifts for counterparts to 20 bright BLAST sources, using a wide range of deep multi-wavelength data in the GOODS-North field. BLAST used a proto-type SPIRE camera and the BLAST

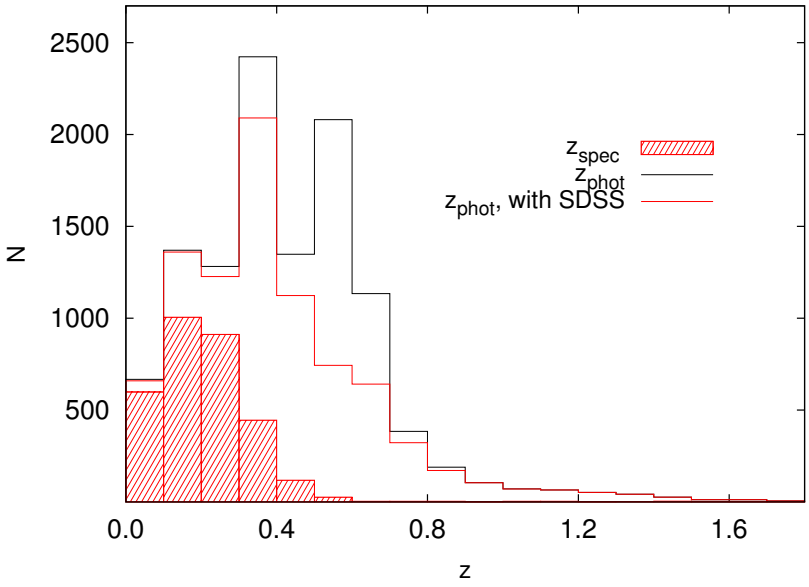

Figure 5.5: — Redshift distributions for the reliable VIKING matches. The filled boxes represent the spectroscopic redshifts for 3147 of the 11,294 reliable VIKING matches with either GAMA or SDSS spectroscopic redshift with a median redshift of $\tilde{z} = 0.199$. The excess peak of all photo-z at $z \sim 0.5$ (black histogram) is formed of redshifts to VIKING objects without optical photometry.

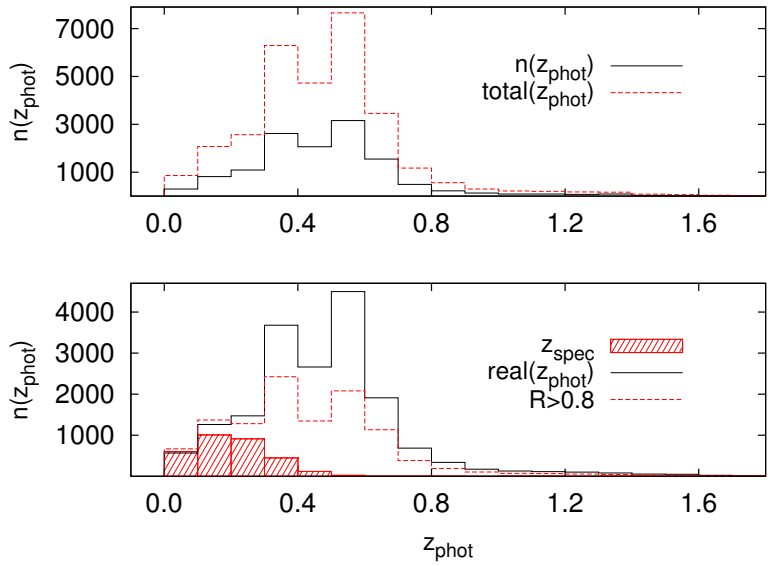

Figure 5.6: — Upper panel: the dashed red histogram shows the photometric redshift distribution of VIKING background objects, the black line represents the photometric redshift distribution of all VIKING objects within our search radius ($total(z_{phot})$). Lower panel: the expected photometric redshift distribution of the true VIKING counterparts ($real(z_{phot})$, black line), calculated by subtracting the background from $total(z_{phot})$. The filled histogram represents spectroscopic redshifts and the red dashed histogram is the distribution for our reliable counterparts.

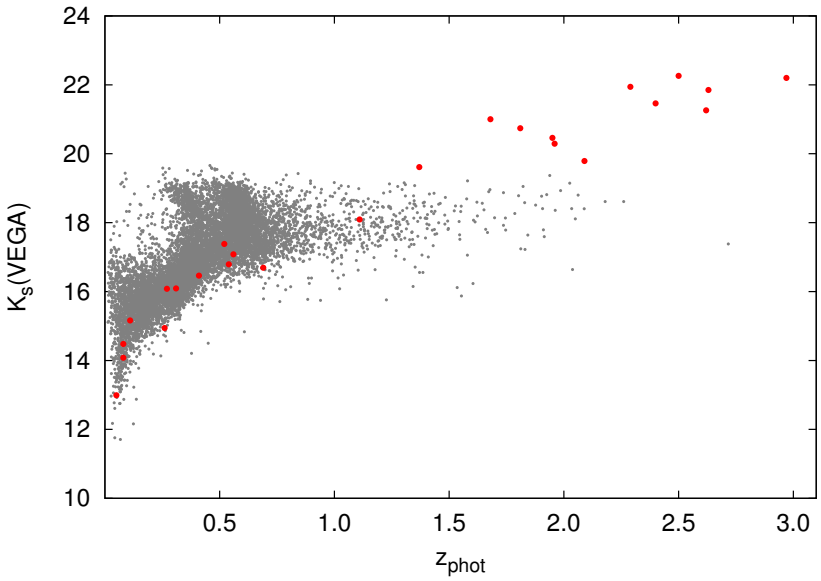

Figure 5.7: — K_s magnitudes (Vega) versus photometric redshift. Grey dots: our reliable VIKING counterparts. Red points: BLAST sources of Dunlop et al. (2010). This suggests that we are fairly complete out to $z \sim 1$.

sources were selected down to 36mJy in 250 μm. We compare our reliable sample to their data on a K_s vs z_{phot} plot in Fig. 5.7. This plot suggests that we are fairly complete out to redshift $z \sim 1$ and are missing higher redshift counterparts due to the VIKING survey limit.

Work carried out by Amblard et al. (2010) using SPIRE and PACS colours, suggests that the SPIRE source redshift distribution might be bimodal, formed by a low redshift population of spirals and a high redshift population of starburst galaxies peaking at $z \sim 2$. Dariush et al. (2011) found that most of the H-ATLAS low-z galaxies are comprised of blue/star-forming galaxies with some highly dusty, red spirals. Evidence for this bimodality in the redshift distribution can also be found in Maddox et al. (2010) using the angular correlation function of 250, 350 and 500 μm selected SPIRE sources, and from theoretical models (Lagache et al., 2003; Negrello et al., 2007). Smith et al. (2011) discuss this in more detail in their section 3.3 on the photometric redshift distribution.

Table 5.1: Photometric redshift completeness, calculated from a background subtracted sample of possible counterparts, $real(z_{phot})$. The errors assume that Poisson errors in the *real* distribution are dominant.

z_{phot}	Completeness(%)	σ_{comp}
0.0-0.1	117.8	5.8
0.1-0.2	108.6	3.8
0.2-0.3	87	2.9
0.3-0.4	65.9	1.4
0.4-0.5	50.6	1.3
0.5-0.6	46.3	0.9
0.6-0.7	59.3	1.8
0.7-0.8	56.1	2.7
0.8-0.9	55.8	3.6
0.9-1.0	61	5.6
1.0-1.1	55	5.6

In this work, we find that the large majority of our candidate identifications have $z_{phot} < 1$, as expected from the K_s magnitude limit of the VIKING data. From our value of Q_0, we expect about 27% of the SPIRE sources to be too faint to be detected in VIKING and hence very likely to be at higher redshifts, see section 4.3.2. Taking into account the possible underestimation of our photometric redshifts at $z > 0.3$, we find that $\sim 2\%$ of the H-ATLAS 250 μm sources with a reliable counterpart lie at $z > 1$. At least a similar fraction of sources without a reliable match and expected to have a true counterpart in VIKING, should obtain $z > 1$. We hence expect $\gtrsim 30\%$ of our H-ATLAS sources to be found at $z > 1$. We compare this with the redshift distributions found for BLAST sources and for sources detected by SPIRE in the GOODS-North field.

Dunlop et al. (2010) and Chapin et al. (2011), using 250 μm BLAST sources, both find that $\sim 50\%$ of their sources lie at $z > 1$ from a variety of photometric redshifts, even though the shapes of the distributions differ, with Dunlop et al. (2010) seeing a more pronounced bi-modality and Chapin et al. (2011) a greater tail beyond

$z = 2$. This comprises a significantly higher fraction of high redshift sources than in this work. Dye et al. (2009) find $\sim 30\%$ of their BLAST sources within a deep field to be at $z > 1$, fully consistent with our fraction. Having used different selection criteria for their BLAST sources, either signal-to-noise cut-offs or flux limits in any of the 250, 350 or 500 μm BLAST bands, leads to different sub-samples that are difficult to compare. In addition, the methods to obtain photometric redshifts and to identify optical/mid-infrared counterparts vary. It is difficult to disentangle the different approaches, but there is still very broad agreement in the conclusion that we see two different populations, one which, at lower redshifts, we find in VIKING counterparts, and the other, at higher redshifts, the fraction of which we can imply and which is consistent with at least some of the BLAST findings.

A similar picture emerges from the HerMES project (Oliver et al., 2010) so far. Eales et al. (2010) and Elbaz et al. (2010) use deep imaging in small areas ($< 0.1\,\mathrm{deg}^2$) observed by SPIRE and with excellent multi-wavelength data available, as well as spectroscopic and photometric redshifts. Both groups use a 250 μm selected sample and assume a 24 μm detection. With a high fraction of spectroscopic redshifts ($> 65\%$), Elbaz et al. (2010) find $35 - 40\%$ of their sources lie at $z > 1$ (deduced from their fig. 2), consistent with our findings, whereas Eales et al. (2010) discover close to 50% in this redshift range.

5.3.2 Photometric redshift comparison

In this section we compare our results with the redshifts supplied with the H-ATLAS G09 Phase 1 source catalogue and derived from the optical identifications. As in section 4.4, we concentrate on the reliable counterparts. Due to the facts that we match with SDSS to obtain our photometry and that `ANNz` is used in both cases, it is no surprise that the photometric redshift distributions of the reliable counterparts are broadly similar, see Fig. 5.8. We obtain a slightly higher median redshift of $\tilde{z} = 0.396$ compared to the median of $\tilde{z} = 0.326$ of the photometric redshifts supplied with the Phase 1 catalogue, partly due to a higher number of redshifts $z_{phot} > 1$. Of the 309

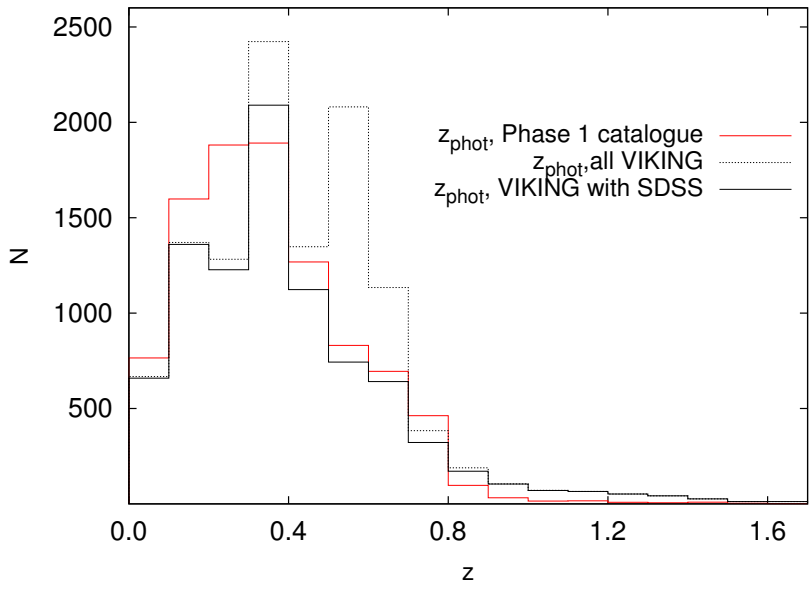

Figure 5.8: — Comparison of the photometric redshift distributions obtained in this work (VIKING) and supplied with the Phase 1 catalogue. The red line shows the latter, 9583 photometric redshifts with a median of $\tilde{z} = 0.326$. The black dashed line shows the former, 11,294 photometric redshifts with a median of $\tilde{z} = 0.396$. The black line represents photometric redshifts of the 8748 VIKING objects with SDSS counterparts.

SPIRE sources with VIKING reliable counterparts and $z_{phot} > 1$, 76 are reliable, have photometric redshifts and are matched to the same object in the optical catalogue. The photometric redshifts of those 76 objects differ by an average of 0.46. This large difference could be explained by incomplete photometric information from UKIDSS LAS used to compile the photometric redshifts in the optical catalogue. Indeed, nearly half (35) of the 76 objects have only 1 or 2 bands in the near-infrared available from LAS. This shows the advantage of the deeper VIKING data. Much better results should be achieved once we have optical photometry from the VST KIDS survey to combine with VIKING.

Chapter 6

The Evolution of the sub-mm Luminosity Function

> "Things exist either because they have recently come into existence or because they have qualities that made them unlikely to be destroyed in the past." *Richard Dawkins, The Blind Watchmaker*

The galaxy luminosity function (LF) in itself is a straight forward concept: it represents the number of galaxies for a given luminosity, or in a certain luminosity range for the differential LF. Binning the galaxies into redshift intervals can then help to describe how populations of galaxies evolved. Details of the LF and how it can be constructed from redshift surveys or from simulations are provided in section 6.1. This section also includes a short discussion of past and current research related to the LF at sub-mm wavelengths.

Any theory of galaxy formation and evolution has to be able to explain the observed LF, locally and at higher redshifts. The LF plays therefore a fundamental role in constraining evolutionary models of galaxy formation, merger rates and star formation rates. A short overview of evolutionary models is given in section 6.3.

Section 6.4.1 explains our data selection and method used to construct the H-ATLAS sub-mm LF, using the reliable counterparts to the VISTA VIKING survey as

described in chapter 4 and section 6.4.2 presents the results.

6.1 Construction of the LF

The differential LF ϕ of a galaxy sample is defined as the number of objects per comoving volume per unit luminosity and is linked to the space density of galaxies as follows:

$$dN = \phi(L) dL\, dV \tag{6.1}$$

where dN the number of galaxies observed between luminosities L and $L + dL$ in the comoving volume dV. If redshift information is available, the LF is defined by:

$$\phi(L, z) = \frac{d^2 N}{dV\, dL}(L, z) \tag{6.2}$$

where dN as above, but now at redshift z. The galaxy samples are also often divided into different types, most basically into red, early-type and blue, late-type sets. This is a special case of a bivariate LF that uses luminosity and an additional parameter as independent input variables. Chapin et al. (2009) have estimated the local far-infrared LF $\phi(L, C)$ where $C = \log(S_{60} - S_{100})$ intended as a benchmark/calibration for the then upcoming *Herschel* mission. Other additional variables include the radius (of nearby galaxies, see Choloniewski, 1985) and the surface brightness (Ball et al., 2006).

The following sections will explain the parametric and non-parametric methods of LF construction as well as the motivation for our method selection.

6.1.1 Parametric method

Parametric models assume an analytical form of the LF. The most popular analytical expression is the Schechter function (Schechter, 1976):

$$\phi(L) dL = \phi^* (L/L^*)^\alpha \exp(-L/L^*) d(L/L^*) \tag{6.3}$$

where $\phi(L)dL$ the number of galaxies per unit co-moving volume in the luminosity interval L to $L + dL$ and ϕ^*, α and L^* are parameters that have to be determined from

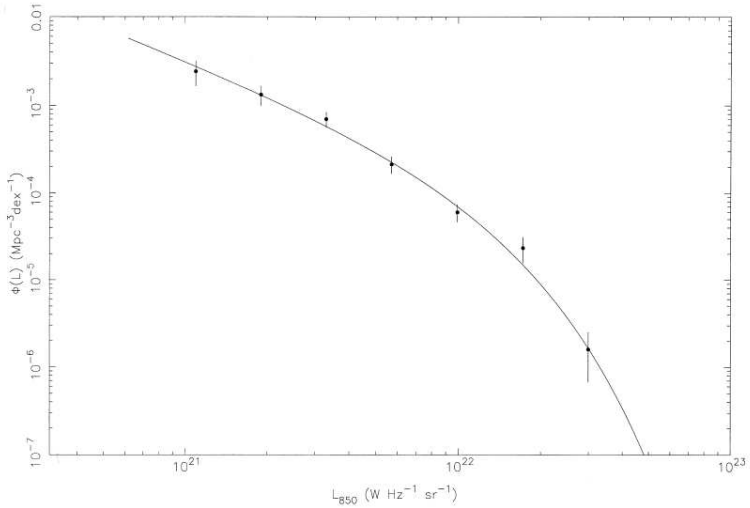

Figure 6.1: — The 850 μm LF of 104 galaxies from the SCUBA Local Universe Galaxy Survey (SLUGS). The black line shows the best-fit Schechter function with parameters α=-2.18 and $L^* = 8.3 \times 10^{21}$ W Hz^{-1} sr^{-1}.

the data. The characteristics of this form are the power law at the faint end (with slope α), exponential cut-off at the bright end and the characteristic luminosity L^* at the turn-over point, or 'knee', between power-law and exponential form. For an example see figure 6.1, showing one of the first observed sub-mm LF at 850 μm from the SCUBA Local Universe Galaxy Survey (SLUGS).

A modified Schechter function has been found to represent the 60 μm IRAS galaxy LF well (Saunders et al., 1990):

$$\phi(L) = C \left(\frac{L}{L^*}\right)^{1-\alpha} \exp\left(-\frac{1}{2\sigma^2}\log_{10}^2\left(1+\frac{L}{L^*}\right)\right) \tag{6.4}$$

which still shows a power-law behaviour at the faint end, but behaves like a Gaussian in $\log L$ for $L \gg L^*$.

Serjeant & Harrison (2005) find that a double power law fits their predicted far-infrared LF better than a Schechter function:

$$\phi(L) = \phi^*/[(L/L^*)^\beta + (L/L^*)^\gamma] \tag{6.5}$$

Those and other analytical expressions (for a more comprehensive list see Johnston

(2011)) are used by the parametric methods to estimate the LF. The best known is the maximum likelihood estimator (MLE), first introduced into observational cosmology by Sandage et al. (1979) and often referred to as the STY79 estimator when used with a Schechter function. The probability $P(L, z)$ that a galaxy has luminosity L or higher at redshift z is:

$$P(L, z) = \frac{\int_L^\infty \phi(L')\rho(z)dL'}{\int_{-\infty}^\infty \phi(L')\rho(z)dL'} \tag{6.6}$$

and hence for the differential probability $p(L, z)$:

$$p(L, z) = \frac{\partial P(L, z)}{\partial L} = \frac{\phi(L)}{\int_{-\infty}^\infty \phi(L')dL'} \tag{6.7}$$

assuming, as is usual in constructing the LF, that the spatial distribution (here $\rho(z)$) and the luminosities are independent of each other. If we assume a parametric form for ϕ, depending only on a set of parameters Θ_j, then it follows that the likelihood $l_i = p(L_i, z|\Theta)$ depends on those parameters only. The likelihood function for our observed luminosities is then $\mathcal{L} = \prod l_i$. By maximising $\mathcal{L}$, we obtain the best set of parameters Θ that could have led to our observed luminosities, thus estimating the LF in its parametric form. The likelihood function is often expressed in logarithmic terms as $\ln \mathcal{L} = \sum \ln l_i$.

Since $\rho(z)$ cancels out in eq. 6.6, the MLE method does not provide a normalisation, the ϕ^* in case of the Schechter function. A standard procedure to calculate the normalisation uses the average number density divided by the integral of the LF (see Willmer et al. (2006) for more detail). The MLE method is generally used in conjunction with a non-parametric method (e.g. the $1/V_{max}$ method, see next section), to provide a visual check of the fit and to obtain error estimates for the parameters by fitting the parametric expression to the data points.

6.1.2 Non-parametric models

If we assume a homogeneous distribution of galaxies in space and that our sample is complete out to the magnitude (flux) limit considered, then we can naively express the

LF as:

$$\phi = \frac{N}{V} \tag{6.8}$$

where N the number of galaxies with a certain absolute magnitude or luminosity and V the survey volume. This is the average galaxy density per unit volume observed and has been applied from the early stages of galaxy study starting with Hubble.

The assumption that the sample is complete is usually wrong for flux limited samples because we can observe brighter galaxies to much greater distances. To account for this effect, the accessible volume denoted V_{max} was introduced (e.g. Schmidt, 1968): for each galaxy, it is defined as the comoving volume in which a galaxy with luminosity L can still be detected in the survey. Dividing each of the galaxies by its accessible volume assigns in effect a higher weight to fainter galaxies. The LF is then:

$$\phi = \frac{1}{\Delta L} \sum_i \frac{1}{V_{max,i}} \tag{6.9}$$

in a certain luminosity range and $V_{max,i}$ is given by:

$$V_{max,i} = \int_A \int_{z_{min}}^{min(z_{max}, z(L_i, S_{min}))} \frac{dV}{dz}\, dz\, dA \tag{6.10}$$

where $z(L_i, S_{min})$ the maximum redshift a galaxy with luminosity L_i can have and still be observable, dV the comoving volume element and A the survey area.

Felten (1976) generalised this method (called $1/V_{max}$) to allow for galaxies coming from more then one survey with different magnitude limits. Eales (1993) used it to obtain the LF from three different redshift surveys and investigated the evolution of the LF for the first time directly, i.e. by constructing the LF at a number of redshifts.

The $1/V_{max}$ method is still popular today and has been modified further by Page & Carrera (2000) (PC00 hereafter) to overcome bias when binning a flux-limited sample in redshift and luminosity. $\Delta L V_{max}$ in eq. 6.9 can include regions in the $L - V(z)$ plane that are not observable. This is especially an issue for galaxies near the flux limit, i.e. in the lower luminosity bins for each redshift slice. PC00 introduce a new estimator that includes only surveyed regions from the $L - V(z)$ plane. The expected number of

objects found in $\Delta L \Delta V(\Delta z)$ is:

$$\langle N \rangle = \int_{L_{min}}^{L_{max}} \int_{z_{min}}^{z_{max}(L)} \phi(L,z) \frac{dV}{dz}\, dz\, dL \tag{6.11}$$

where L_{min} and L_{max} are the lower and upper limits of the luminosity bin, z_{min} the lower limit of the redshift bin and $z_{max}(L)$ the highest redshift possible for an object with luminosity L and still be in the redshift bin. If we assume that $\phi(L,z)$ changes little over the L-z bin, we have:

$$\langle N \rangle \approx \phi(L,z) \int_{L_{min}}^{L_{max}} \int_{z_{min}}^{z_{max}(L)} \frac{dV}{dz}\, dz\, dL \tag{6.12}$$

and hence:

$$\phi_{est} = \frac{N}{\int_{L_{min}}^{L_{max}} \int_{z_{min}}^{z_{max}(L)} \frac{dV}{dz}\, dz\, dL} \tag{6.13}$$

where N is now the actual number of objects found in the $L-z$ bin and ϕ_{est} is the binned estimate of the LF. The denominator in eq. 6.13 is the accessible comoving volume averaged over the luminosities in this bin. Both estimators, the $1/V_{max}$ and the PC00, perform similarly for $L-z$ bins that are far from the flux-limit of the survey. However, the $1/V_{max}$ LF estimator shows a downturn in the lowest luminosity bin in each redshift slice, i.e. close to the flux-limit, due to an overestimate of the accessible volume. This has been demonstrated nicely by Dunne et al. (2011) comparing both estimators when calculating the LF for H-ATLAS sources in the SDP field, see fig. 6.2.

The statistical errors on the PC00 estimator in the literature are usually either purely Poisson (e.g. Eales et al., 2009; Simpson et al., 2012) or Gaussian (e.g. Dunne et al., 2011; Jiang et al., 2008). The PC00 estimator does not depend on the measured luminosities of the sources (only to sort the sources into luminosity bins) which is an advantage for sub-mm sources where the luminosities are very uncertain due to flux-boosting from source confusion; for this reason, we are using the PC00 estimator for the calculation of the H-ATLAS sub-mm LF using sources with reliable counterparts in VIKING, see section 6.4.2.

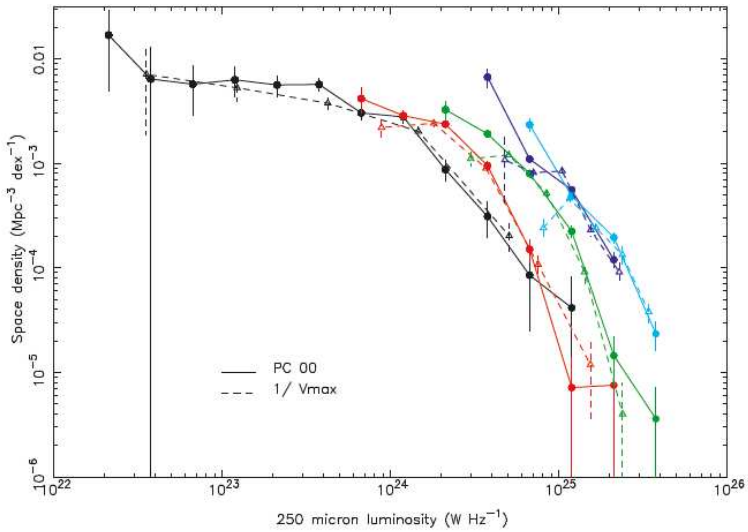

Figure 6.2: — The H-ATLAS SDP sub-mm LF of Dunne et al. (2011) out to redshift $z = 0.5$. Dots connected by dashed (solid) lines represent the LF using the $1/V_{max}$ (PC00) method respectively. The redshift is colour-coded as follows: black $0 < z < 0.1$, red $0.1 < z < 0.2$, green $0.2 < z < 0.3$, blue $0.3 < z < 0.4$, cyan $0.4 < z < 0.5$

6.1.3 Corrections for incompleteness

Observational limitations lead to a range of issues concerning the completeness of our galaxy sample. The $1/V_{max}$ method and subsequent improvements, deal with the flux limit of a survey by using the accessible volume. More corrections to the sub-mm catalogue are often necessary due to the source extraction method. These can be constrained by creating maps from a simulated input galaxy catalogue and then recovering the input sources. The differences in the input and recovered catalogue indicate the corrections necessary to the catalogue number densities. Rigby et al. (2011) (see also section 3.1.1.1) have used this method to create correction tables for the flux and surface density of the H-ATLAS SDP sources. In section 6.4.1 we have used these tables to calculate correction factors for our galaxy sample.

Another hurdle to the construction of the sub-mm LF is incompleteness due to missing counterparts, because in the sub-mm we are relying on identifications in other wavelengths to obtain redshifts. Two factors are to consider: the incompleteness of the

matching catalogue itself and the incompleteness introduced by the matching method.

The matching catalogue, in our case the VIKING GAMA 09 catalogue as described in section 2.1.1.1, is incomplete due to its own flux/magnitude limit. Without reliable correction factors from the literature, one can construct some correction from expected densities towards the magnitude limit. Dunne et al. (2011) have used the SDSS catalogue to fit a linear function to the logarithmic number counts in the range $19 < r < 21.5$ and extrapolated to fainter magnitudes, up to the magnitude limit of $r = 22.4$. The difference in expected and observed number counts is then used to calculate the correction factor. We are using a similar approach when correcting for the magnitude limit in our VIKING K_s sample. Sometimes it is enough to restrict the upper redshift used to avoid any missing counterparts, as shown in Eales et al. (2009); when matching BLAST sources to mid-infrared and/or radio objects, restricting the redshift to $z < 1$ should ensure that no counterparts are lost due to flux limits. Dye et al. (2010) have used yet a different approach: they plot the optical r band fluxes against the SPIRE 250 μm fluxes in different redshift bins. Because they find a clear correlation in each redshift bin, they can use the relation to estimate a 250 μm flux cut-off for each bin where they miss <5% of identifications due to the $r = 22.4$ limit. They then restrict their analysis to SPIRE sources greater than this sub-mm flux cut-off. Both methods have the disadvantage though that sources are lost to the construction of the LF, either because of redshift or flux restrictions.

The matching method used to find counterparts in other wavelengths depends on choices regarding the values of statistic cut-off (e.g. P-value or reliability R) and several other variables (e.g. search radius). Smith et al. (2011) account for the reliability cut-off in the matching of the SDSS catalogue to the H-ATLAS SDP sources by considering the ratio of reliably identified counterparts to detected counterparts ($Q_0 \times N_{source}$) in different redshift slices (their table 3). We have followed this approach, as outlined in our chapter on photometric redshifts in section 5.3.1 and created a table for the VIKING identifications. This allows us to use the inverse of the incompleteness as a correction factor in the $dz = 0.1$ redshift bins. The incompleteness table of Smith et al.

(2011) has also been used by Dunne et al. (2011) to account for the incompleteness in the optical identification method. Dye et al. (2010) relied on the search radius cut-off to calculate an incompleteness correction for the ID method. Defining r_{80} for each optical counterpart as the radius at which it would have achieved a reliability of 80%, the correction factor is then calculated as the inverse of the fraction that would have been identified within the smaller of r_{80} and the 10 arcsec search radius. The resulting correction factors c_i are in the range of $1 < c_i < 1.2$ in Dye et al. (2010), rather small, and even smaller when we apply this to our VIKING counterparts, with a maximum correction of $c_i \approx 1.1$. Hence, we have ignored this correction for our sample. Assuming Gaussian errors, the search radius of 10 arcsec employed by us and for the sample Dye et al. (2010) are using, includes the vast majority of the possible optical/NIR counterparts to the sub-mm sources, 99.996%. Also, the radius r_{80} can only be calculated if it is assumed that there is only one candidate to each sub-mm source; not true for the majority of sources.

Using a frequentist method (e.g. P-value), Eales et al. (2009) account for missed mid-infrared and radio counterparts (being outside the search radius) to BLAST sources by considering the maximum radius $r_{cut,i}$ at which a specific counterpart i could have been found. The correction factor is then the ratio of the probability of finding a counterpart at all (which would be Q_0 in our method) to the probability of finding a counterpart out to $r_{cut,i}$. Again, assuming Gaussian errors, our search radius is big enough to include nearly all possible counterparts and we do not correct for the possibility that we miss a counterpart in this way.

6.2 Review of the sub-mm LF

The sub-mm LF before the Submillimetre Common User Bolometer Array (SCUBA,Holland et al., 1999) camera on the James Clerk Maxwell Telescope has usually been estimated using data from shorter wavelengths. The sub-mm luminosities are then deduced from assuming model SEDs. It has been found with the *Herschel* data, that the total

infrared luminosities L_{FIR}, defined as the luminosity integrated over 8-1000 μm, are tightly correlated to total luminosities extrapolated from 24 μm data out to redshift $z \simeq 1.5$, but that above this redshift, the total luminosities from 24 μm are in general overestimated; Elbaz et al. (2010) find factors of 2-3 and Rodighiero et al. (2010) a factor of ~ 1.8.

For the mid- to far-infrared probed by IRAS, the LFs are in general not well fitted with a Schechter function. Lawrence et al. (1986) find a two power-law a good match to the 60 μm data, Rieke & Lebofsky (1986) also construct a two power-law fit for their infrared LF (integrated 25 μm-200 μm), as a Schechter function does not account for the higher number of brighter galaxies observed. Using a MLE, Saunders et al. (1990) found that a Schechter function does not fit the IRAS 60 μm and their integrated LF very well and that a modified Schechter (see eq. 6.4) matches the observed data more adequately.

With the advent of SCUBA, statistically viable sub-mm selected samples were available for the first time. The SCUBA Local Universe Galaxy survey (SLUGS) observed 104 galaxies selected at 60 μm from the IRAS Bright Galaxy Sample in the JCMT long (850 μm) and short (450 μm) wavelength bands. The resulting sub-mm LF (Dunne et al., 2000) can be seen in fig. 6.1. Fitting a single temperature SED (modified Blackbody, see section 6.4.1) to the IRAS 60- and 100 μm and the SCUBA 850 μm fluxes, they find a mean temperature of 35.6±4.9K and an emissivity index of $\beta = 1.3 \pm 0.2$ (see section 6.4.1). Both variables are highly degenerate, and increasing the emissivity index will lead to colder dust temperatures. In contrast to the IRAS LF discussed above, they find that a Schechter function fits the observed sub-mm LF well.

Serjeant & Harrison (2005) predicted the 850 μm LF by extrapolating from the IRAS Point Source Catalogue (PSC) 60 and 100 μm fluxes, using a colour-luminosity relation found by Dunne et al. (2000); the resulting 850 μm LF is in good agreement with the LF from the observed data of Dunne et al. (2000), even though they find that a two power-law fits the data better than a Schechter function. They also predict the 250 μm LF, see fig. 6.3, relevant for Herschel.

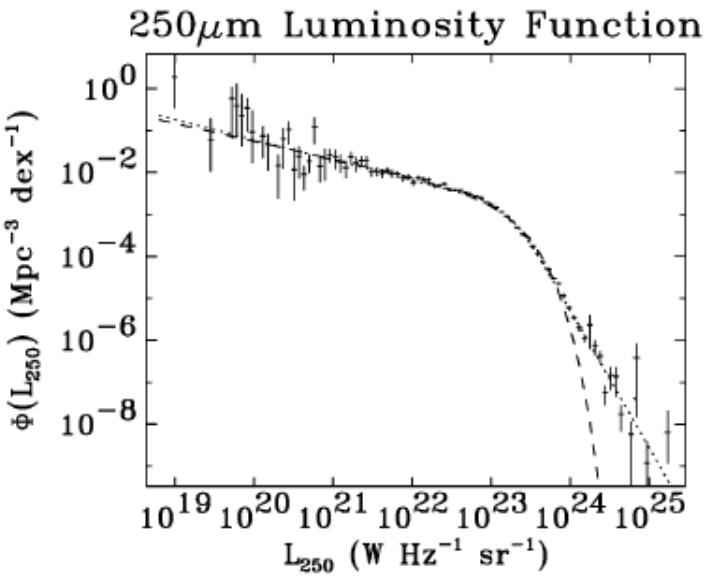

Figure 6.3: — The projected local Herschel 250 μm LF from IRAS PSC galaxies of Serjeant & Harrison (2005). The 250 μm luminosities are extrapolated from observed 60 and 100 μm fluxes. The data is better fitted with a double power law (dotted line) than a Schechter function (dashed line).

The first observed 250 μm LF could be measured with BLAST fluxes. Eales et al. (2009) construct the 250 μm LF in five different redshift slices out to redshift $z = 1.0$. The radio and/or mid-infrared counterparts have been selected using the P-value method (Dye et al., 2009 and section 4.1). They obtain spectroscopic redshifts for those counterparts and allow for incompleteness due to missing counterparts and counterparts without redshift (see section 6.1.3). Using the PC00 method, see section 6.1.2, they measure the sub-mm LF in the 250, 350 and 500 μm bands. This is the first time, the galaxy sub-mm LF has been directly measured in those wavelength bands. The resulting 250 μm LF can be seen in fig. 6.4. They have also extrapolated the LF from IRAS PCSz 60 and 100 μm fluxes, as Serjeant & Harrison (2005), but using a relationship between the ratios 60/100 and 60/850 from Vlahakis et al. (2005) to obtain 850 μm values. This allowed them to fit a single temperature model SED (modified Blackbody) to obtain the luminosities at other wavelengths. The extrapolated 250 μm can be seen in fig. 6.4 as the thick dashed line and is in good agreement with the observed data in the redshift range $0 < z < 0.2$, showing that predictions from mid-infrared wavelengths are viable. Fig. 6.4 also shows evidence for cosmic evolution, with the space density of more luminous galaxies increasing with cosmic redshift. They do see this effect also in the LF at 350 and 500 μm, implying that it is a solid result. Following the observations of *Herschel* (see chapter 3), the sub-mm LF has been measured from data of the HerMES and the H-ATLAS surveys in the SDP field. Vaccari et al. (2010) construct the local 250, 350, 500 μm and total infrared LF using the Spitzer 24 μm counterparts of the HerMES galaxies and fit the resulting multi-wavelength data to SED templates from Polletta et al. (2007) with the `hyperz` code. Applying the $1/V_{max}$ method (see section 6.1.2), they find that the modified Schechter function of Saunders et al. (1990) is a good fit to the local 250 μm LF function, see fig. 6.5a. They find a slightly higher number of local sub-mm galaxies than predicted from models (see next section) and a slope at the faint end of the LF that is somewhat flatter than had been shown previously, but note that the latter could be caused by the low number of galaxies in the lowest luminosity bin.

Eales et al. (2010) have used the HerMES SDP data to investigate the evolution

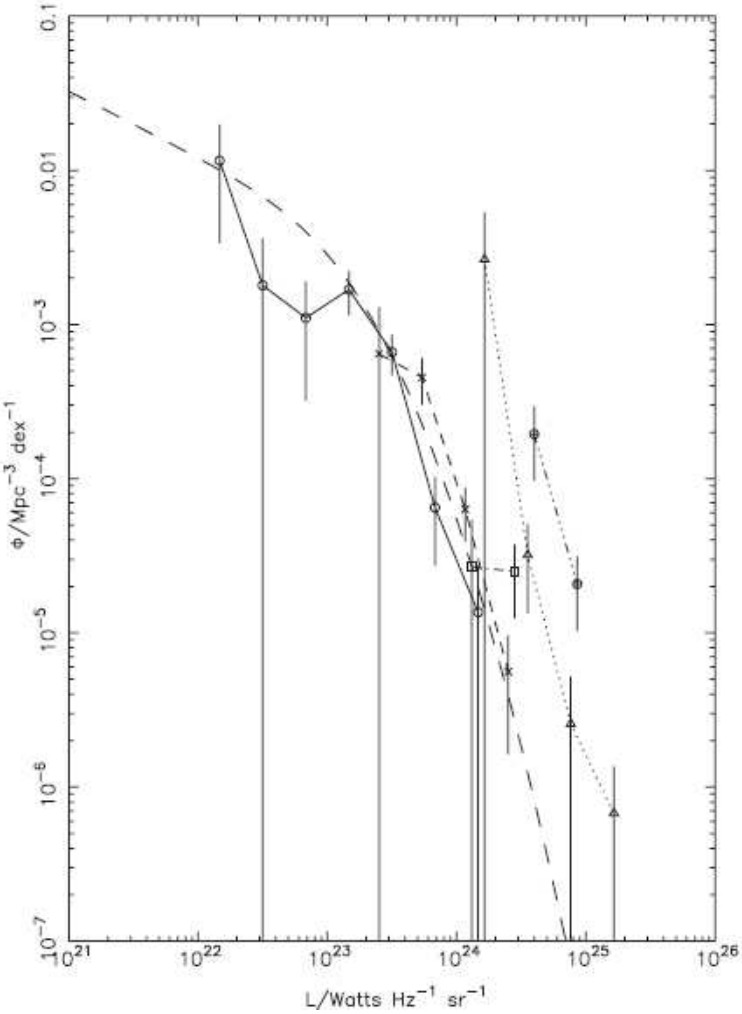

Figure 6.4: — The BLAST 250 μm LF of Eales et al. (2009), uncorrected for flux-boosting. The data is divided into five redshift slices: open circles $0 < z < 0.2$; crosses: $0.2 < z < 0.4$; squares: $0.4 < z < 0.6$; triangles: $0.6 < z < 0.8$; crosses inside circles: $0.8 < z < 1.0$. The thick dashed line represents the extrapolated LF from 60 and 100 μm IRAS PSCz galaxies(Saunders et al., 2000).

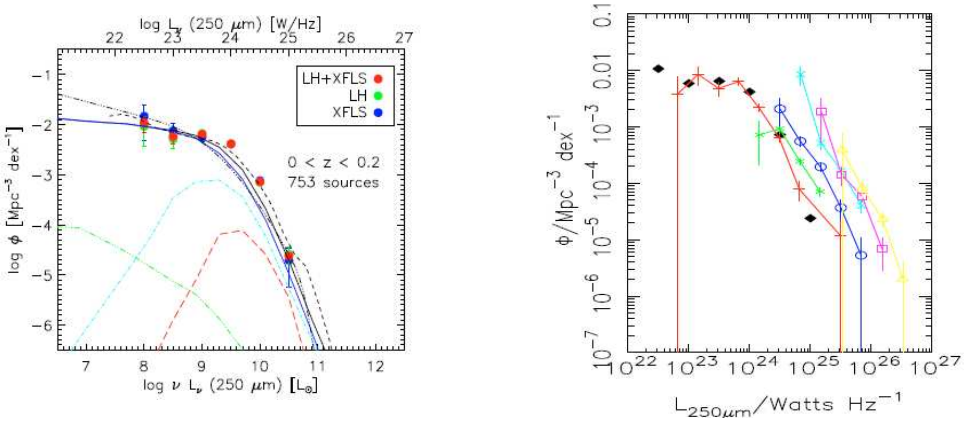

(a) **(b)**

Figure 6.5: **(a)** The HerMES 250 μm local LF of Vaccari et al. (2010). The blue, cyan, red and green lines represent spirals, starburst, high-luminosity starburst and type-1 AGN respectively from the evolutionary model of Franceschini et al. (2010). **(b)** The HerMES 250 μm LF of Eales et al. (2010) in redshift slices of $dz = 0.4$ and out to $z = 2.0$. Strong evolution can be seen out to $z \sim 1.0$.

of the sub-mm LF out to redshift $z = 2.0$ and find evidence for strong evolution out to about $z \simeq 1.0$ and only weak evolution beyond this redshift, see fig. 6.5b, both being consistent with models. They have used the average SED (modified Blackbody) found for the BLAST galaxies by Dye et al. (2009), with a temperature of 26K and an emissivity index of $\beta = 1.5$, and the method of PC00 to construct the 250 μm LF.

Dye et al. (2010) undertook an investigation of the 250 μm LF with H-ATLAS SDP data from a catalogue with optical counterparts (Smith et al., 2011); the survey being shallower than HerMES, only redshifts out to $z = 0.5$ were included. They fitted a modified Blackbody SED to the data with a fixed emissivity index of $\beta = 1.5$ and found a median temperature of 26 ± 8K (allowing for a temperature in the range 10K $<$ T $<$ 50K), practically the same as the mean BLAST temperature. Also, where available, PACS fluxes were included in the fit. They then construct the LF with the $1/V_{max}$ method, using the galaxy's SED-specific k-correction and luminosity (in contrast to the PC00 method). They consider two sources of incompleteness (see

section 6.1.3): due to the r-band magnitude limit and due to the matching method, here the reliability cut of 80%. The resulting 250 μm LF is shown in fig. 6.7; it shows strong evolution over the redshift range considered with the comoving space density increasing with redshift. In section 6.4.2, we will compare it to our sub-mm LF of the much larger Phase 1 data and constructed with the use of VIKING counterparts instead of the optical counterparts.

The most recent sub-mm LF to present here is from Dunne et al. (2011). Similar to Dye et al. (2010), they have used the H-ATLAS SDP catalogue, but investigate the dust evolution. They correct for three different sources of incompleteness: sub-mm flux, optical magnitude limit and matching process, see section 6.1.3. To evaluate the PC00 method they are using to determine the dust mass, they first construct the LF using three different methods: the PC00, the $1/V_{max}$ and a modified version of the PC00 (hereafter mPC00). The PC00 and the $1/V_{max}$ methods are discussed in section 6.1.2. For the mPC00, they use now the individual k-corrections from the galaxy's fitted SED, instead of a k-correction corresponding to the average SED. They are still using the whole luminosity range within a luminosity bin instead of the galaxy's luminosity; this would amount to a return to the $1/V_{max}$ method. The mPC00 can hence be considered a middle path between the PC00 and the $1/V_{max}$ method. They show that one of the advantages of the PC00 is still conserved in the mPC00: the lack of a down-turn in the first luminosity bins as seen in the $1/V_{max}$ method. Fig. 6.6 shows their resulting 250 μm LF, using mPC00. They also see significant evolution, but somewhat less than Dye et al. (2010) in the highest redshift bins. We compare our LF to their results in section 6.4.2.

From considering the sub-mm LF in the literature, we have seen that there is strong evidence for evolution in the comoving space density out to redshift of at least $z = 0.5$ (from H-ATLAS) and even $z = 1.0$ (from HerMES and BLAST). The next section will examine how this is explained/predicted by some evolutionary galaxy formation models.

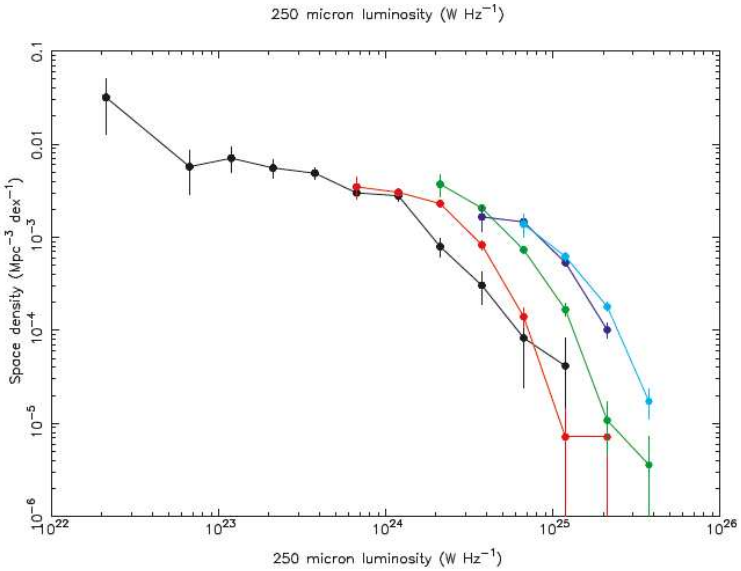

Figure 6.6: — The H-ATLAS 250 μm LF of Dunne et al. (2011) using the modified version of PC00. The colour-coding is as in fig. 6.2

.

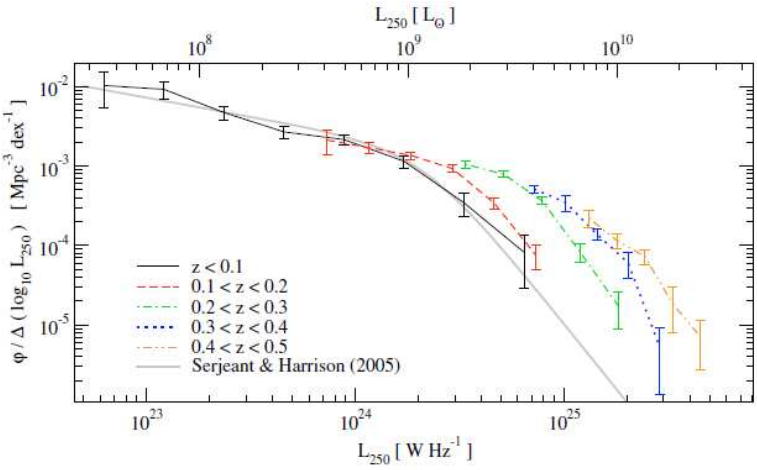

Figure 6.7: — The H-ATLAS 250 μm LF of Dye et al. (2010) using the $1/V_{max}$ method.

6.3 Models of galaxy evolution

With the advent of COBE and SCUBA, it became clear that galaxy formation and evolution models based on UV and optical could not explain the number counts and luminosity densities in the far-infrared and sub-mm range. Bruzual (1990) predicted the infrared background from evolutionary models of normal galaxies which was 1-2 orders of magnitude too low compared to the CIB as observed by COBE. Mazzei et al. (1994) model for the first time the spectrum of elliptical galaxies from the UV to the far-infrared and can show that those galaxies might go through a very dust-obscured phase early in their development, assuming a large initial star formation rate, emphasizing the important role for observations in the longer wavelength range. Franceschini (1997) devised a new population of high redshift dusty starbursts to complement the normal galaxies and AGN supposed to make up the bulk of the far-infrared emission which allows him to account for the CIB. Franceschini (1997) were able to reproduce the CIB by including a dusty phase in the formation of elliptical galaxies. Guiderdoni et al. (1998) recommend the addition of sub-mm into the modelling of galaxy properties when successfully reproducing optical properties from adding reprocessing of starlight by dust.

Rowan-Robinson (2001) adds a cirrus component and leaves out the normal galaxy template. His contributions to the CIB come from two different classes of starbursts (M82 and Arp220 like), an AGN dust torus and the cirrus. Starting from a parameterisation of the star formation history and the assumption of pure luminosity evolution, he deduces the detailed shape of each SED. He finds that to be consistent with infrared number counts and the CIB; the star formation rate has to be flat between redshifts $z = 1$ to 3. He predicted that 70% of the *Herschel* 250 μm sources are below redshift $z = 1$ (using a cosmological model of $\Omega_M = 1$ though), which is in agreement with our findings, see section 5.3.1.

Lagache et al. (2003) modelled the IR/sub-mm evolution with two SED templates only: normal galaxy and starburst, the latter dominating the high luminosity part of

the IR LF and the former the low luminosity end. They considered for the first time the fluctuations seen in the CIB, and account for the CIB and recent sub-mm observations with SCUBA and MAMBO by requiring strong evolution from the present day to $z = 1$ which stays constant thereafter until $z = 5$.

Negrello et al. (2007) used four template SEDs: protospheroidal, starburst, normal and radio, starting from physical models of Granato et al. (2004) and the Zotti et al. (2005) radio model. Their aim was to predict number counts of strongly lensed sources for upcoming sub-mm observations. Their prediction of around 80 strongly lensed galaxies in the 550 deg^2 H-ATLAS survey turns out to be probably underestimated, having found already 5 of those systems in the SDP data (14.4 deg^2) (Negrello et al., 2010).

Franceschini et al. (2010) use a wide range of FIR/sub-mm data from recent observations (24 to 1200 μm) to construct their phenomenological model of galaxy evolution. The contribution of their four SEDs (normal spiral, 2 starbursts, AGN) can be seen in fig. 6.5a where we show the local LF of Vaccari et al. (2010). They predict $10^{2.625} \sim 421\text{deg}^{-2}$ sources at 250 μm, 10% within the actual H-ATLAS sources found in the SDP.

The Lagache et al. (2003), Negrello et al. (2007) and Franceschini et al. (2010) models are often used to compare to LFs constructed directly from observational data, as well as the LF of Serjeant & Harrison (2005) who use relation between 850/60 μm and 60/100 μm found by Dunne et al. (2000).

6.4 The sub-mm LF of the VIKING-HATLAS sample

6.4.1 Method

We are following the methods of PC00 and the modified version as used in Dunne et al. (2011) (hereafter D11, see section 6.1.2 for both) in determining the LF for the H-ATLAS Phase 1 sources in the GAMA9 field with reliable VIKING counterpart (see chapter 4).

The SPIRE fluxes are corrected according to the prescription by Rigby et al. (2011), depending on flux density and S/N. Reliable PACS fluxes at 100 and 160 μm, as used by Dye et al. (2010) and D11 were not available yet for the Phase 1 data at the time of this work (May 2012). We use spectroscopic redshifts where available and reliable (e.g. for GAMA, the quality flag $Q \geq 3$); otherwise we employ our photometric redshifts, see chapter 5. In section 5.3.1 we argue that we should be fairly complete out to $z \simeq 1$ and hence restrict our analysis to the subset of sources with $z \leq 1$ (10,810 galaxies).

The PC00 method requires an average SED and k-correction for its galaxies to calculate the accessible volume. The binning into luminosity bins of width 0.25dex however is done with the luminosities as calculated for each galaxy from the fitting of the SPIRE fluxes. We assume that the dust temperature is mainly the result of a greybody, or modified blackbody, of the form:

$$\nu^{\beta+3}(\exp(h\nu/kT) - 1)^{-1} \tag{6.14}$$

where h the Planck constant, k the Boltzmann constant and β the emissivity index. We use the 3 SPIRE fluxes at 250, 350 and 500 μm to fit the spectrum in eq. 6.14 with fixed[1] $\beta = 1.5$ and within the range $10K < T < 50K$ following Dye et al. (2010). For galaxies, where the dust temperature could not be constrained within the limits ($\sim 10\%$), we adopt the median temperature.

We find a median best-fit dust temperature of 22 ± 7K; this is lower than the median of 26 ± 5K found for sources detected at 250 μm with BLAST (Dye et al., 2009) and 26 ± 8K with SPIRE in the H-ATLAS SDP field (Dye et al., 2010), also with a fixed emissivity index of $\beta = 1.5$. Both studies include shorter wavelength data in the SED fitting: Dye et al. (2009) use Spitzer 70 and 160 μm fluxes and Dye et al. (2010) have PACS fluxes available at 100 and 160 μm for $\sim 10\%$ of their sources. The effect of including PACS data in the SED fitting for H-ATLAS sources is investigated by Smith et al. (2012): the mean isothermal temperature is substantially higher and

[1] Hildebrand (1983) found an emissivity index β of between 1 and 2 for thermal emission at $\lambda = 250\,\mu$m. Dunne et al. (2000) are using $\beta = 1.3$ whereas we adopt here the value of $\beta = 1.5$ used by Dunne et al. (2011); Dye et al. (2009, 2010).

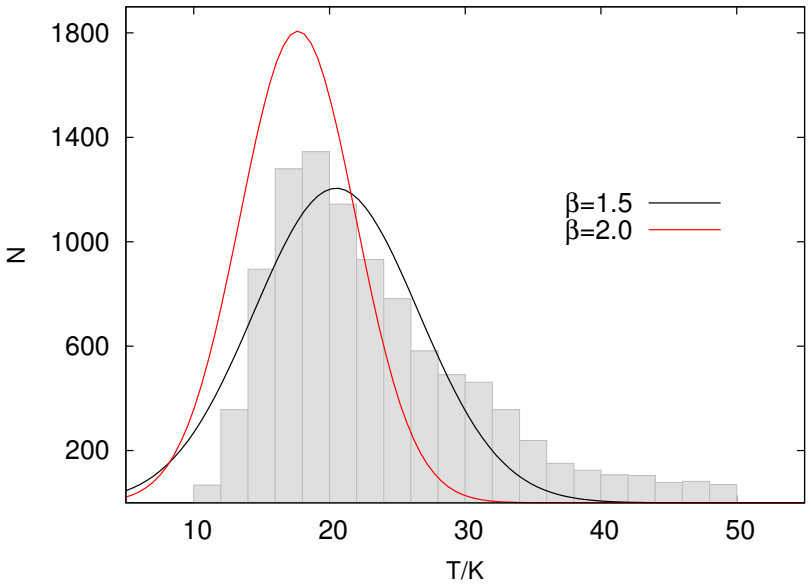

Figure 6.8: — Isothermal dust temperature distribution from the fitting of the 250, 350 and 500 μm fluxes to a greybody spectrum. The black line represents the best Gaussian fit to the histogram. The red line shows the Gaussian fit to the temperature distribution with $\beta = 2.0$.

the uncertainties in the temperatures are larger when using the PACS fluxes (see their Fig.7). This can also be seen in Fig.10 (right) of Dunne et al. (2011), showing the isothermal temperature distribution for objects with and without PACS data. We could hence argue that we obtain lower median dust temperatures than the above studies because we do not include shorter wavelength data. A much lower median dust temperature of 18.7K is also found by Bourne et al. (2012) when fitting H-ATLAS SPIRE fluxes of galaxies without PACS data at redshifts $z < 0.35$ from the three equatorial GAMA fields, using $\beta = 2.0$. Repeating our fitting with $\beta = 2.0$, we find a median temperature of 18.7K, in close agreement, although only 38% of our galaxies lie at $z < 0.35$. We have subsequently run our PC00 LF analysis with both median temperatures, 22K and 26K. For a distribution of the temperatures from our SED fitting, see fig. 6.8.

The D11 method also uses the luminosities from the greybody fitting to bin the data; in contrast to the PC00 method though, the individual k-corrections are applied for each galaxy, obtained from its fitted SED, for the calculation of the accessible volume. The multiplicative k-correction K for the monochromatic luminosity at 250 μm is calculated as:

$$K = \left(\frac{\nu_{obs}}{\nu_{em}}\right)^{\beta+3} \times \frac{e^{h\nu_{em}/kT} - 1}{e^{h\nu_{obs}/kT} - 1} \tag{6.15}$$

where ν_{obs} the observed frequency, corresponding to 250 μm, and ν_{em} the rest-frame frequency, depending on the redshift of the galaxy. The 250 μm luminosity L_{250} in WHz^{-1} is then given by:

$$L_{250} = 4\pi D(z)^2 (1+z) S_{250} K \tag{6.16}$$

where $D(z)$ the comoving distance (see section 5.1.2) and S_{250} the SPIRE flux density at 250 μm. Both methods offer an advantage over the $1/V_{max}$ method where the galaxy's luminosity is also used in the calculation of the comoving volume, introducing a difficult to quantify error due to the uncertainty in luminosity from flux boosting. The relatively large width of the luminosity bins provides less room for error when using the luminosity just for binning.

Table 6.1: The completeness of the VIKING catalogue used for the identifications, as a function of Ks magnitude. C_K represents our correction factor as used in the determination of the LF.

K_s	Completeness	C_K
18.8	0.77	1.31
18.9	0.69	1.45
19.0	0.61	1.63
19.1	0.47	2.14
19.2	0.30	3.33
19.3	0.12	8.19
19.4	0.07	14.73
19.5	0.05	21.61
19.6	0.03	36.59
19.7	0.01	92.11

In addition to the (minimal) corrections C_S made to the SPIRE flux density at 250 μm, we correct for the VISTA VIKING survey limit in K_s and for the redshift incompleteness. For the correction due to the K_s limit, we use a similar method to D11. We fit a linear line to the logarithmic histogram of K_s magnitudes of our VIKING catalogue in the range $16.7 < K_s < 18.7$; the difference between the expected and observed number counts is then used to calculate the completeness, the inverse of which is our correction factor C_K, see table 6.1. We have chosen to extrapolate the number counts from $K_s = 18.8$ as this is the peak of the distribution, expecting that the true numbers would steadily increase, at least to our highest magnitude of $K_s = 19.7$ considered, see fig. 6.9. The redshift correction factor C_z is calculated from table 5.1 as the inverse of the completeness in column two, assuming a 100% redshift completeness out to redshift $z = 0.2$; see section 5.3.1 for the calculation of the redshift completeness. For the PC00 method, see eq. 6.13, the LF in each bin is then calculated as:

$$\phi = \frac{\sum_i C_S C_K C_z}{\int_{L_{min}}^{L_{max}} \int_{z_{min}}^{z_{max}(L)} \frac{dV}{dz} dz dL} \tag{6.17}$$

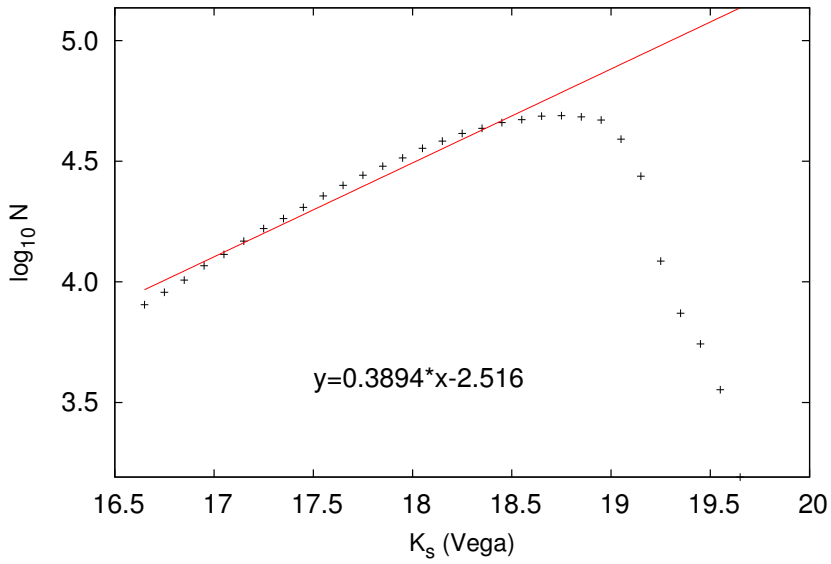

Figure 6.9: — K_s logarithmic number counts of the G09 VIKING galaxy catalogue ($\geq 5\sigma$ in K_s, any J detection, see sections 2.1.1.1 and 2.1.1.2 for more details on the selection criteria). The red line represents the linear fit to the data in the range $16.7 < K_s < 18.7$.

where i runs over all galaxies in the bin. For the D11 method, the only difference is the substitution of the upper limit $z_{max}(L)$ with the upper limit $z_{max,i}$ which now depends on the ith galaxy, due to the application of the galaxy's k-correction:

$$\phi = \sum_i \frac{C_S C_K C_z}{\int_{L_{min}}^{L_{max}} \int_{z_{min}}^{z_{max,i}} \frac{dV}{dz} dz dL} \tag{6.18}$$

6.4.2 Results

Figs. 6.10 and 6.11 are created using the method of PC00 with a median temperature of 22K and 26K respectively in the calculation of the accessible volume. The differences are small, with a good agreement out to $z = 0.4$ (black and red line) and slightly higher space density values for the LF at higher redshifts when using 22K.

Fig. 6.12 is created using the individual k-corrections for the calculation of the accessible volume, i.e. the D11 method. One immediately obvious effect is the downturn seen in the lowest luminosity bins for the redshifts $z > 0.2$. This effect can also be seen

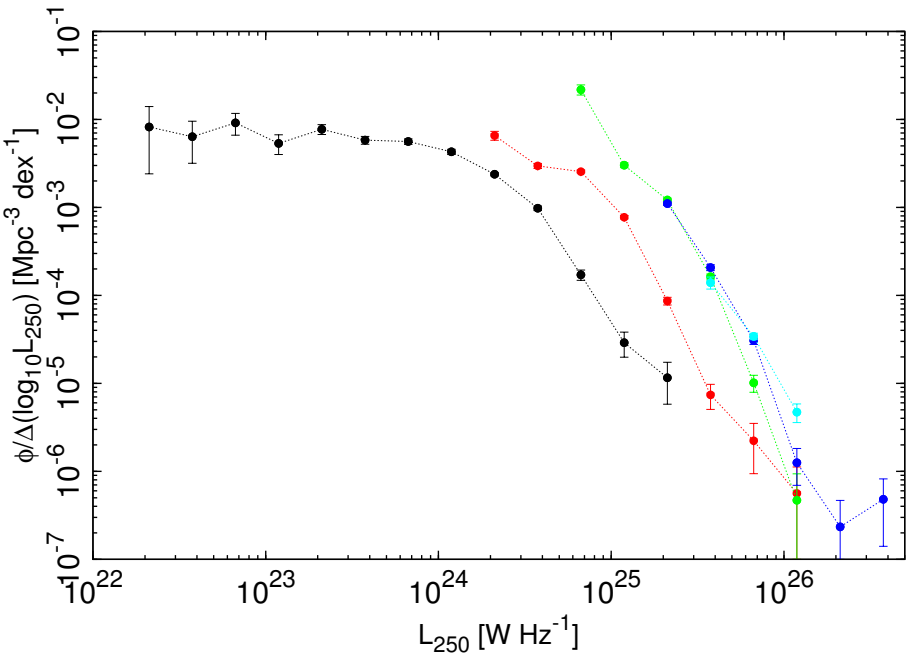

Figure 6.10: — The H-ATLAS 250 μm luminosity function using the PC00 method with a median dust temperature of 22K, as found by our greybody fitting of the three SPIRE fluxes. The key to the colour-coded redshift slices is as follows: $0 < z < 0.2$ black, $0.2 < z < 0.4$ red, $0.4 < z < 0.6$ green, $0.6 < z < 0.8$ blue, $0.8 < z < 1.0$ cyan.

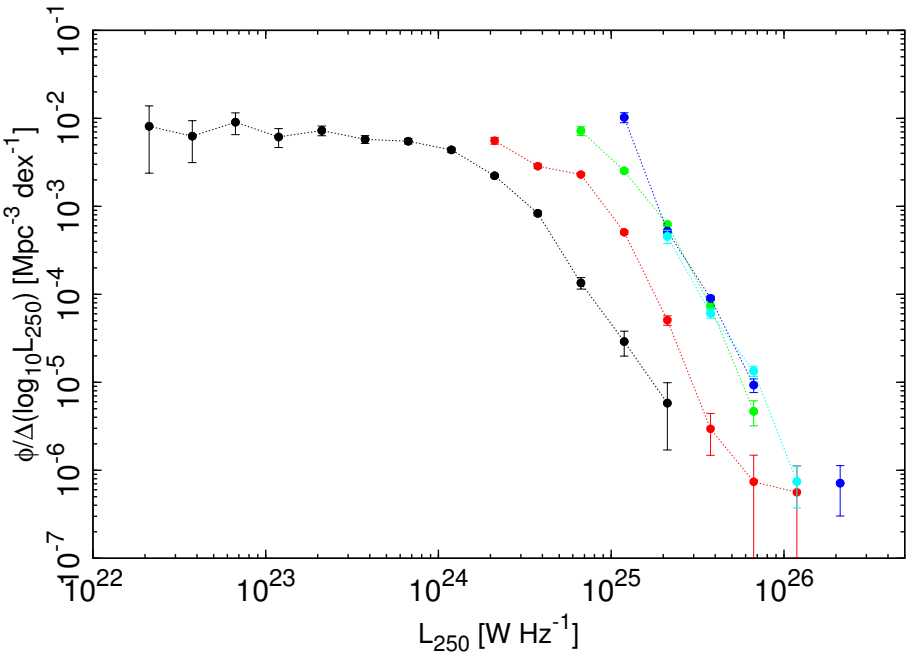

Figure 6.11: — The H-ATLAS 250 μm luminosity function using the PC00 method with a median dust temperature of 26K, as found by Dye et al. (2009, 2010). The key to the colour-coded redshift slices is as in fig. 6.10

in D11, where the PC00, the $1/V_{max}$ and modified PC00 (D11) methods are compared, although the effect is much more pronounced when using the $1/V_{max}$ method. One reason for seeing this downturn can be explained when contemplating the relationship between isothermal dust temperature and luminosity, see eq. 6.14, 6.15 and 6.16 : for a fixed redshift, the k-correction decreases with increasing temperature. Hence for a given redshift range, higher dust temperatures are linked to the lowest luminosities; this is obvious in fig. 6.13 showing the dust temperature vs the luminosity in the colour-coded redshift ranges. The lower k-corrections, as compared to the PC00 method which uses the median dust temperature, are then used in the calculation of the accessible volume with the effect of increasing it; this in turn leads to a lower value of ϕ.

We divide our galaxy sample into "red" ($S_{250}/S_{350} < 1.5$, 5575 galaxies) and "blue" ($S_{250}/S_{350} > 1.5$, 5235 galaxies) and run the analysis on the two samples separately. This shows that the downturn effect is mostly caused by the red galaxies; having lower dust temperatures, they are much more affected by the link between luminosity and temperature within a redshift slice. This is illustrated in fig. 6.13: the black continuous line represents the dividing line between the red galaxies (below) and the blue galaxies (above); the red galaxies show a much more pronounced inverse relationship between temperature and luminosity within each redshift slice.

It is obvious from figs. 6.10 to 6.12 that we find strong evolution of the 250 μm LF out to about redshift $z = 0.6$, and that there is a lack of evolution beyond $z \simeq 0.6$. This is in contrast to Eales et al. (2009) using BLAST data out to $z = 1.0$ and Eales et al. (2010) using HerMES data out to $z = 2.0$. One possible explanation for the weak evolution could be the uncertainty in the photometric redshifts we use. Indeed, both the BLAST and the HerMES studies have a much higher percentage of spectroscopic redshifts at their disposal, $\sim 40\%$ and $\sim 36\%$[2] respectively. In comparison, 28% of the sources in our sample have a spectroscopic redshift. In section 5.3.1 we find that our photometric redshifts suffer from a bias of ~ 0.09 for $z > 0.3$, i.e. we underestimate the

[2]The HerMES percentage of spectroscopic redshifts relates to $z \leq 2$, so the percentage up to $z = 1$ should be even higher.

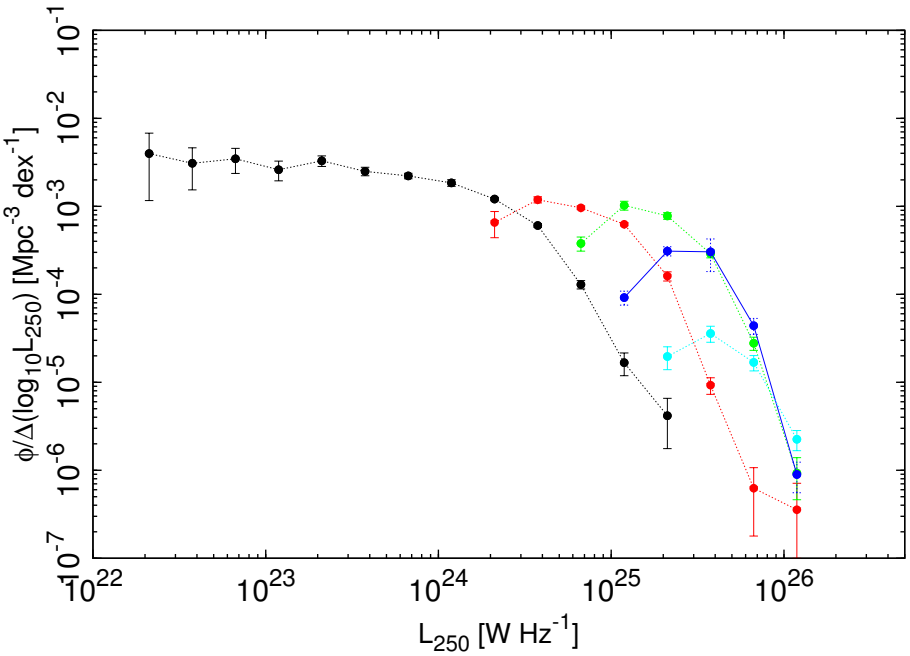

Figure 6.12: — The H-ATLAS 250 μm luminosity function and its evolution using the D11 method. The accessible volume is calculated using the galaxy's own k-correction as obtained from the greybody fitting. The key to the redshift slices is as in fig. 6.10.

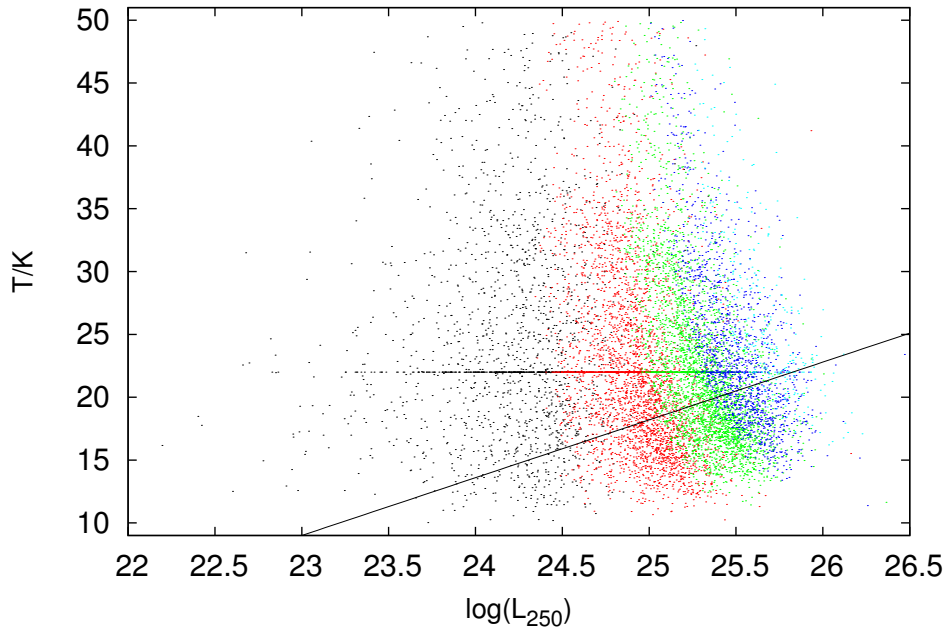

Figure 6.13: — Isothermal dust temperature and luminosity showing no overall correlation. Within the individual redshift slices though, the higher luminosities are reserved for the lowest temperatures. The black line represents the division between the "red" and "blue" galaxies, see text. The horizontal concentration at T=22K arises from the galaxies without acceptable SED fit within the temperature range and which subsequently have been assigned the median temperature of 22K.

photometric redshifts by this amount. We add this bias to all the photometric redshifts $z > 0.3$ used in our sample and run our analysis again using the PC00 method with the temperature median of 22K. The result can be seen in fig. 6.14. We now see a strong evolution out to redshift $z = 0.8$, in much closer agreement to the BLAST and HerMES findings.

The lack of evolution beyond this redshift could still be attributed to an improper correction of the incompleteness in our sample at the fainter K_s magnitude end. One source of uncertainty comes from the choice of K_s range in the fitting of the linear slope to extrapolate the number counts. We run our analysis with two different slopes, one steeper and one flatter, without a significant change in the LF evolution at the high redshift end.

The flux corrections we have applied from Rigby et al. (2011) include a correction for flux-boosting. Eales et al. (2009) have produced two versions for the LF at 250 μm: one without any attempt at correcting for flux-boosting and another which shows the effects of including a correction for flux-boosting (with a method similar to that of Rigby et al., 2011). The latter shows less evolution between the two highest redshift slices, closer to our findings. The inclusion of the correction for flux-boosting affects the faintest sources most, lowering their luminosities. Eales et al. (2010) do not include corrections for flux-boosting as they seem confident that the method to select counterparts (Roseboom et al., 2010), assuming 24 μm detection, deals with this issue. They use a redshift range of $0.8 < z < 1.2$ (see fig. 6.5b) and it is rather difficult to compare to our findings: it could be that the objects with $1.0 < z < 1.2$ in this slice are responsible for the evolution they still see. In summary, we are in broad agreement over the evolution of the 250 μm with prior direct measurements from BLAST and HerMES, even though we find strong evolution to slightly lower redshifts than those studies.

Our estimate of the local luminosity function (LLF, $z < 0.2$) is compared with the findings of Vaccari et al. (2010) (V10, purple triangles) and the predictions of Serjeant & Harrison (2005) (SH05, grey: Schechter, black: double power-law) in figs. 6.15 and 6.16. Our own best-fit Schechter and double power law functions are in red and blue

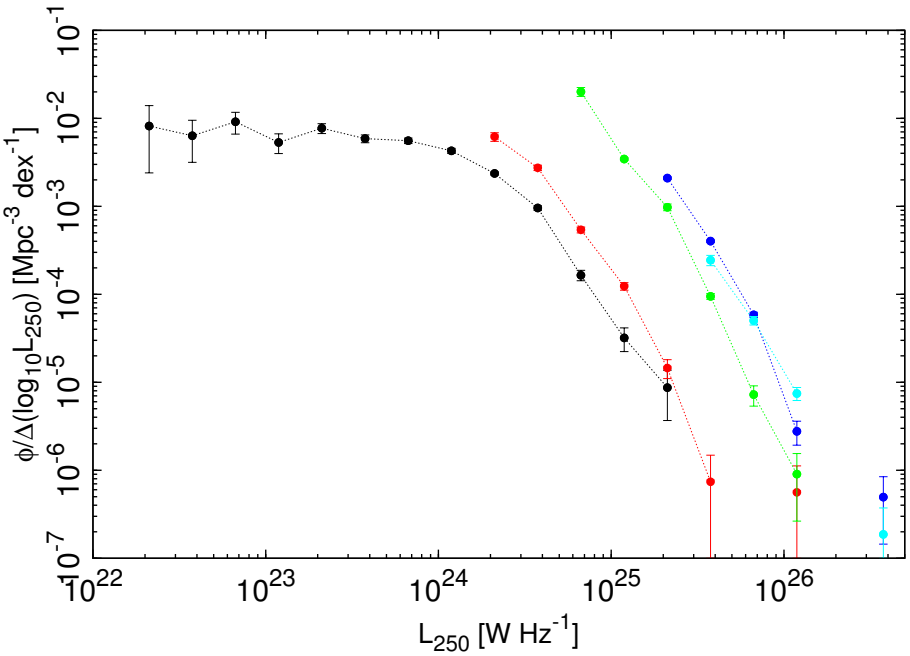

Figure 6.14: — The H-ATLAS 250 μm luminosity function and its evolution using the PC00 method and a median dust temperature of 22K. A bias of 0.09 has been added to photometric redshifts $z > 0.3$. The key to the redshift slices is as in fig. 6.10.

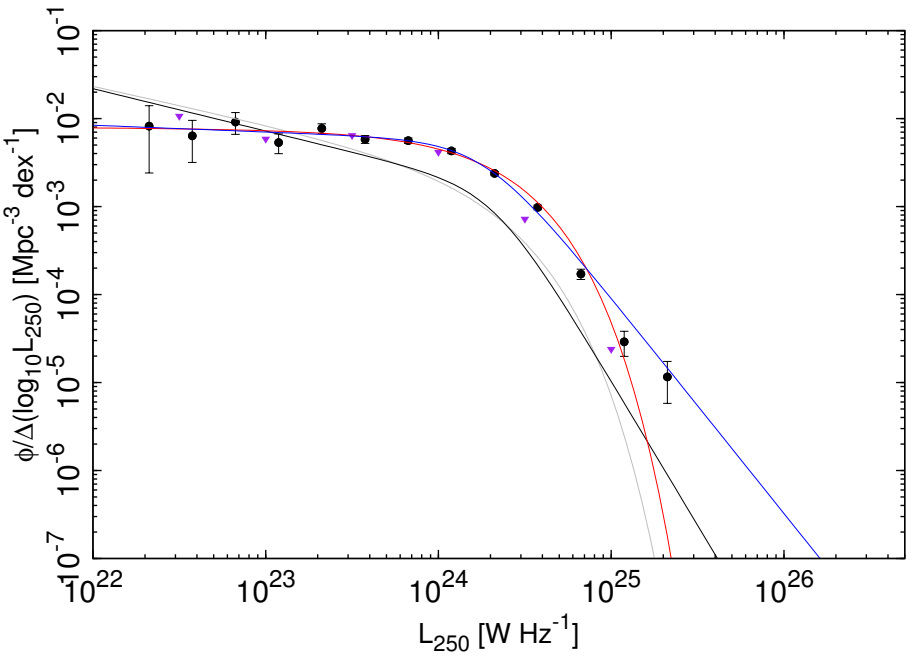

Figure 6.15: — The H-ATLAS 250 μm local luminosity function (LLF, $z < 0.2$) using the PC00 method with a median dust temperature of 22K. The black points are our data, the purple triangle represent the LLF of Vaccari et al. (2010). The grey and black lines represent the best-fit Schechter and double power-law function of Serjeant & Harrison (2005). The red and blue lines represent the best-fit Schechter and double power-law function for our measurements of the LLF.

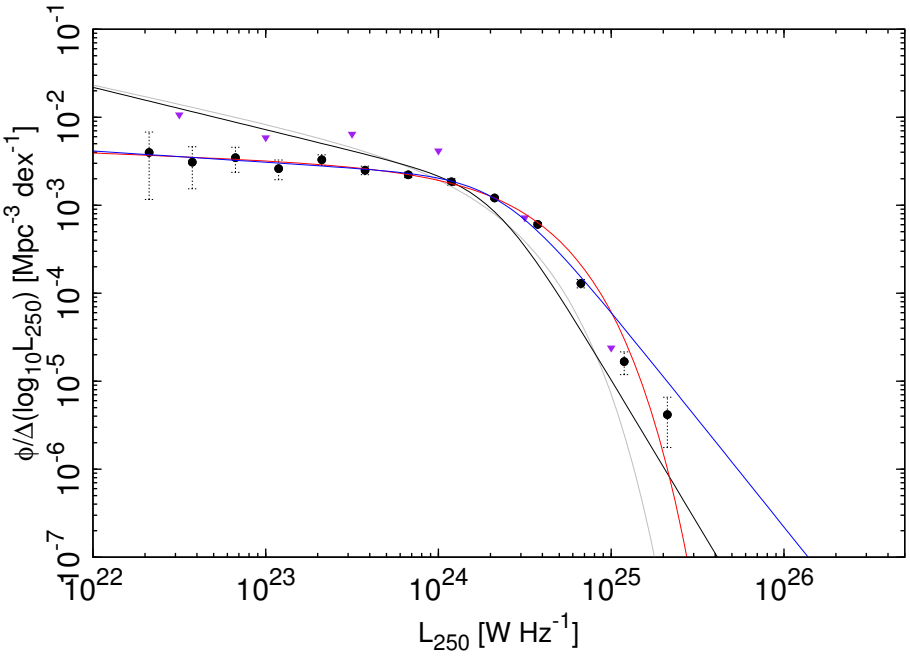

Figure 6.16: — The H-ATLAS 250 μm local luminosity function (LLF, $z < 0.2$) using the D11 method. The key to the colour-coded points and lines is as in fig. 6.15.

Table 6.2: Best-fitting parameters for the 250 μm LF as defined by eq. 6.3 and 6.5. The units are dex^{-1}Mpc^{-3} and WHz^{-1} for $\log_{10}(\phi^*)$ and $\log_{10}(L^*)$ respectively. The β here represents one of the two double power-law indices as in eq. 6.5 and is different from the emissivity index β in eq. 6.14.

	Schechter			Power law			
	$\log_{10}(\phi^*)$	$\log_{10}(L^*)$	α	$\log_{10}(\phi^*)$	$\log_{10}(L^*)$	β	γ
SH05	-2.62	24.29	-0.43	-2.78	24.33	0.481	3.28
PC00 22K	-2.13	24.30	-0.013	-2.25	24.26	0.077	2.45
PC00 22K, photo-z bias	-2.13	24.29	-0.010	-2.25	24.26	0.075	2.45
PC00 26K	-2.28	24.42	-0.072	-2.37	24.36	0.123	2.45
D11	-2.59	24.44	-0.078	-2.69	24.38	0.128	2.45

respectively. Table 6.2 lists the best-fit parameters for the different fittings.

We find excellent agreement between our local LF measurement and the findings of V10 when using the PC00 method with either 22K or 26K (not shown). Employing the D11 method, i.e. using the individual k-corrections for the calculation of the accessible volume, leads generally to lower space densities by about a factor of two. As we have seen in our discussion of the downturn in the lowest luminosity bins for the D11 method, higher temperatures lead to lower k-corrections which in turn lead to higher accessible volumes and lower values for the space density. This effect is amplified in the lowest redshift bin where the higher temperatures are more common. Hence we see the disagreement as compared to our LLF using the PC00 method. V10 have used the $1/V_{max}$ method which should in principal show similar results to the D11 method, but they also employ different SEDs to find the k-corrections, fitting optical to sub-mm spectral templates from the library of Polletta et al. (2007). It is difficult to disentangle the effects of the methods for the calculation of the LLF and the SED fitting. The good agreement is however encouraging.

Comparing our LLF with the predictions of SH05, we find that our LLFs exhibit much flatter slopes at the faint end. Here, the sample size is small though and we could see the effects of incompleteness. On the bright end, our measurements of the space

density are larger than the predictions; here, we might see the effect of the extrapolation from shorter wavelength data used by SH05. Dye et al. (2010) see a similar effect at the bright end, if less pronounced, when comparing their local LF to the predictions of SH05.

Comparing our LF with the results of Dye et al. (2010) (fig. 6.7) and D11 (fig. 6.6), both using the H-ATLAS SDP data, out to redshift $z = 0.5$, we find broad agreement; the different binning in redshift makes a comparison in more detail difficult.

Chapter 7

Star formation rates and dust attenuation in the UV and sub-mm

"The seeker after truth should be humbler than the dust." *Mahatma Gandhi*

The evolution of a galaxy is intrinsically linked to the history of its star formation. Stars form out of gas and dust under the influence of gravity and hence it seems reasonable to estimate a galaxy's current star formation from the amount of gas and/or dust that can be inferred from observations. Indeed this has been the first approach to the estimation of a galaxy's star formation rate (SFR), pioneered by Schmidt (1959) who assumed a power-law for the dependency of the SFR on the gas surface density, usually defined in terms of the SFR surface density $\Sigma_{\rm SFR}$ and the gas density Σ_{gas} as $\Sigma_{\rm SFR} \propto \Sigma_{gas}^{N}$. This so-called Schmidt law has been shown to hold surprisingly well within our Galaxy. Kennicutt (1998) showed that normal disk galaxies and starbursts follow the Schmidt law very well with a power-law index of $N = 1.4 \pm 0.15$, (Kennicutt-Schmidt law).

The observable effects of star formation are usually dominated by the most massive stars in a galaxy. The resulting UV light can hence also be used as an estimator for the

galaxy's SFR (e.g. Buat et al., 2010; Gilbank et al., 2010; Kennicutt, 1998; Salim et al., 2007). In dusty galaxies, a large fraction of the UV light is absorbed and re-radiated in the infrared to sub-mm wavelengths. Estimating the SFR from observations in those wavelengths has been undertaken recently from sub-mm observations of the SPIRE instrument on board the Herschel Space Telescope (e.g. Buat et al., 2010; Domínguez-Sánchez et al., 2012; Roseboom et al., 2012; Wijesinghe et al., 2011). Other tracers of star formation are the Hα emission from HII regions around young and massive stars and 20cm radio emission from the synchrotron radiation emitted by supernova remnants.

The advent of computer galaxy synthesis models (e.g. Bruzual & Charlot, 2003; Fioc & Rocca-Volmerange, 1997; Leitherer et al., 1999) allows the convenient calibration of the SFR-luminosity relation, assumed to be linear. Inputs to the model include the Initial Mass Function (IMF, see section 7.1.1), the duration of the starburst, a dust extinction law and the metallicity of the gas. The SFR is kept constant (usually at $1 M_{\odot} yr^{-1}$) and the resulting luminosity is used for the calibration. Some popular calibrations are discussed in section 7.1.2.

Total SFRs derived from the UV and the FIR can be used to calibrate the dust attenuation A_{UV} as a function of the UV slope β, see section 7.2.2.2. This is an important tool, in the case where only UV observations are available.[1]

In this chapter we will be matching Galaxy Evolution Explorer (*GALEX*) DR6 objects with fluxes in the *NUV* and *FUV* bands at 231 and 153 nm respectively to H-ATLAS reliable VIKING counterparts and presenting our resulting SFRs and dust attenuation relation in section 7.2.

[1] The relation between A_{UV} and β assumes a theoretical dust extinction law as input into synthesis models. We are not discussing theoretical dust extinction laws in this work, but will cite the law used where appropriate.

7.1 Calculating the SFR

7.1.1 The Initial Mass Function

The IMF ξ is an important input into stellar synthesis models. It represents the number of stars formed per unit mass within the possible mass range:

$$dN = \xi(m)dm \tag{7.1}$$

Salpeter (1955) introduced the functional form

$$\xi(m) = km^{-\alpha} \tag{7.2}$$

and found $\alpha = 2.35$ for main-sequence stars in the solar neighbourhood in the mass range $0.4 < m/M_{\odot} < 10$. Kroupa (2001) added different power-law indices for stars at the lower mass end: $\alpha = 1.3$ for stars with $0.08 < m/M_{\odot} < 0.5M$ and $\alpha = 0.3$ for stars with $0.01 < m/M_{\odot} < 0.08$. Chabrier (2003) proposed a log-normal form of the IMF for $m < 1M_{\odot}$. Low mass stars are hence observed to be much more abundant than high mass stars, although the slope of the mass function does flatten considerably towards very low mass stars[2].

The birth places of stars are dense molecular clouds and at least for those clouds in our Galaxy, the IMF is found to be fairly constant with Salpeter or Kroupa power-law indices, despite the disparity in the physical conditions. Hence, the usual practice is to assume either IMF for the estimation of the SFR of a galaxy, even though deviation from the Milky Way IMF has been found recently, see Dutton et al. (2012) and references therein. Considering that measurements of star formation are mainly concerned with massive young stars, the assumption of a power-law IMF with a Salpeter index seems appropriate.

In addition to providing a list of pre-defined IMFs (e.g. Salpeter or Kroupa), some models also allow user-defined IMF input, for example the `STARBURST99` code (Leitherer et al., 1999) as used by Buat et al. (2010).

[2]The theoretical limit for the ignition of hydrogen lies at $0.08M_{\odot}$. Kroupa (2001) include hence objects without hydrogen burning but that could sustain some thermal equilibrium from deuterium reactions.

7.1.2 Calibration of the SFR-luminosity relation

One of the key output parameters of stellar synthesis models is the luminosity of the galaxy, either bolometric or in different wavelength bands as the UV or IR. For the relationship between far-infrared luminosity and SFR in starbursts it is usually assumed that most of the UV radiation from young stars is re-radiated by dust so that the relation is linear; the input SFR of the models (usually $1 M_{\odot}$) allows then the calibration of this linear relationship.

The most popular calibration for the far-infrared luminosity is from Kennicutt (1998):

$$\mathrm{SFR}/M_{\odot} yr^{-1} = 4.5 \times 10^{-44} L_{\mathrm{FIR}}/\mathrm{ergs\,s^{-1}} = 1.7 \times 10^{-10} L_{\mathrm{FIR}}/L_{\odot} \tag{7.3}$$

using the starburst synthesis model of Leitherer & Heckman (1995) for a continuous burst with a Salpeter IMF and solar metallicity. The FIR luminosities were derived from photometry at shorter wavelength (mainly from IRAS) as was usual at a time without reliable FIR observations. For galaxies at $z < 1.5$, a number of studies (e.g. Elbaz et al., 2010; Rodighiero et al., 2010) have since shown that the FIR luminosities extrapolated from the mid-infrared (mainly at $24\,\mu$m) are tightly correlated to the FIR luminosities observed by *Herschel*.

The assumption that all the IR radiation originates from young stars is valid in the case of starbursts, but needs to be re-considered if the sample contains normal galaxies where some fraction of the IR emission is due to older stars, especially if shorter than FIR wavelength ranges are used.

Buat et al. (2007) (hereafter B07) use an updated version of the above synthesis model, `STARBURST99` by Leitherer et al. (1999), with a Kroupa IMF and derive the following calibration of the SFR from the FIR luminosity:

$$\mathrm{SFR}_{\mathrm{FIR}}/M_{\odot} yr^{-1} = 1.1 \times 10^{-10} L_{\mathrm{FIR}}/L_{\odot} \tag{7.4}$$

B07 raise the issue that a fraction of the SFR could be missed if only the FIR luminosity is taken into account: most starbursts do also radiate in the UV and in the optical and

hence not all of the young star's radiation is absorbed by dust. They therefore also investigate the SFR as deduced from the UV radiation which results in:

$$\mathrm{SFR_{UV}}/M_{\odot}yr^{-1} = 2.0 \times 10^{-10} L_{\mathrm{UV}}/L_{\odot} \tag{7.5}$$

They also include the possibility that older stars contribute to the dust heating by using the following relation for the luminosity due to young stars:

$$L_{\mathrm{tot}} = L_{\mathrm{UV}} + (1-\eta)L_{\mathrm{FIR}} \tag{7.6}$$

It has been found that the value of η lies between 0.2 and 0.4 in the nearby universe for similar galaxy samples (Bell, 2002; Popescu et al., 2011) and B07 use $\eta = 0.3$ in their analysis. The SFR is hence calculated by B07 as:

$$\mathrm{SFR_{tot}}(M_{\odot}yr^{-1}) = \mathrm{SFR_{UV}} + 0.7\,\mathrm{SFR_{FIR}} \tag{7.7}$$

Buat et al. (2010) (hereafterB10) employ their calibrations for UV and FIR derived SFR values, as well as the total SFR by setting $\eta = 0$ when using *Herschel* detected galaxies cross-matched with galaxies detected in the *NUV* by *GALEX*. To be able to compare our results to their findings, we will likewise use $\eta = 0$ in section 7.2.

7.2 SFRs and dust attenuation from *Herschel* and *GALEX* observations

We have calculated SFRs from the FIR and the UV and have considered the contribution of either wavelength band to the total SFR. From this we have derived a dust attenuation law for UV luminosities. Our results are compared with those from B10, Wijesinghe et al. (2011) and others.

7.2.1 Data selection

We are using the SPIRE galaxies in the G09 field that have reliable VIKING counterparts (e.g. $R > 0.8$, see chapter 4) with $z < 1$ (where available, we have used

spectroscopic redshifts, otherwise our photometric redshifts, see chapter 5) consisting of 10,682 galaxies. We then cross-match the galaxies, using VIKING positions, with the *GALEX* DR6 catalogue choosing the nearest object within a matching radius of 2" and a detection in *NUV*. This leads to 3889 objects with *GALEX* matches, a matching rate of 36.4%. This relatively low rate is mainly due to the shallowness of the *GALEX* fields in the G09 field: they have only been observed as part of the AIS (All Sky Survey) or the MIS (Medium Imaging Survey) with exposure times of 100 and 1500 seconds respectively, to overlap with the SDSS survey.

The UV luminosities are derived at rest-frame 153nm and are hence defined as νL_ν. They have been calculated by assuming a power-law continuum of the form $f_\lambda \propto \lambda^\beta$ where λ the wavelength with 120nm $< \lambda <$ 260nm and f_λ the flux per unit wavelength and fitting the *NUV* and *FUV* *GALEX* fluxes. If the object was not detected in the *FUV* (1739 objects), we have used the mean F_{FUV}/F_{NUV} colour of the subsample with *FUV* flux (2150 objects), following B10.

We were able to fit 2893 *GALEX* objects, using a MATLAB routine, selecting only objects with $\chi^2 < 10$. Fig. 7.1 shows the resulting UV luminosity distribution (light grey) and Fig. 7.2 shows the redshift distributions of the *NUV* detections (grey) and the *NUV* detections with a fitted power-law (blue). From Fig. 7.2 it is clear that although we lose 25% of objects in the fitting, we do not introduce a redshift bias.

The FIR luminosity L_{FIR} has been calculated by integrating the fitted isothermal spectrum in the range $8\,\mu$m $< \lambda < 1000\,\mu$m. Only isothermal fits with $\chi^2 < 10$ have been used in the analysis. 2353 of the 2893 power-law fitted *GALEX* objects also had FIR luminosity from a good isothermal fit, see the red and blue histograms in Fig. 7.1 for the luminosity distributions in FIR and UV respectively of this sample. We use those 2353 objects to produce our $L_{\rm FIR}/L_{\rm UV}$ ratios. For the relation between β and $L_{\rm FIR}/L_{\rm UV}$, we would like to compare our results with those of Kong et al. (2004) and Buat et al. (2010), using objects with *NUV* and *FUV* detections only and keeping the redshift of our sample at $z < 0.3$, the limit used by Kong et al. (2004) to calculate β from the *NUV* and *FUV* fluxes. This results in a sample of 1121 galaxies, of which

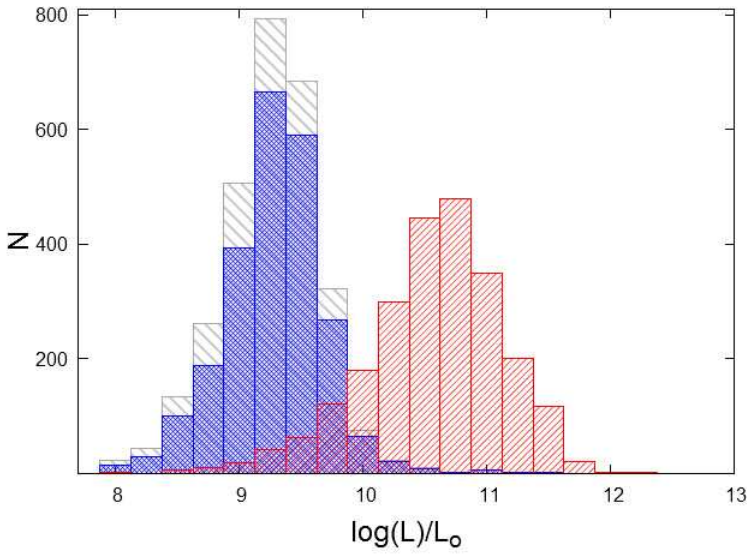

Figure 7.1: — The luminosity distribution of *GALEX* objects that are strong candidates to be counterparts to SPIRE G09 galaxies. $L_{\rm UV}$ is calculated by fitting *NUV* and *FUV* fluxes to a power-law (grey: all fitted, blue: with FIR luminosities calculated from isothermal fits to SPIRE data). The red histogram shows the $L_{\rm FIR}$ distribution.

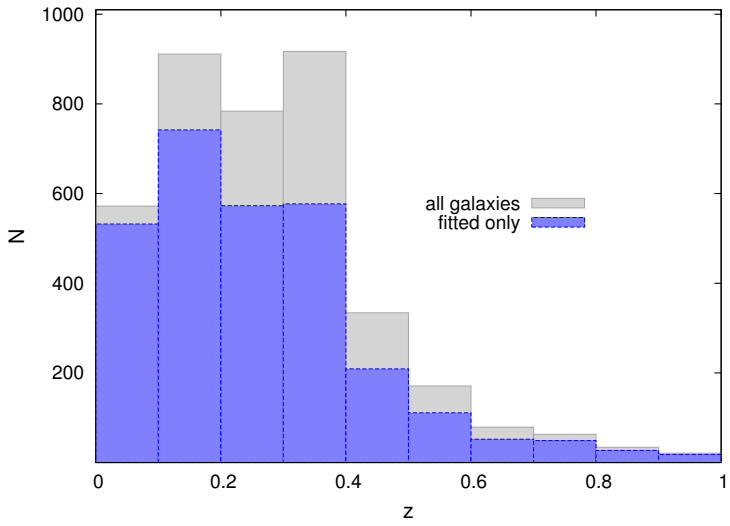

Figure 7.2: — Redshift distribution of the *GALEX* objects that have a good power-law fit (light grey) and that also have FIR luminosities from an isothermal fit to SPIRE fluxes (blue).

449 are detected at 10σ in both NUV and FUV.

7.2.2 Dust attenuation

The extinction of UV radiation is tightly correlated with the dust content of a galaxy. The ratio $L_{\rm FIR}/L_{\rm UV}$, or more commonly IRX for Infrared Excess, is hence a valuable measurement of the dust attenuation, and it has been shown that the IRX is a solid tracer for the dust extinction in star-forming galaxies (e.g. Buat et al., 2005; Meurer et al., 1999). In section 7.2.2.1 we investigate the IRX as a marker for dust attenuation in our sample.

If infrared data is not available, the dust extinction can still be estimated from the slope β of the UV continuum due to the correlation between β and IRX at least in the case of starbursts (e.g. Calzetti et al., 2000; Kong et al., 2004; Meurer et al., 1999). It has been shown recently that β as an obscuration metric is less reliable and depends to some extent on the type of the galaxy (Boissier et al., 2007; Buat et al., 2010; Wijesinghe et al., 2011). In section 7.2.2.2, we compare the IRX and β to check the robustness of β as a tracer for dust attenuation in our sample.

7.2.2.1 The Infrared Excess

Fig. 7.3 shows the expected increase of $L_{\rm FIR}/L_{\rm UV}$ (IRX) with $L_{\rm FIR}$. Our results (empty black triangles, solid line) are in good agreement with the results from B10 (empty orange squares, solid line) who have used *Herschel* galaxies out to $z \sim 1$. This consistency is encouraging. As well as resulting from a low number of galaxies in the highest luminosity bin, our higher mean IRX value in the range $12 \leq \log L_{\rm FIR} < 12.5$ could be affected by a bias against higher redshift galaxies from the cross-matching with VIKING and we could well mask a more consistent downward trend for higher luminosities as found by B10.

B10 find a deviation from their earlier relation in B07 (filled orange circles, solid line), who used a local sample of $60\,\mu$m selected galaxies, from about $z > 0.5$ by ~ 0.3 dex, implying a decrease in dust attenuation for higher redshifts. Their (and

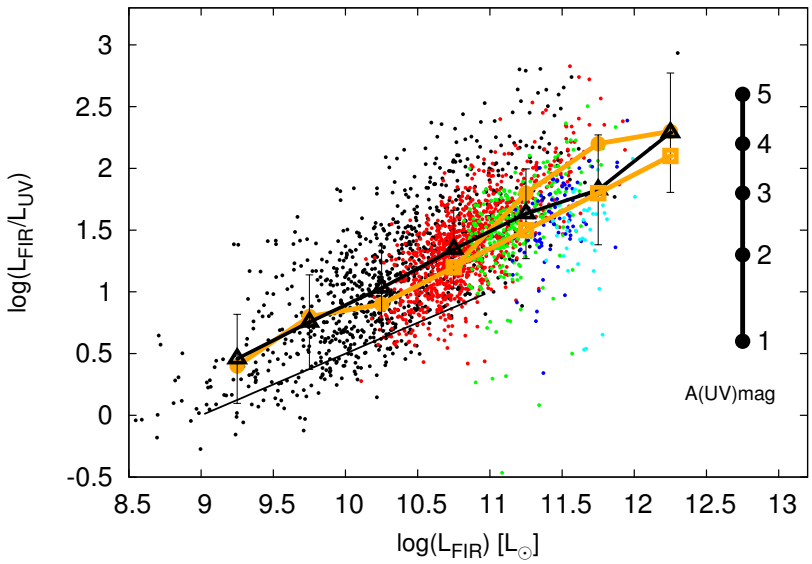

Figure 7.3: — $L_{\rm FIR}/L_{\rm UV}$ (IRX) versus $L_{\rm FIR}$ for the 2353 galaxies in our G09 sample. The redshift is colour-coded as follows: black $0 < z < 0.2$, red $0.2 < z < 0.4$, green $0.4 < z < 0.6$, blue $0.6 < z < 0.8$, cyan $0.8 < z < 1.0$. The black triangles and solid line represent the mean ratios in $L_{\rm FIR}$ bins of 0.5 dex in our sample. The orange filled circles and solid line show the mean for a 60 μm selected sample of nearby galaxies by Buat et al. (2007) (B07), from their fig.7. The empty orange squares and solid line are taken from Buat et al. (2010) (B10), their fig.1. The thin black line represents the relation found by Bell et al. (2003) for a sample consisting of normal and star-forming galaxies. The A(UV) scale, black filled circles and solid line, is taken from Buat et al. (2005).

our) deviation from the local relation in B07 is still within 1σ errors though and this downward effect might not be real.

Our ratios, as well as those of B07 and B10, are systematically higher than those found by Bell et al. (2003), see thin black line in Fig. 7.3. Bell et al. (2003) have explicitly removed AGN from their sample of IR and UV selected galaxies. The inclusion of AGN, as in our sample or indeed in the samples of B07 and B10, could increase the $L_{\rm FIR}/L_{\rm UV}$ values by a significant factor; this has not been investigated further here.

7.2.2.2 UV slope β

In the absence of FIR observations, it is usual to estimate the dust attenuation from the slope β of the UV continuum. This approach was formalised by Meurer et al. (1999). They start with a model of the dependence of the observed IRX on the dust attenuation $A_{\rm UV}$ and show that this model is in good agreement with the outcomes of the synthesis model of Leitherer et al. (1999), assuming starburst parameters and a variety of extinction laws. They then calibrate the IRX - $A_{\rm UV}$ relation from empirical SEDs of local starbursts. Finally, they find an empirical relation between IRX and β (using local starburst galaxies with *IRAS* detection) and produce a relationship between the dust extinction $A_{\rm UV}$ and β:

$$A_{160\rm nm} = 4.43 + 1.99\beta \tag{7.8}$$

The above equation from Meurer et al. (1999) is frequently used, even in situations where the assumptions (local starburst galaxy) are not met. Meurer et al. (1999) themselves apply eq. 7.8 to a sample of galaxies at much higher redshifts, assuming that the relationship does not change significantly with redshift.

Wijesinghe et al. (2011) offer a different attenuation relation[3] for β:

$$A_{\rm FUV} = -0.04\beta^3 + 0.26\beta^2 + 2.12\beta + 2.29 \tag{7.9}$$

from a sample of 875 galaxies from the 5-band catalogue of the H-ATLAS SDP field with *GALEX* MIS UV data (from the GAMA multi-wavelength catalogue).

Fig. 7.4 shows our IRX-β relation for the 1121 galaxies of our initial sample that are at $z < 0.3$ and that have both *NUV* and *FUV* detections. Out of these 1121 galaxies, 449 have 10σ detection in both *NUV* and *FUV* and are represented with dots for $L_{\rm FIR} < 10^{11} L_{\odot}$ and filled squares for $L_{\rm FIR} > 10^{11} L_{\odot}$ in fig. 7.4. Galaxies without the 10σ detections are shown as empty squares. Our linear fit is:

$$\log(L_{\rm FIR}/L_{\rm UV}) = 0.44\beta + 1.23 \tag{7.10}$$

[3] We have calculated eq. 7.9 from their eq.5 and eq.2 from Buat et al. (2005), as suggested by Wijesinghe et al. (2011).

using only galaxies with 10σ detections.

A comparison with other findings suggests that our local sample comprises the whole spectrum of star-forming galaxies, from normal spirals to starbursts. Kong et al. (2004) used a sample of 50 nearby starbursts and it is not surprising that our higher luminosity galaxies are scattered around their fit on the IRX-β plane (see thin solid line in Fig. 7.4). The fit of Meurer et al. (1999), shown as the dotted line, is similar to that of Kong et al. (2004), if somewhat offset. Boissier et al. (2007) investigated the relation for 48 normal star-forming galaxies and their fit is shown as the dotted line in Fig. 7.4. Our fit closely follows that of Boissier et al. (2007) suggesting that a dust attenuation on the assumption of local starbursts, e.g. eq. 7.8, would not be appropriate. Buat et al. (2010) find a similar IRX-β relation, their fig.2, but do not supply a fit[4]. Most of their galaxies lie between the fits of Kong et al. (2004) and Boissier et al. (2007).

Wijesinghe et al. (2011) also use a H-ATLAS sample, drawing on the GAMA multi-wavelength catalogue which provides photometry from SDSS, UKIDSS, H-ATLAS and *GALEX* allowing them to apply a SED fitting method. The SDP field is part of the G09 field and our samples should in principle overlap, at least at the low redshift considered here. It is hence surprising that our respective fits, as seen in Fig 7.4 seem not very comparable. The fit of Wijesinghe et al. (2011) (dot-dashed line) shows the steepest slope of all relations compared and approaches the fit of Kong et al. (2004) for higher values of β.

Buat et al. (2005) have used the synthesis code `PEGASE` to explore the dependence of $A_{\rm FUV}$ on the IRX. Combining their eq.2 ($A_{\rm FUV}$(IRX))with our eq. 7.10, we derive the following relationship between the dust attenuation $A_{\rm FUV}$ and β for our sample (the cubic term is negligible):

$$A_{\rm FUV} = 0.04\beta^2 + 0.84\beta + 2.44 \tag{7.11}$$

Fig. 7.5 illustrates the relation (thick solid line). Also shown are the fits of Kong et al. (2004), Meurer et al. (1999), Boissier et al. (2007) and Wijesinghe et al. (2011),

[4]We have modeled our Fig. 7.4 closely on their fig.2 to allow easy comparison.

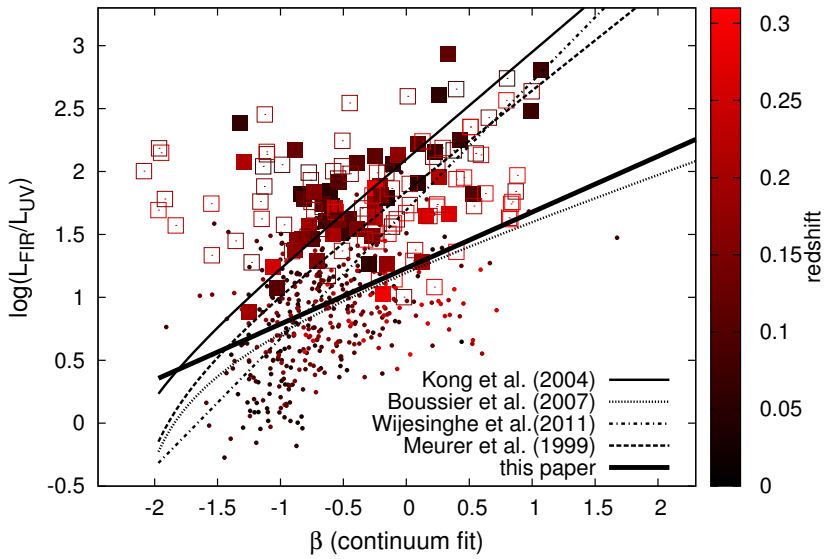

Figure 7.4: — $L_{\rm FIR}/L_{\rm UV}$ (or IRX) versus the UV spectral slope β for our sample at $z < 0.3$. Dots represent galaxies with $L_{\rm FIR} < 10^{11}$ and a 10σ detection in both *NUV* and *FUV*. Galaxies with $L_{\rm FIR} > 10^{11}$ (LIRGS) are shown as squares (filled if 10σ detection for both UV bands, otherwise empty). Our fit to the secure detections is represented as the thick line; other fits are also shown. The majority of galaxies lie between the fits of Kong et al. (2004), from local starburst, and Boissier et al. (2007), from normal galaxies. Our fit closely follows the fit of Boissier et al. (2007), suggesting that the bulk of our sample is formed of normal galaxies without high star formation rates.

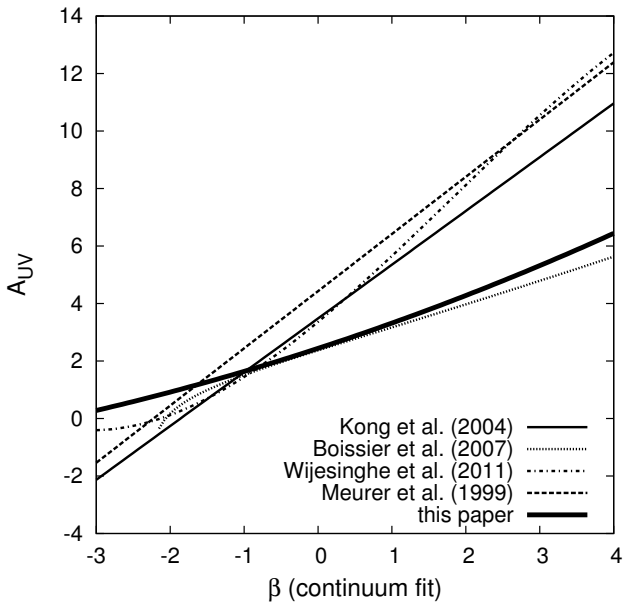

Figure 7.5: — Several fits of the $A_{\rm UV} - \beta$ relation. Our own fit (thick solid line), calculated using our IRX-β relation as shown in Fig. 7.4 and eq.2 of Buat et al. (2005) is in good agreement with the fit of Boissier et al. (2007) and suggests that the bulk of our sample is comprised of normal disk galaxies. The fits of Kong et al. (2004) and Meurer et al. (1999) are derived from local starbursts and do not fit our sample very well.

as deduced from their relations shown in Fig. 7.4. As expected, our dust attenuation follows closely Boissier et al. (2007), if slightly higher for galaxies with a slope at the lower or higher ends of the range. It is substantially lower though, at least for $\beta > 0$, than the dust attenuation laws from Kong et al. (2004), Meurer et al. (1999) and Wijesinghe et al. (2011). This is not surprising for the studies of Kong et al. (2004) and Meurer et al. (1999) as they use samples of starburst galaxies. The discrepancy between our findings and those of Wijesinghe et al. (2011) are rather unexplained in the light of overlapping samples from the same survey. Most likely, the differences stem from the differences in the sample selection: they use a slightly higher redshift limit of $z < 0.35$ to produce their IRX-β relationship, rely on galaxies with an optical (SDSS) counterpart and, do not restrict their fit to galaxies with 10σ detections in both *NUV* and *FUV*. It is unclear though if and how any of these factors influences the results without following the same selection criteria. As expected, our luminosity distributions are very similar, as can be seen from Fig. 7.6, compared to their fig.5. We see the same trend as Wijesinghe et al. (2011) of a higher constraint of the IR luminosities at higher UV luminosities. We have also followed the prescription of Kong et al. (2004) to calculate β from the *FUV*-*NUV* colour, as used in Wijesinghe et al. (2011); the resulting slopes do not differ significantly from those derived using the power-law fitting.

Sections 4.3.2 and 5.3 suggested that the H-ATLAS sample is comprised of two distinct populations with normal galaxies at lower redshifts. Given our agreement with the fits of Boissier et al. (2007) who used a sample of normal disk galaxies, we will trust our own findings and use eq. 7.11 in the following section to estimate SFRs.

7.2.3 Calibrating the $\mathrm{SFR_{FIR}}$

Ideally, when calculating SFRs, we use both FIR and UV observations to include the radiation from the massive young stars and the 'hidden' star formation in the form of UV radiation absorbed by dust and re-radiated in the infrared range. Often this is not possible though and it is useful to be able to quantify the error in the SFR when

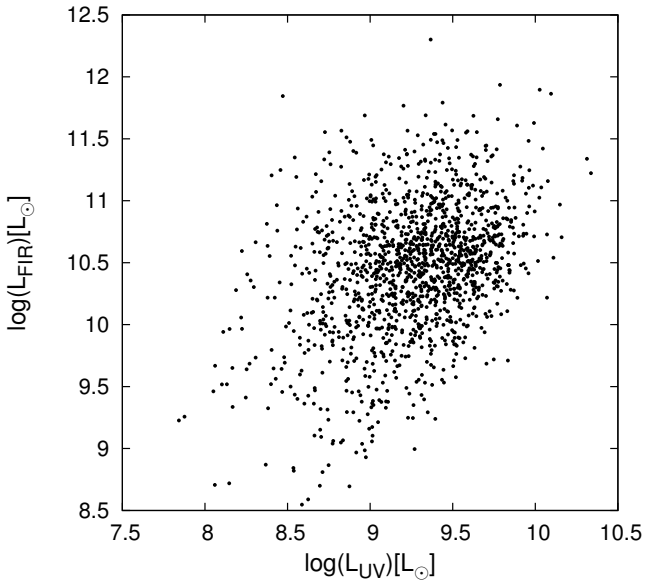

Figure 7.6: — FIR luminosities versus UV luminosities. The relationship is rather weak, but seems to depend to some extend on the UV luminosity: at higher $L_{\rm UV}$, the scatter in the $L_{\rm FIR}$ is smaller than at lower $L_{\rm UV}$. This trend is also found by Wijesinghe et al. (2011) and illustrated in their fig.5.

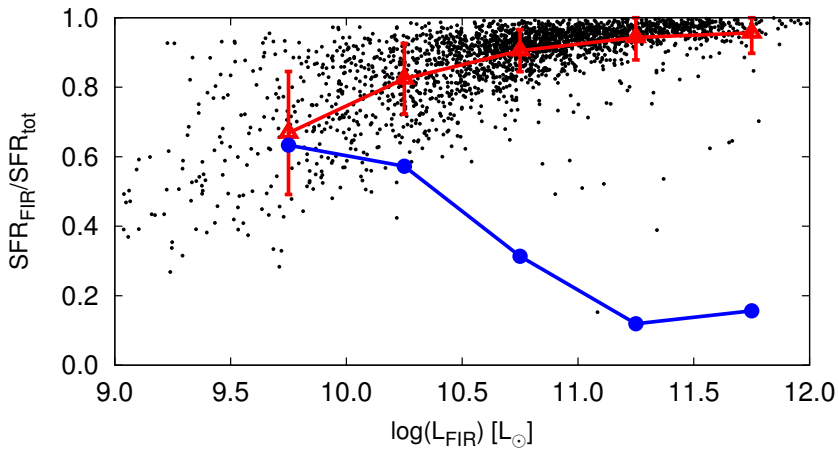

Figure 7.7: — The fraction of the SFR observed in the FIR as a function of $L_{\rm FIR}$. The contribution of the $\rm SFR_{FIR}$ to the total SFR increases with increasing luminosity. The red triangles joined by the red line represent the mean values in the log-luminosity bins $< 10, 10-10.5, 10.5-11, 11-11.5, > 11.5$. The UV detection rate in each luminosity bin is shown by the blue filled circles.

observations in only one of the wavelength ranges are available.

We use

$$\rm SFR_{tot} = SFR_{FIR} + SFR_{UV} \tag{7.12}$$

as our total SFR forecast where $\rm SFR_{\mathit{FIR}}$ and $\rm SFR_{\mathit{UV}}$ are calculated as in eq. 7.4 and 7.5 respectively, following B10. This assumes that all infrared (mid-far) radiation is emitted by dust and neglects the contribution of stellar photospheres, which is very small at long wavelengths (i.e. $\eta = 0$ in eq. 7.6), a Kroupa IMF, a constant star formation and solar metallicity. $L_{\rm UV}$ is uncorrected for dust extinction.

Fig. 7.7 shows the fraction of the total SFR that is attributed to the FIR as a function of $L_{\rm FIR}$ and also the UV detection fraction in bins of 0.5 dex (blue line), using our sample of 2353 galaxies with fitted $L_{\rm FIR}$ and $L_{\rm UV}$. We can see that the contribution from the FIR to the total SFR increases with increasing $L_{\rm FIR}$; at lower $L_{\rm FIR}$, the SFR

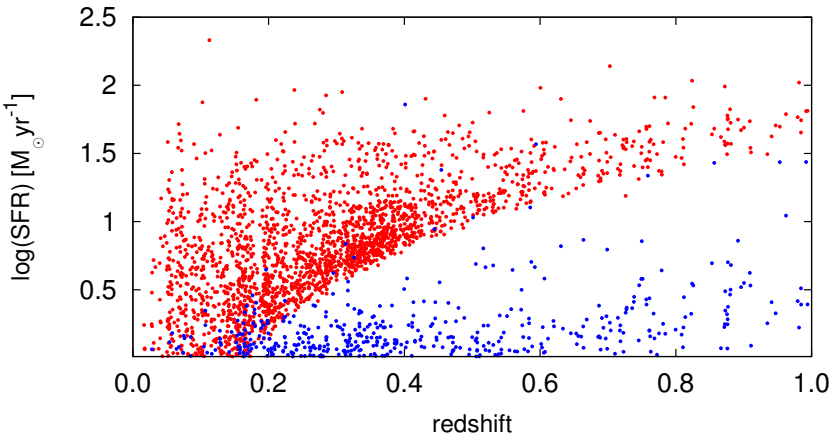

Figure 7.8: — The redshift dependence of the calculated star formation rates. SFR_{FIR} is shown in red, SFR_{UV} in blue. At higher redshifts, the relative UV contribution decreases.

from FIR alone is not a good estimator of the total SFR and clearly, UV observations are needed. At $L_{FIR} > 10^{11.5} L_{\odot}$, a mean of 96% (±6%) of the total SFR can be contributed to the FIR emission albeit with a low UV detection rate of 16%. At $L_{FIR} < 10^{10} L_{\odot}$, the mean contribution decreases to 66% (±19%) with a UV detection rate of 63%. The SFR_{FIR} contributions to the total SFR are comparable to the findings of B10, even though their UV detection rate is much more favourable, see their fig.3. This is chiefly the result of the deeper *GALEX* coverage of the Lockman-SWIRE field used in their study. Our findings hence emphasise the need to build FIR and UV samples to estimate the total SFR of all but the most luminous galaxies. This could be redshift dependent to some extent, as can be seen on Fig. 7.8 which shows the individual SFRs, from the FIR and the UV, as a function of redshift. At higher redshifts, the UV contribution becomes increasingly negligible in our sample. This could be a selection effect: firstly, there are more dusty star-forming galaxies at higher redshifts in the H-ATLAS-VIKING catalogue (see sections 4.3.2 and 5.3), secondly, because of the shallow UV coverage, higher redshift galaxies are proportionally under-represented.

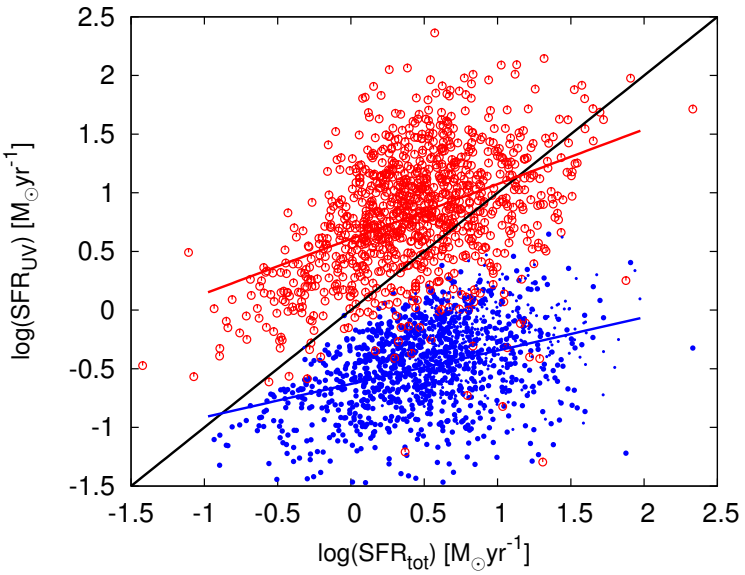

Figure 7.9: — Comparison of SFR_{UV} with the total SFR. Values derived from dust absorption corrected luminosities using the prescription of Meurer et al. (1999) are shown in red, from uncorrected luminosities in blue. To narrow the uncertainties, only galaxies with $z < 0.2$ have been included in the log-linear fit to both groups (red and blue lines).

Next, we would like to check the viability of our UV dust attenuation, see eq. 7.11. For this, we correct the UV luminosities in our sample and compare the resulting $\mathrm{SFR}_{\mathrm{UV}}$ to the total SFR as calculated from eq. 7.12; in principle, they should match. We also follow this procedure for the dust attenuation equations from Meurer et al. (1999) and Wijesinghe et al. (2011). The results can be seen in Figs. 7.9 , 7.10 and 7.11.

In any of the figures, we can see that the uncorrected $\mathrm{SFR}_{\mathrm{UV}}$ show only a weak dependency on the $\mathrm{SFR}_{\mathrm{tot}}$ in the log-log plane. This is in contrast to the findings of B10, their fig.4, where the log-linear fit for the uncorrected values shows a higher slope than our fit. This could well arise from the deeper 250 μm limit of 23mJy in the Lockman-SWIRE field and the galaxy sample of B10 is likely to include more of the very dusty starburst at $z \sim 1$. Without data on the redshift or luminosity distributions of their sample, this is difficult to verify though.

B10 have also applied the dust extinction formula of Meurer et al. (1999) to their

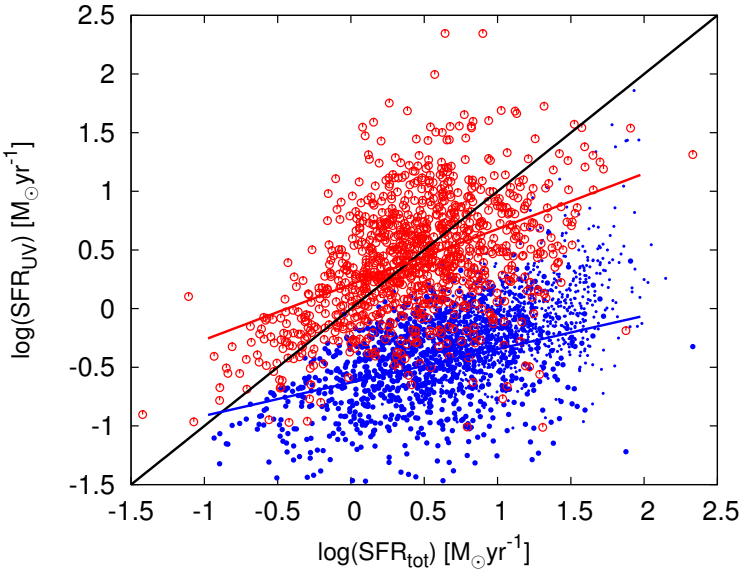

Figure 7.10: — Same as Fig. 7.9, except that the dust extinction was calculated using the formula of Wijesinghe et al. (2011).

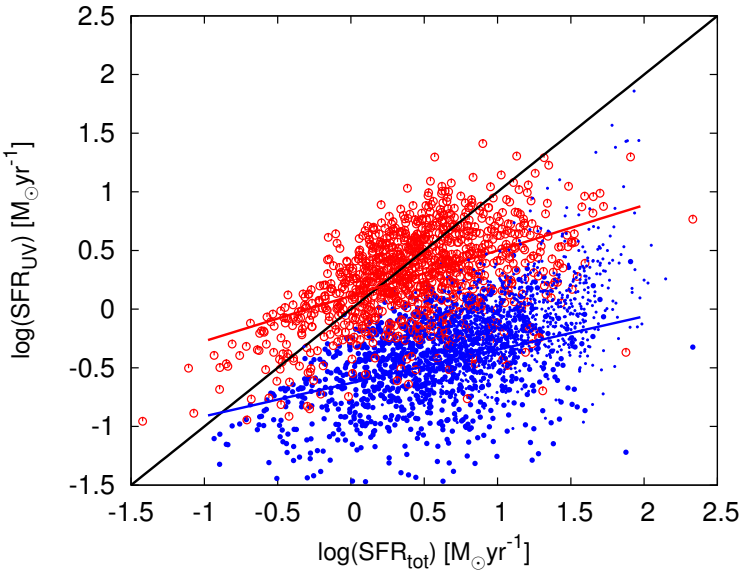

Figure 7.11: — Same as Fig. 7.9, except that the dust extinction was calculated using our formula, i.e. eq. 7.11.

sample of *Herschel* galaxies. Contrary to our findings, their corrected UV luminosities do consistently over-estimate the derived SFR by a factor of $\sim 2-3$. Our corrected values in Fig. 7.11 show overall a lower scatter and estimate the total SFR on average well in the lower to medium SFR range. As expected, at higher total SFR, the corrected $\mathrm{SFR_{UV}}$ values still under-estimate the total SFR, by a factor of ~ 8 at $\mathrm{SFR_{tot}} = 50 M_{\odot} yr^{-1}$. Corrections following the prescription of Wijesinghe et al. (2011) estimate the total SFR slightly better at higher SFR values, but lose this advantage in the lower to medium SFR range; they also show a much larger dispersion overall.

In conclusion, our dust attenuation appears adequate for galaxies that have low and medium SFRs. At higher SFRs, the prescription of Meurer et al. (1999) is more appropriate as expected for a formula derived from a sample of starburst galaxies.

Chapter 8

Conclusions

In this thesis we have investigated a sample of galaxies that are detected with the *Herschel* Space Telescope in the the sub-mm wavelength range and that also have near-infrared detections with the VISTA telescope in Chile as part of the VIKING survey.

We have cross-matched the sub-mm and near-infrared catalogues with a 10" search radius around the SPIRE positions in the G09 field, using a likelihood ratio method which has been modified to allow for a more robust estimation of the probability Q_0 of finding a genuine near-infrared counterpart above the magnitude limit. The results of the matching will be incorporated into a future H-ATLAS data release, together with the optical IDs from SDSS already available.

We have also used a publicly available code to calculate photometric redshifts plus errors for all VIKING objects that lie within the search radius of a SPIRE source using VIKING and SDSS photometry (if available); the photometric redshifts will also be part of the future H-ATLAS data release.

The large majority of our candidates lie at $z \leq 1$, with a median redshift of $\tilde{z} = 0.405$, which is as expected from the magnitude limit of the VIKING survey. Only 2% of the H-ATLAS sources with a reliable counterpart have photometric redshifts $z > 1$ and we estimate that $\gtrsim 30\%$ of all sources are found at $z > 1$. This is fully consistent with the fraction of 250 μm BLAST sources at $z > 1$ found by Dye et al. (2010), but

lower than the same fractions of Dunlop et al. (2010) and Chapin et al. (2011), also both using BLAST sources. There is still broad agreement in the conclusion that the 250 μm sources are drawn from two distinct populations: a lower redshift population consisting of mainly normal, late-type galaxies and a higher redshift population of more dusty, strongly "starbursty" galaxies[1]. The majority of the sources with VIKING counterparts would hence be comprised of normal galaxies and there is further evidence for this from our investigation of the the dust attenuation in chapter 7: from Fig. 7.4, the (Infrared Excess) IRX vs. UV spectral slope β, we see that although we do find LIRGS (Luminous Infrared Galaxies, $L > 10^{11}$) around the fit of Kong et al. (2004) who used local starburst galaxies, the majority of galaxies lie below this fit and more closely resemble the sample of Boissier et al. (2007) who used normal galaxies.

We have then used SPIRE galaxies with reliable VIKING counterparts to investigate the 250 μm luminosity function and its evolution finding strong evolution out to $z \leq 0.6$ and possibly $z \leq 0.8$. This sample is also cross-matched with the *GALEX* space telescope to calculate UV luminosities and to derive star formation rates (SFRs). The SFRs from the FIR and the UV are then compared leading to a formula for UV dust attenuation that might be most appropriate for H-ATLAS sources up to $z \sim 1$.

The results presented in chapter 6 and 7, the submm luminosity function and the star formation rates respectively, rely heavily on the cross-matching results and the subsequent photometric redshifts. It was hence important to ensure that this data is meticulously assembled and therefore we have spent the majority of the research time on fine-tuning of the methods as described in chapters 4 and 5.

The likelihood ratio (LR) method forms the basis of our cross-matching: how can we find VIKING counterparts to the SPIRE detections that have wildly higher positional uncertainties increasing the search radius and hence including a high number of possible identifications? And how can we attach a self-consistent probability, i.e. reliability, to any counterpart? In the absence of radio data in the search area, we have found that the

[1] A formal definition of starburstiness has been undertaken by Elbaz et al. (2010), using comparative measures of specific SFR and compactness of the star-forming region.

LR method offers the best alternative, taking into account the magnitude distribution of true counterparts, the probability distribution of the SPIRE positional errors and the classification into stars and galaxies. All three properties are not known a priori and we spent considerable time deriving trustworthy estimates. Nevertheless, the matching process introduces the possibility for uncertainties.

The classification into stars and galaxies, as described in section 2.1.1.2, is crude; ideally QSOs would form a separate class, or would at least be reliably classified as galaxies. Currently, QSOs without SDSS spectra are classified as stars, selected by morphology. This reduces the likelihood that a QSO is selected as a reliable counterpart because of the low value of Q_{0s} used in the calibration; Q_{0s} truly reflects the low probability of a star being detected by SPIRE, but we are hence more likely to miss true QSO identifications. A future investigation could study a possible QSO colour classification scheme, starting with the research of Findlay et al. (2012) using near-infrared and optical photometry for high redshift QSOs, or maybe by exploiting the K-band excess of QSOs with respect to foreground stars (Maddox et al., 2012, 2008; Warren et al., 2000), both also requiring visible photometry.

Quasars can also be detected in the X-ray; heavily obscured quasars, either by dust tori around the AGN or by high dust content of the host galaxy, can still be observed in the hard X-ray range ($\gtrsim$ 5keV). NASA's Chandra and ESA's XMM-Newton x-ray space telescopes both provide some coverage in the equatorial GAMA fields, and it might be worthwhile to cross-match with our VIKING catalogue for a candidate list of quasars. NuStar (Nuclear Spectroscopic Telescope Array), a NASA small explorer mission which was launched in June 2012, is well placed to observe dusty QSOs with an energy band of 5-80keV (Harrison et al., 2010). eRosita, a German-Russian collaboration, is planned to launch in 2014 and will provide an all sky survey, observing in the 0.5-10keV band over 4 years. However, this might still miss some of the most obscured quasars that are likely to be observed by *Herschel*.

The probability distribution of the SPIRE positional errors is still the subject of an investigation within the H-ATLAS team. Our assumption of a Gaussian error might

not hold and there is evidence of more elliptical errors. In practice, our search radius should still include all of the genuine matches; in some cases, possible matches might have a reliability that is too low if the offset is in the direction of the higher positional uncertainty (the scanning direction). Our reliable catalogue is hence conservative and might increase with the inclusion of the elliptical error models in the future.

The magnitude distribution of the true counterparts is tricky to calculate, as described in section 4.2.2. The normalisation Q_0 of the background-subtracted magnitude distribution is easily overestimated because of true multiple counterparts and the effects of clustering. Our new method avoids the multi-counting issue by using SPIRE blanks and a model of the dependence of true blanks, i.e. observed blanks plus those positions with a random line-of-sight object, on the search radius. This method has subsequently been used by several authors (Bond et al., 2012; Kim et al., 2012; McAlpine et al., 2012) matching mid-infrared or radio catalogues to SPIRE sources.

Bond et al. (2012) have matched SPIRE detections in the GAMA 15h field to objects in the Wide-field Infrared Survey (WISE, Wright et al., 2010) catalogue, detecting in 3.4, 4.6, 12 and 22 μm, and found reliable counterparts for 50.6% of the SPIRE sources, a fraction that is similar to ours. They find a high fraction of AGN (0.30), from colour selections in the mid-infrared, in a subsample of 9% of all matched galaxies that have no redshift assigned from SDSS counterparts and are assumed to lie at redshifts $z > 0.5$. WISE data for the G09 field is now available, and it would be most interesting to cross-match with our initial VIKING input catalogue and to follow their method of AGN selection which would be useful in our star-galaxy separation scheme, as discussed above.

Kim et al. (2012) find an identification rate of 86% when matching the SPIRE catalogue of the SDP field to *Spitzer* IRAC objects, having detection limits of an order of magnitude fainter in the 3.6 μm band than the WISE survey. They estimate that 40% of SPIRE sources lie at high redshifts, somewhat higher than our estimate of $\sim 30\%$.

McAlpine et al. (2012) match radio catalogues with K_s-selected NIR catalogues and

investigate the impact of the resolution of radio images, limiting K_s magnitude and size of the search radius on the performance of the LR method. Their table 1 shows clearly how our estimation of the probability Q_0 of finding a genuine near-infrared counterpart above the magnitude limit is independent of the search radius employed in comparison to the methods of Ciliegi et al. (2003) and Smith et al. (2011), and is hence preferable.

The LR method following Sutherland & Saunders (1992) assumes that there is only one true counterpart for each source. An adaptation of the LR method to include genuine multiple counterparts is another possibility for a future research project. Both Steve Maddox and myself have brought forward ideas on how to extend the LR method to allow for more than one true counterpart and this could lead to a future collaboration. The candidates for true multiple counterparts also define an exciting group of galaxies to study as we would hope to find a high number of mergers and cores of galaxy clusters. For example, Hoyos et al. (2012) present a new automatic method for finding mergers from morphological information extracted from HST images. Our current list of 1444 candidates could be included in a target list for ALMA to obtain sub-arcsec positions which facilitates the decision on reliable VIKING counterparts.

Only 1768 spectroscopic redshifts from deep redshift surveys (DEEP2 and zCOSMOS) were found for the inclusion in our photometric redshift training set, a fraction of only ∼5.5%. We estimate that $\sim 30\%$ of galaxies in H-ATLAS lie at $z > 1$ and this low fraction would under-represent the high redshift end and might lead to a bias in our photo-z estimation towards lower redshifts. Indeed, in section 5.3.1, we found that our photo-z algorithm underestimates the true redshift with an average of ≈ 0.09 from about redshift $z \simeq 0.3$. This bias might decrease with the availabilty of more higher redshift training objects.

The accuracy of the photometric redshift also depends on the number of photometric broad-bands available for each object; some visible surveys currently underway, especially VST KIDS which overlaps with VIKING and which should provide near-complete optical detections, will be of great help to the calculation of more accurate photometric redshifts. We have also discussed the possibility that differences in the

colour distributions of the training set and our galaxy sample could play a major role. An interesting future project would investigate those distributions in more detail and might discover clues as how to assemble more realistic training sets thus leading to better photometric redshifts when using these empirical methods.

In chapter 6, we have investigated the evolution of the submm luminosity function using SPIRE objects and our reliable VIKING counterparts together with the estimated redshifts from photometry. We are in broad agreement with the current literature, even though the case for evolution beyond $z \geq 0.6$ is weak. This emphasises the need for a more complete reliable catalogue, achievable with observations from ALMA or with the inclusion of data from the VST KIDS survey. From our investigation of the submm LF, especially Fig. 6.13 there is also good evidence, that the SPIRE galaxies can be crudely divided into two classes by S_{250}/S_{350} colour that might behave in very different ways. This can be seen clearly in Fig. 6.13 where the redder galaxies show a greater correlation between temperature and luminosity within each redshift slice of width $\triangle z = 0.2$. Running the LR analysis separately for the red and blue classes might give more insights into the nature of the SPIRE galaxies with VIKING counterparts.

We have used an isothermal fitting of the SPIRE fluxes to obtain our temperatures, k-corrections and 250 μm luminosities. Inclusion of PACS data, i.e. fluxes in 100 and 160 μm would improve the fitting by reducing the number of sources with temperatures that could not be reliably constrained, and lead to more accurate luminosities. The exclusion of PACS data might introduce a bias against galaxies with warmer dust, as shown in Dunne et al. (2011), fig.10. PACS fluxes are now available in version 2 of the Phase 1 catalogue of the GAMA fields and it might prove interesting to compare the 250 μm LF with and without the inclusion of PACS data.

In chapter 7, we studied the dust attenuation of a subset of SPIRE galaxies in the G09 field that have reliable VIKING counterparts and UV detections from *GALEX*. Our sample shows a broader distribution on the IRX-β diagram than those derived from local starburst galaxies and is in general agreement with studies that use more quiescently star-forming galaxies. At the low redshifts considered here ($z \leq 0.3$), our sample

is fairly complete with regards to VIKING counterparts, but misses out on deeper UV observations; therefore, we might have introduced a bias against more heavily obscured star-forming galaxies.

When considering normal disk galaxies, the contribution of older stars might be important; we have used a value of $\eta = 0$ in our estimation of the total SFR and have hence ignored such a possible contribution, to be able to compare our results with that of Buat et al. (2010). It would be interesting to spend more time investigating the influence of different values of η, but in view of the rather low *GALEX* detection rate for our SPIRE sample, it might not provide any more insights.

The addition of NIR counterparts and their photometric redshift to the H-ATLAS catalogue is valuable to a range of different research directions. Negrello et al. (2010) used a reliable VIKING counterpart to identify a lensing foreground galaxy in a study on submm bright, strongly lensed galaxies. The H-ATLAS source was too faint in the optical and fell below the adopted magnitude limit employed in the optical LR analysis by Smith et al. (2011). The emission of the lens dominates in the NIR whereas the submm emission is boosted by the gravitational lensing and the background galaxy is observed as a bright source with SPIRE. Negrello et al. (2010) found 5 such lensing systems in the H-ATLAS SDP field and was able to disentangle the different contributions of foreground and lensed galaxy in the NIR and submm; they also established the redshifts for the lensed galaxy from CO lines, a set of rotational emission lines which traces the molecular gas around starforming regions.

Whereas Negrello et al. (2010) searched for strongly lensed galaxies using a 100mJy flux limit at 500 μm, González-Nuevo et al. (2012) look for high-z, high apparent luminosity SPIRE objects by using flux density cuts ($250 \leq 35$mJy and $S_{350} \leq 85$mJy) and additional colour cuts ($S_{350}/S_{250} > 0.6$ and $S_{500}/S_{350} > 0.4$) deduced from the SEDs of 3 ULIRGS. They then look for close associations with VIKING galaxies; if the photometric properties of identifications seem incompatible with the bright FIR fluxes, the source is deemed a candidate lens system, with the VIKING object as the lens. This results in 31 candidate strongly lensed sources in the H-ATLAS SDP field which

include the 5 lenses from the Negrello et al. (2010) selection.

Reliable NIR counterparts to submm sources will continue to be of importance for the selection of lensed systems, in particular for the identification of the foreground, lensing galaxy. In addition, the inclusion of NIR photometry will provide more accurate SED fitting used in a variety of research to calculate redshifts, k-corrections and luminosities. The research undertaken as part of this thesis should hence provide a useful basis for future studies of galaxies with ALMA and other facilities.

References

Abazajian K. et al., 2009, *The seventh data release of the Sloan Digital Sky Survey,* ApJS, 182, 543 84

Abdalla F. B., Banerji M., Lahav O., Rashkov V., 2011, *A comparison of six photometric redshift methods applied to 1.5 million luminous red galaxies,* MNRAS, 417, 1891 93

Alpher R., Herman R., Gamow G., 1948, *Thermonuclear reactions in the expanding univers,* Physical Review, 74, 1198 14

Amblard a. et al., 2010, *Herschel -ATLAS: Dust temperature and redshift distribution of SPIRE and PACS detected sources using submillimetre colours,* A&A, 518, L9 25, 63, 94, 101

Arnaboldi M. et al., 2007, *ESO Public Surveys with the VST and VISTA,* Msngr, 127, 28 7

Arnaboldi M., Retzlaff J., 2011, *First ESO Public Release of Data from the VISTA Public Surveys,* Msngr, 146, 45 7

Balbi A. et al., 2000, *Constraints on cosmolgical parameters from MAXIMA-1,* ApJ, 545, L1 16

Baldry I. K. et al., 2010, *Galaxy And Mass Assembly (GAMA): the input catalogue and star-galaxy separation,* MNRAS, 100, 86 33, 37

Ball N. M., Loveday J., Brunner R. J., Baldry I. K., Brinkmann J., 2006, *Bivariate galaxy luminosity functions in the Sloan Digital Sky Survey,* MNRAS, 373, 845 106

Baum W., 1962, *Photoelectric Magnitudes and Red-Shifts,* International Astronomical Union Symposium, 390 78

Bell E. F., 2002, *Dust-induced Systematic Errors in Ultraviolet-derived Star Formation Rates,* ApJ, 577, 150 143

Bell E. F., McIntosh D. H., Katz N., Weinberg M. D., 2003, *The Optical and Near-Infrared Properties of Galaxies. I. Luminosity and Stellar Mass Functions,* ApJS, 149, 289 xviii, 147

Bell E. F. et al., 2006, *The merger rate of massive galaxies,* ApJ, 270 67

Benn C., 1983, *Optical identifications of radio sources in the presence of optical confusion,* The Observatory, 103, 150 47, 48, 49

Bessell M., 1979, *UBVRI photometry II: the Cousins VRI system, its temperature and absolute flux calibration, and relevance for two-dimensional photometry,* PASP, 91, 589 7

Bessell M., Brett J., 1988, *JHKLM photometry: standard systems, passbands, and intrinsic colors,* PASP, 100, 1134 7

Biggs A. D. et al., 2011, *The LABOCA survey of the Extended Chandra Deep Field-South - radio and mid-infrared counterparts to submillimetre galaxies,* MNRAS, 413, 2314 39, 42, 45

Bishop C., 1995, Neural Networks for Pattern Recognition. Clarendon Press - Oxford 86, 88, 90

Blain A., Longair M., 1993, *Submillimetre cosmology,* MNRAS, 264, 509 94

Blain A. W., Smail I., Ivison R. J., Kneib J. P., Frayer D. T., 2002, *Submillimeter Galaxies,* Physics Reports, 369, 111 ix, 9

Boissier S. et al., 2007, *Radial variation of attenuation and star formation in the largest late-type disks observed with GALEX,* ApJS, 173, 524 xviii, xix, 146, 149, 150, 151, 152, 160

Bolzonella M., Miralles J., Pell R., 2000, *Photometric redshifts based on standard SED fitting procedures,* A&A, 492, 476 83

Bond N. A. et al., 2012, *The infrared properties of sources matched in the WISE All-Sky and Herschel ATLAS surveys,* ApJ, 750, L18 13, 40, 162

Borys C. et al., 2004, *The Hubble Deep Field North SCUBA Super-map - II. Multi-wavelength properties,* MNRAS, 355, 485 44

Bourne N. et al., 2012, *Herschel-ATLAS/GAMA : a census of dust in optically selected galaxies from stacking at submillimetre wavelengths,* MNRAS, 421, 3027 125

Brammer G. B., van Dokkum P. G., Coppi P., 2008, *EAZY: A Fast, Public Photometric Redshift Code,* ApJ, 686, 1503 83

Bruzual G., 1990, *Extracting cosomological and evolutionary parameters from distant galaxy observations,* ASP Conference Series, 10, 185 121

Bruzual G., Charlot S., 2003, *Stellar population synthesis at the resolution of 2003,* MNRAS, 344, 1000 140

Buat V. et al., 2010, *Measures of star formation rates from infrared (Herschel) and UV (GALEX) emissions of galaxies in the HerMES fields,* MNRAS, 6, 6 xviii, 140, 141, 143, 144, 146, 147, 149, 165

Buat V. et al., 2005, *Dust attenuation in the nearby universe: a comparison between galaxies selected in the ultraviolet and in the far-infrared,* ApJ, 619, 51 xviii, xix, 146, 147, 148, 149, 151

Buat V. et al., 2007, *The Local Universe as Seen in the FarInfrared and FarUltraviolet: A Global Point of View of the Local Recent Star Formation,* ApJS, 173, 404 xviii, 142, 147

Calzetti D., Armus L. E. E., Bohlin R. C., Kinney A. L., Storchi-Bergmann T., 2000, *The dust content and opacity of actively star-forming galaxies,* ApJ, 533, 682 146

Chabrier G., 2003, *Galactic stellar and substellar initial mass,* PASP, 115, 763 141

Chapin E. L. et al., 2011, *A joint analysis of BLAST 250-500μm and LABOCA 870μm observations in the Extended Chandra Deep Field-South,* MNRAS, 411, 505 12, 94, 102, 160

Chapin E. L., Hughes D. H., Aretxaga I., 2009, *The local far-infrared galaxy colour luminosity distribution : a reference for BLAST and Herschel / SPIRE submillimetre surveys,* MNRAS, 662, 653 42, 45, 106

Chapman S. C., Windhorst R., Odewahn S., Yan H., Conselice C., 2003, *Hubble Space Telescope images of submillimeter sources: large irregular galaxies at high redshift,* ApJ, 599, 92 10

Choloniewski J., 1985, *Bivariate luminosity fuction of E and S0 galaxies,* MNRAS, 214, 197 106

Ciliegi P. et al., 2003, *Astrophysics A deep VLA survey at 6 cm in the Lockman Hole,* Astronomy, 918, 901 51, 52, 163

Clegg P. E., 1980, *The Infrared Astronomical Satellite-IRAS,* Physica Scripta, 21, 678 10

Clements D. et al., 2004, *The Canada-UK Deep Submillimetre Survey - VIII. Source identifications in the 3-hour field,* MNRAS, 351, 447 42, 43

Cole S. et al., 2005, *The 2dF Galaxy Redshift Survey: power-spectrum analysis of the final data set and cosmological implications,* MNRAS, 362, 505 17

Colless M. et al., 2001, *The 2dF Galaxy Redshift Survey : spectra and redshifts,* MNRAS, 328, 1039 17

Collister A., Lahav O., 2004, *ANNz: estimating photometric redshifts using artificial neural networks,* PASP, 116, 345 xiv, 81, 87, 92, 93, 95

Condon J., 1974, *Confusion and flux-density error distribution,* ApJ, 188, 279 25

Connolly A., Koo D., Kron R., Munn J., 1995, *Slicing through multicolor space: galaxy redshifts from broadband photometry,* AJ, 110, 2655 84

Cowie L., Songaila A., Hu E., Cohen J., 1996, *New insight on galaxy formation and evolution from Keck Spectroscopy of the Hawaii Deep Fields,* AJ, 112, 839 10, 19

Csabai N. et al., 2007, *Multidimensional indexing tools for the virtual observatory,* Astronomische Nachrichten, 328, 852 84

Dalton G. et al., 2004, *The VISTA IR Camera,* Proc. SPIE, 5492, 988 27

Dannerbauer H. et al., 2010, *Unveiling Far-Infrared Counterparts of Bright Submillimeter Galaxies Using Pacs Imaging,* ApJ, 720, L144 42, 45

Dariush a. et al., 2011, *The environment and characteristics of low-redshift galaxies detected by theHerschel-ATLAS,* MNRAS, 418, 64 101

Davis M. et al., 2003, *Science Objectives and Early Results of the DEEP2 Redshift Survey,* SPIE, 4834, 161 96

de Bernardis P. et al., 2000, *First results from the BOOMERanG experiment,* Cosmology and Particle Physics: CAPP 2000. AIP Conference Proceedings, 555, 85 16

de Ruiter H., Willis A., Arp H., 1977, *A Westerbork 1415 MHz survey of background radio sources. II. Optical identifications with deep IIIA-J plates,* A&AS, 28, 211 46, 47, 48

Devlin M. J. et al., 2009, *Over half of the far-infrared background light comes from galaxies at $z \geq 1.2$,* Nature, 458, 737 25

Dickey J., Salpeter E., 1984, *1.4 GHz continuum sources in the Hercules cluster,* ApJ, 284, 461 10

Domínguez-Sánchez H. et al., 2012, *Comparison of star formation rates from Hα and infrared luminosity as seen by Herschel,* MNRAS, 426, 330 140

Downes A., Peacock J., Savage A., Carrie D., 1986, *The Parkes selected regions: powerful radio galaxies and quasars at high redshifts,* MNRAS, 218, 31 41, 42

Driver S. P. et al., 2009, *Galaxy And Mass Assembly (GAMA),* The Galaxy Disk in Cosmological Context, Proceedings of the International Astronomical Union, 469 37, 79

Dunkley J. et al., 2009, *Five-Year Wilkinson Microwave Anisotropy Probe Observations: Likelihoods and Parameters From the WMAP Data,* ApJS, 180, 306 80

Dunlop J. et al., 1989, *The Parkes Selected Regions: deep optical and infrared observations of radio galaxies and quasars at high redshifts,* MNRAS, 238, 1171 42

Dunlop J. S. et al., 2010, *The BLAST 250 μm-selected galaxy population in GOODS-South,* MNRAS, 408, 2022 xv, 12, 40, 71, 98, 101, 102, 160

Dunne L. et al., 2000, *The SCUBA Local Universe Galaxy Survey I . First measurements of the submillimetre luminosity and dust mass functions,* MNRAS, 315, 115 24, 114, 122, 123

Dunne L. et al., 2011, *Herschel -ATLAS : rapid evolution of dust in galaxies over the last 5 billion years,* MNRAS, 417, 1510 xvi, 110, 111, 112, 113, 119, 120, 122, 123, 125, 164

Dutton A. A. et al., 2012, *The SWELLS survey - V . A Salpeter stellar initial mass function in the bulges of massive spiral galaxies,* arXiv : 1206.4310, 1 141

Dye S. et al., 2009, *Radio and Mid-Infrared Identification of Blast Source Counterparts in the Chandra Deep Field South,* ApJ, 703, 285 xvii, 12, 25, 39, 40, 43, 44, 45, 55, 103, 116, 118, 123, 129

Dye S. et al., 2010, *Herschel-ATLAS : Evolution of the 250 μm luminosity function out to z=0.5,* A&A, 518, L10 xvi, xvii, 112, 113, 118, 119, 120, 123, 129, 138, 159

Dye S. et al., 2008, *The SCUBA HAlf Degree Extragalactic Survey (SHADES) VII. Optical/IR photometry and stellar masses of submillimetre galaxies,* MNRAS, 386, 1107 8, 25

Eales S., 1993, *Direct construction of the galaxy luminosity function as a function of redshift,* ApJ, 404, 51 109

Eales S. et al., 2009, *Blast: the Redshift Survey,* ApJ, 707, 1779 xvi, 110, 112, 113, 116, 117, 130, 133

Eales S. et al., 2010, *First results from HerMES on the evolution of the submillimetre luminosity function,* A&A, 518, L23 xvi, 36, 103, 116, 118, 130, 133

Elbaz D., 2005, *Understanding Galaxy Formation with ISO Deep Surveys,* Space Science Reviews, 119, 93 11, 24

Elbaz D., Cesarsky C. J., Fadda D., Aussel H., 1999, *Source counts from the 15 μm ISOCAM Deep Surveys,* A&A, 351, 37 23

Elbaz D. et al., 2010, *Herschel unveils a puzzling uniformity of distant dusty galaxies,* A&A, 518, L29 103, 114, 142, 160

Emerson J., McPherson A., Sutherland W., 2006, *Visible and Infrared Survey Telescope fro Astronomy: Progress Report,* The Messenger, 41 27

Emerson J., Sutherland W., 2010, *VISTA: Status and Performance,* Proc. SPIE, 7733, 773306 27

Faber S. et al., 2007, *Galaxy luminosity function to z∼1 from DEEP2 and COMBO-17: Implications for red galaxy formation,* ApJ, 665, 265 x, 21, 22

Felten J., 1976, *On Schmidt's V_m estimator and other estimators of luminosity functions,* ApJ, 207, 700 109

Findlay J. R. et al., 2012, *Selection constraints on high-redshift quasar searches in the VISTA Kilo-degree Infrared Galaxy survey,* MNRAS, 419, 3354 7, 58, 161

Fioc M., Rocca-Volmerange B., 1997, *PEGASE: a UV to NIR spectral evolution model of galaxies,* A&A, 326, 950 140

Firth A. E., Lahav O., Somerville R. S., 2003, *Estimating photometric redshifts with artificial neural networks,* October, 1202, 1195 93

Franceschini A., 1997, *Models of the extragalactic background,* ASP Conference Series, 124, 356 121

Franceschini A. et al., 2010, *Galaxy evolution from deep multi-wavelength infrared surveys: a prelude to Herschel,* A&A, 517, A74 xvi, 118, 122

Geach J. E., 2012, *Unsupervised self-organized mapping: a versatile empirical tool for object selection, classification and redshift estimation in large surveys,* MNRAS, 419, 2633 91

Geha M., Blanton M. R., Yan R., Tinker J. L., 2012, *A Stellar Mass Threshold for Quenching of Field Galaxies,* ApJ, 757, 85 22

Gilbank D. G., Baldry I. K., Balogh M. L., Glazebrook K., Bower R. G., 2010, *The local star formation rate density: assessing calibrations using [OII], Halpha and UV luminosities,* MNRAS, 405, 2594 140

Gonçalves T. S., Martin D. C., Menéndez-Delmestre K., Wyder T. K., Koekemoer A., 2012, *Quenching Star Formation At Intermediate Redshifts: Downsizing of the Mass Flux Density in the Green Valley,* ApJ, 759, 67 23

González-Nuevo J. et al., 2010, *Herschel -ATLAS: Blazars in the science demonstration phase field,* A&A, 518, L38 68

González-Nuevo J. et al., 2012, *Herschel-ATLAS: Toward a Sample of 1000 Strongly Lensed Galaxies,* ApJ, 749, 65 165

Granato G., Silva L., De Zotti G., Bressan A., Danese L., 2004, *A physical model for the joint evolution of qsos and spheroids,* Multiwavelength Cosmology. Proceedings of the "Multiwavelength Cosmology" conference, held on Mykonos Island, Greece, 17-20 June, 2003. Edited by Manolis Plionis. Astrophysics and Space Science Library, 301, 129 122

Griffin M. J. et al., 2010, *The Herschel -SPIRE instrument and its in-flight performance,* A&A, 1 5, 35

Guiderdoni B., Hivon E., Bouchet F. R., Maffei B., 1998, *Semi-analytic modelling of galaxy evolution in the IR / submm range,* MNRAS, 295, 877 121

Gurney K., 1997, An Introduction to Neural Networks. UCL Press Limited 85, 86

Guth A., 1981, *Inflationary universe: a possible solution to the horizon and the flatness problems,* Phys. Rev. D, 23, 347 16

Hainline L. J. et al., 2009, *A Mid-Infrared Imaging Survey of Submillimeter-Selected Galaxies With the Spitzer Space Telescope,* ApJ, 699, 1610 40

Hambly N. C. et al., 2008, *The WFCAM Science Archive,* MNRAS, 384, 637 27

Hardcastle M. J. et al., 2010, *Herschel-ATLAS: far-infrared properties of radio-selected galaxies,* MNRAS, 409, 122 40

Harrison F. A. et al., 2010, *The Nuclear Spectroscopic Telescope Array (NuSTAR),* Space Telescopes and Instrumentation 2010: Ultraviolet to Gama Ray. Edited by Arnaud, M., Murray, S.S., Takahashi, T., Proceedings of the SPIE, 7732, 0S 161

Hewett P. C., Warren S. J., Leggett S. K., Hodgkin S. T., 2006, *The UKIRT Infrared Deep Sky Survey ZY JHK photometric system: passbands and synthetic colours,* MNRAS, 367, 454 28, 95

Hildebrand R., 1983, *The determination of cloud mass and dust characteristics from submillimetre thermal emission,* Quarterly Journal of the Royal Astronomical Society, 24, 267 123

Hildebrandt H. et al., 2010, *PHAT : PHoto-z Accuracy Testing,* A&A, A31 82, 93

Hodgkin T., Irwin M. J., Hewett P. C., Warren S. J., 2009, *The UKIRT Wide Field Camera ZYJHK Photometric System : Calibration from 2MASS,* MNRAS, 394, 675 30, 31

Hogg D. W., Baldry I. K., Blanton M. R., Eisenstein D. J., 2002, *The K correction,* astro.ph.10394H, 1 8

Holland W. S. et al., 1999, *SCUBA : a common-user submillimetre camera operating on the James Clerk Maxwell Telescope,* MNRAS, 303, 659 8, 113

Hoyos C. et al., 2012, *A new automatic method to identify galaxy mergers - I. Description and application to the Space Telescope A901/902 Galaxy Evolution Survey,* MNRAS, 419, 2703 163

Hubble E., 1926, *Extra-galactic nebulae,* ApJ, 64, 321 13, 18

Hubble E., 1929, *A Relation between Distance and Radial Velocity among Extra-Galactic Nebulae,* Communication from the Mount Wilson Observatory, 105, 23 14, 77, 79

Hughes D. et al., 1998, *Unveiling Dust-enshrouded Star Formation in the Early Universe : a Sub-mm Survey of the Hubble Deep Field,* Nature, 394, 241 10, 24

Ibar E. et al., 2010, *H-ATLAS : PACS imaging for the Science Demonstration Phase,* Distribution, 000 36

Ilbert O. et al., 2006, *Accurate photometric redshifts for the CFHT legacy survey calibrated using the VIMOS VLT deep survey,* A&A, 457, 841 83

Ivison R. et al., 2002, *Deep radio imaging of the SCUBA 8-mJy survey fields: submillimetre source identifications and redshift distribution,* MNRAS, 337, 1 42

Ivison R. J. et al., 2010, *BLAST: the far-infrared/radio correlation in distant galaxies,* MNRAS, 402, 245 40

Ivison R. J. et al., 2007, *The SCUBA HAlf Degree Extragalactic Survey - III. Identification of radio and mid-infrared counterparts to submillimetre galaxies,* MNRAS, 380, 199 25, 39, 40, 42, 43, 51

Jarvis M. J. et al., 2010, *Herschel-ATLAS: the far-infrared-radio correlation at $z < 0.5$,* MNRAS, 409, 92 40

Jiang L. et al., 2008, *A survey of $z \sim 6$ quasars in the Sloan Digital Sky Survey Deep Stripe. I . A flux-limited sample at $z_{AB} < 21$,* AJ, 135, 1057 110

Johnson H., Morgan W., 1953, *Fundamental stellar photometry for standards of spectral type on the revised system of the Yerkes Spectral Atlas,* ApJ, 117, 313 5

Johnston R., 2011, *Shedding Light on the Galaxy Luminosity Function,* Astronomy and Astrophysics Review 107

Johnston S. et al., 2008, *Science with ASKAP,* Experimental Astronomy, 22, 151 40

Kampen E. V. et al., 2012, *Herschel-ATLAS/GAMA : spatial clustering of low-redshift submm galaxies,* MNRAS, 426, 3455 25

Kennicutt R., 1998, *The global Schmidt law in star-forming galaxies,* ApJ, 498, 541 139, 140, 142

Kessler M. F. et al., 1996, *The Infrared Space Observatory (ISO) mission,* A&A, 315, 27 10

Kim S. et al., 2012, *Spitzer -Irac Identification of Herschel -Atlas Spire Sources,* ApJ, 756, 28 40, 162

Kirkpatrick J. D. et al., 1999, *Dwarfs cooler than "M" : the definition of spectral type "L" using discoveries from the 2-micron all-sky survey (2MASS),* ApJ, 519, 802 7

Komatsu E. et al., 2011, *Seven-Year Wilkinson Microwave Anisotropy Probe (WMAP) Observations: Cosmological Interpretation,* ApJS, 192, 18 17

Kong X., Charlot S., Brinchmann J., Fall S. M., 2004, *Star formation history and dust content of galaxies drawn from ultraviolet surveys,* MNRAS, 349, 769 xviii, xix, 144, 146, 149, 150, 151, 152, 160

Krause E., Hirata C., Martin C., Neill J., Wyder T., 2012, *Halo occupation distribution modeling of green valley galaxies,* arxiv:1208.6139v2 23

Kroupa P., 2001, *On the variation of the initial mass function,* MNRAS, 322, 231 141

Lagache G., Dole H., Puget J.-L., 2003, *Modelling infrared galaxy evolution using a phenomenological approach,* MNRAS, 338, 555 24, 101, 121, 122

Lahav O., Naim A., Sodré L., Storrie-Lombardi M., 1996, *Neural computation as a tool for galaxy classification: methods and examples,* MNRAS, 207 90

Lapi A. et al., 2011, *Herschel -Atlas Galaxy Counts and High-Redshift Luminosity Functions: the Formation of Massive Early-Type Galaxies,* ApJ, 742, 24 xiii, 63, 65, 94

Lawrence A., Walker D., Rowan-Robinson M., Leech K., Penston M., 1986, *Studies of IRAS sources at high galactic latitudes - II. Results from a redshift survey at $b > 60$: distribution in depth, luminosity function, and physical nature of IRAS galaxies,* MNRAS, 219, 687 114

Lawrence A. et al., 2007, *The UKIRT Infrared Deep Sky Survey (UKIDSS),* MNRAS, 379, 1599 7, 95

Leitherer C., Heckman T. M., 1995, *Synthetic properties of starburst galaxies,* ApJ, 96, 9 142

Leitherer C. et al., 1999, *Starburst99 : synthesis models for galaxies with active star formation claus leitherer,* ApJS, 123, 3 140, 141, 142, 148

Lewis J. R., Irwin M., Bunclark P., 2010, *Pipeline Processing for VISTA,* Analysis, 434, 91 27

Li I. H., Yee H. K. C., 2008, *Finding galaxy groups in photometric-redshift space: the probability friends-of-friends algorithm,* AJ, 135, 809 84

Lilly S. et al., 2007, *zCOSMOS : A large VLT / VIMOS redshift survey covering* $0 < z < 3$ *in the COSMOS Field,* ApJS, 172, 70 96

Lilly S. J. et al., 1999, *The Canada-United Kingdom deep submillimetre surevey. II. First identifications, redshifts, and implications for galaxy evolution,* ApJ, 518, 641 42

Lippmann R. P., 1987, *An introduction to computing with neural nets,* ASSP Magazine, IEEE, 4, 4 xiv, 86

Lodieu N. et al., 2012, *First T dwarfs in the VISTA Hemisphere Survey,* arxiv:1210.5148 7

Lodieu N., Dobbie P. D., Deacon N. R., Venemans B. P., Durant M., 2009, *Two distant brown dwarfs in the UKIRT Infrared Deep Sky Survey Deep Extragalactic Survey Data Release 2,* MNRAS, 395, 1631 7

Lotz J. M., 2007, *The Evolution of the Galaxy Merger Rate at z ¡ 1,* ASP Conference Series, 380, 467 67

Maddox N., Hewett P. C., Péroux C., Nestor D. B., Wisotzki L., 2012, *The large area KX quasar catalogue - I. Analysis of the photometric redshift selection and the complete quasar catalogue,* MNRAS, 424, 2876 161

Maddox N., Hewett P. C., Warren S. J., Croom S. M., 2008, *Luminous K-band selected quasars from UKIDSS,* MNRAS, 386, 1605 161

Maddox S. J. et al., 2010, *Herschel -ATLAS: The angular correlation function of sub-millimetre galaxies at high and low redshift,* A&A, 518, L11 101

Mazzei P., De Zotti G., Xu C., 1994, *Models for the evolution of the spectral energy distribution of elliptical galaxies from ultraviolet to far-infrared wavelenghts,* ApJ, 422, 81 121

McAlpine K., Smith D. J. B., Jarvis M. J., Bonfield D. G., Fleuren S., 2012, *The likelihood ratio as a tool for radio continuum surveys with Square Kilometre Array precursor telescopes,* MNRAS, 423, 132 162

McCulloch W., Pitts W., 1943, *A logical calculus of the ideas immanent in nervous activity,* Bulletin of Mathematical Biophysics, 7, 115 85

Meurer G., Heckman T., Calzetti D., 1999, *Dust absorption and the ultraviolet lluminosity density at z≈3 as calibrated by local starburst galaxies,* ApJ, 521, 64 xix, 10, 24, 146, 148, 149, 151, 152, 156, 158

Michalowski M. J., Hjorth J., Watson D., 2010, *Cosmic evolution of submillimeter galaxies and their contribution to stellar mass assembly,* A&A, 514, 67 40

Mortier A. M. J. et al., 2005, *The SCUBA Half-Degree Extraggalactic Survey - I. Survey motivation, design and data processing,* MNRAS, 363, 563 8

Mortlock D. J. et al., 2011, *A luminous quasar at a redshift of z=7.085,* Nature, 474, 616 7

Negrello M. et al., 2010, *The Detection of a Population of Submillimeter-Bright, Strongly-Lensed Galaxies,* Science, 330, 800 122, 165, 166

Negrello M. et al., 2007, *Astrophysical and cosmological information from large-scale submillimetre surveys of extragalactic sources,* MNRAS, 377, 1557 101, 122

Norris R. et al., 2011, *EMU: evolutionary Map of the Universe,* PASA, 28, 215 70

Oliver S. J. et al., 2010, *HerMES: SPIRE galaxy number counts at 250, 350, and 500 μm,* A&A, 518, L21 103

Oyaizu H., 2008, *Photometric redshift error estimators,* Hemisphere, 709 91

Page M. J., Carrera F. J., 2000, *An improved method of constructing binned luminosity functions,* MNRAS, 311, 433 109

Pascale E. et al., 2011, *The first release of data from the Herschel ATLAS: the SPIRE images,* MNRAS, 415, 911 36

Penzias A., Wilson R., 1965, *A measurement of excess antenna temperature at 4080 Mc/s,* ApJ, 142, 419 14

Percival W. J. et al., 2001, *The 2dF Galaxy Redshift Survey : the power spectrum and the matter content of the Universe,* MNRAS, 327, 1297 17

Pérez-González P. et al., 2010, *Spitzer View on the Downsizing Scenario of Galaxy Formation and the Role of AGN,* Highlights of Spanish Astrophysics V, Astrophysics and space Science Proceedings, 337 12

Perlmutter S. et al., 1999, *Measurements of* Ω *and* Λ *from 42 high-redshift supernovae,* ApJ, 517, 565 16

Pilbratt G. L. et al., 2010, *Herschel Space Observatory,* A&A, 518, L1 35

Poglitsch A. et al., 2010, *The Photodetector Array Camera and Spectrometer (PACS) on the Herschel Space Observatory,* A&A, 518, L2 35

Polletta M. et al., 2007, *Spectral energy distributions of hard x-ray selected active galactic nuclei in the XMM-Newton Medium Deep Survey,* ApJ, 663, 81 116, 137

Pope A. et al., 2006, *The Hubble Deep Field-North SCUBA Super-map - IV. Characterizing submillimetre galaxies using deep Spitzer imaging,* MNRAS, 370, 1185 42, 45

Popescu C. C., Tuffs R. J., Dopita M. A., Kylafis N. D., Madore B. F., 2011, *Modelling the spectral energy distribution of galaxies. V. The dust and PAH emission SEDs of disk galaxies,* A&A, 527, 109 143

Prestage R., Peacock J., 1983, *Optical identifications of Parkes radio sources using UK Schmidt plates,* MNRAS, 204, 355 48

Puget J.-L. et al., 1996, *Tentative detection of a cosmic far-infrared background with COBE,* A&A, 308, L5 11, 23

Reid I. N. et al., 1999, *L dwarfs and the substellar mass function,* ApJ, 521, 613 7

Rieke G. H., Lebofsky M., 1986, *The luminosity function for field galaxies in the infrared,* ApJ, 326 114

Riess A. G., Nugent P., Filippenko A. V., Kirshner R. P., Perlmutter S., 1998, *Snapshot distances to type 1a supernovae: all in "one" night's work,* ApJ, 504, 935 16

Rigby E. E. et al., 2011, *Herschel-ATLAS: first data release of the Science Demonstration Phase source catalogues,* MNRAS, 415, 2336 25, 36, 38, 111, 123, 133

Rodighiero G. et al., 2010, *The first Herschel view of the mass-SFR link in high-z galaxies,* A&A 12, 114, 142

Roseboom I. G. et al., 2012, *FMOS near-IR spectroscopy of Herschel selected galaxies : star formation rates , metallicity and dust attenuation at* $z \sim 1$*,* MNRAS, 426, 1782 25, 140

Roseboom I. G. et al., 2010, *The Herschel Multi-Tiered Extragalactic Survey: source extraction and cross-identifications in confusion-dominated SPIRE images,* MNRAS, 409, 48 40, 133

Rowan-Robinson M., 2001, *Models for the IR and submm SEDs of normal , starburst and active galaxies,* New Astronomy Reviews, 45, 631 24, 121

Rowlands K. et al., 2011, *Herschel -ATLAS / GAMA : Dusty early-type galaxies and passive spirals,* Nuclear Physics 25

Ryan, Jr. R. E., Cohen S. H., Windhorst R. a., Silk J., 2008, *Galaxy Mergers at* $z \simeq 1$ *in the HUDF: Evidence for a Peak in the Major Merger Rate of Massive Galaxies1,* ApJ, 678, 751 67

Sacchi N. et al., 2009, *Spectroscopic identifications of spitzer sources in the SWIRE/ XMM-NEWTON /ELAIS-S1 Field: a large fraction of active galactic nuclei with high F(24 μm)/F (R) ratio,* ApJ, 703, 1778 12

Salim S., Fang J. J., Rich R. M., Faber S. M., Thilker D. a., 2012, *Galaxy-scale star formation on the red sequence: the continued growth of S0s and the quiescence of ellipticals,* ApJ, 755, 105 22

Salim S. et al., 2007, *UV star formation rates in the local universe,* ApJS, 173, 267 140

Salpeter E., 1955, *The luminosity function and stellar evolution,* ApJ, 121, 161 141

Sandage A., Tammann G., Yahil A., 1979, *The velocity field of bright nearby galaxies. I. The variation of mean absolute magnitude with redshift for galaxies in a magnitude-limited sample,* ApJ, 352 108

Sanders D. et al., 1988, *Ultraluminous infrared galaxies and the origin of quasars,* ApJ, 325, 74 10

Saunders W. et al., 1990, *the 60-μm and far-infrared luminosity functions of IRAS galaxies,* MNRAS, 242, 318 107, 114, 116

Saunders W. et al., 2000, *The PSCz catalogue,* MNRAS, 317, 55 xvi, 117

Schechter P., 1976, *An analytical expression for the luminosity function for galaxies,* ApJ, 203, 297 106

Schilizzi R., Dewdney P., Lazio T., 2008, *The Square Kilometre Array,* Proc. SPIE, 7012, 52 40

Schmidt M., 1959, *The Rate of Star Formation,* ApJ, 129, 243 139

Schmidt M., 1968, *Space distribution and luminostiy functions of quasi-stellar radio sources,* ApJ, 151, 393 109

Serjeant S. et al., 2008, *The SCUBA Half Degree Extragalactic Survey (SHADES) IX. The environment, mass and redshift dependence of star formation,* MNRAS, 386, 1907 8, 24

Serjeant S., Harrison D., 2005, *The local submillimetre luminosity function and predictions from Spitzer to Herschel,* MNRAS, 192 xvi, xvii, 107, 114, 115, 116, 122, 133, 135

Simpson C. et al., 2012, *Radio imaging of the Subaru / XMM N ewt on Deep Field III . Evolution of the radio luminosity function beyond z = 1,* MNRAS, 421, 3060 110

Skelton R. E., Bell E. F., Somerville R. S., 2012, *Modeling the Red Sequence: Hierarchical Growth Yet Slow Luminosity Evolution,* ApJ, 753, 44 22

Slipher V., 1917, *Nebulae,* Proceedings of the American Philosophical Society, 56, 403 13

Smail I., Ivison R., Blain A., Kneib J. P., 2002, *The nature of faint submillimetre-selected galaxies,* MNRAS, 331, 495 10, 24

Smail I., Ivison R. J., Blain A., 1997, *A deep submillimetre survey of lensing clusters: a new window on galaxy formation and evolution,* ApJ, 490, 5 24

Smith D. J. B. et al., 2012, *Herschel-ATLAS : Multi-wavelength SEDs and physical properties of 250 μm-selected galaxies at $z < 0.5$,* MNRAS, 427, 703 xiii, 25, 58, 63, 65, 123

Smith D. J. B. et al., 2011, *Herschel-ATLAS: counterparts from the ultraviolet-near-infrared in the science demonstration phase catalogue,* MNRAS, 416, 857 xiv, 25, 38, 43, 50, 51, 53, 54, 63, 70, 71, 75, 95, 98, 101, 112, 118, 163, 165

Smith G. et al., 2004, *AAOmega: a multipurpose fiber-fed spectrograph for the AAT,* Proc. SPIE, 5492, 410 79

Smith H., Lonsdale C., Lonsdale C. J., 1998, *The starburst-AGN connection. II. The nature of luminous infrared galaxies as revealed by VLBI, VLA, infrared and optical observations,* ApJ, 492, 17 10

Soifer B., Houck J., Neugebauer G., 1987, *The IRAS view of the extragalactic sky,* Ann. Rev. Astron. Astrophys., 25, 187 10, 23

Spergel D. N. et al., 2007, *Three-year Wilkinson Microwave Anisotropy Probe (WMAP observations: Implications for cosmology,* ApJ, 170, 377 14, 17, 19

Springel V. et al., 2005, *Simulating the joint evolution of quasars, galaxies and their large-scale distribution,* Nature, 435, 629 20

Stevenson K. B. et al., 2012, *Two Nearby Sub-Earth-Sized Exoplanet Candidates in the Gj 436 System,* ApJ, 755, 9 12

Sutherland W., Saunders W., 1992, *On the likelihood ratio for source identification,* MNRAS, 259, 413 49, 163

Takagi T. et al., 2007, *The SCUBA HAlf Degree Extragalactic Survey (SHADES) - V. Submillimetre properties of near-infrared-selected galaxies in the Subaru/XMM-Newton deep field,* MNRAS, 381, 1154 8

Tegmark M. et al., 2004, *Cosmological parameters from SDSS and WMAP,* Physical Review D, id103501 17

Thompson M. a. et al., 2010, *A search for debris disks in the Herschel -ATLAS,* A&A, 518, L134 68

Tokunaga A. T., Simons D. A., Vacca W. D., 2002, *The Mauna Kea Observatories Near-Infrared Filter Set. II. Specifications for a New JHKLM Filter Set for Infrared Astronomy,* PASP, 114, 180 28

Tonnesen S., Cen R., 2012, *Effects on galaxy evolution: pair interactions versus environment,* MNRAS, 425, 2313 22

Unger S. et al., 1989, *The relationship between the radio and far-infrared emission in IRAS galaxies: VLA observations of a large well-defined sample at 1420MHz,* MNRAS, 236, 425 10

Vaccari M. et al., 2010, *Special feature The HerMES SPIRE submillimeter local luminosity function,* Observatory, 20, 1 xvi, xvii, 116, 118, 122, 133, 135

Véron-Cetty M.-P., Véron P., 2010, *A catalogue of quasars and active nuclei: 13th edition,* A&A, 518, A10 xiii, 68, 69

Vlahakis C., Dunne L., Eales S., 2005, *The SCUBA Local Universe Galaxy survey - III. Dust along the Hubble sequence,* MNRAS, 1253 116

Wang D., Zhang Y. X., Liu C., Zhao Y. H., 2007, *Kernel regression for determining photometric redshifts from Sloan broad-band photometry,* MNRAS, 1606, 1601 84

Warren S. J., Hewett P. C., Foltz C. B., 2000, *The KX method for producing K-band flux-limited samples of quasars,* MNRAS, 312, 827 161

Way M. J., Klose C. D., 2012, *Can selforganizing maps accurately predict photometric redshifts?,* PASP, 124, 274 91

Wijesinghe D. B. et al., 2011, *GAMA/H-ATLAS: the ultraviolet spectral slope and obscuration in galaxies,* MNRAS, 415, 1002 xix, 140, 143, 146, 148, 149, 152, 153, 156, 157, 158

Willmer C. N. A. et al., 2006, *The Deep Evolutionary Exploratory Probe 2 galaxy redshift survey: the galaxy luminosity function to $z \sim 1$,* ApJ, 647, 853 108

Wolf C., 2009, *Bayesian photometric redshifts with empirical training sets,* MNRAS, 533, 520 84

Wootten A., Thompson A., 2009, *The Atacama Large Millimeter/submillineter Array,* Proceedings of the IEEE, 97, 1463 70

Wright E., 2003, *The WMAP data and results,* New Astronomy Reviews, 47, 877 19